

國立交通大學

材料科學與工程學系

博士論文

雙效型氣體擴散電極與高表面積碳凝膠製備

及電化學分析

Material Synthesis, Characterization, and
Electrochemical Analysis for Bi-functional Gas Diffusion
Electrodes and Carbon Ambient Gels

研究生：張雲閔

指導教授：吳樸偉 教授

中華民國一百零一年七月

雙效型氣體擴散電極與高表面積碳凝膠製備

及電化學分析

Material Synthesis, Characterization, and Electrochemical
Analysis for Bi-functional Gas Diffusion Electrodes and Carbon
Ambient Gels

研 究 生：張雲閔

Student: Yun-Min Chang

指 導 教 授：吳樸偉 教授

Advisor: Professor Pu-Wei Wu

國 立 交 通 大 學
材 料 科 學 與 工 程 學 系
博 士 論 文

A Thesis

Submitted to Department of Materials Science and Engineering

College of Engineering

National Chiao Tung University

in Partial Fulfillment of the Requirements

for the Degree of Doctor of Philosophy

in

Materials Science and Engineering

July 2012

Hsinchu, Taiwan, Republic of China

中 華 民 國 一 百 零 一 年 七 月

雙效型氣體擴散電極與高表面積碳凝膠製備及電化學分析

研究生：張雲閔

指導教授：吳樸偉 教授

國立交通大學

材料科學與工程學系

摘要

本研究利用檸檬酸鹽法(amorphous citrate precursor)合成化學劑量比為 $\text{La}_{0.6}\text{Ca}_{0.4}\text{Co}_{0.8}\text{Ru}_{0.2}\text{O}_3$ 粉末。此外，利用固態燒結法(solid-state reaction)合成 $\text{La}_{0.6}\text{Ca}_{0.4}\text{Co}_x\text{Ru}_{1-x}\text{O}_3$ 的鈣鈦礦氧化物 ($x = 0, 0.2, 0.4, 0.6, 0.8$ 及 1) 粉末。由 X 光粉末繞射(XRD)可觀察到主相為鈣鈦礦的 $\text{La}_{0.6}\text{Ca}_{0.4}\text{CoO}_3$ ，表示成功的將 Ru^{4+} 插層入 $\text{La}_{0.6}\text{Ca}_{0.4}\text{CoO}_3$ 相中，元素組成(EDX)分析結果亦與合成時比例一致。在鹼性 KOH 溶液中，利用 H_2O_2 分解反應測試其催化效能， $\text{La}_{0.6}\text{Ca}_{0.4}\text{Co}_{0.8}\text{Ru}_{0.2}\text{O}_3$ 展現出優於 $\text{La}_{0.6}\text{Ca}_{0.4}\text{CoO}_3$ 之催化活性，推測在氧氣還原反應中，Ru 摻雜後催化活性被提升。類似的情形可利用氧氣還原極化曲線佐證，實驗中以 Black Pearl 2000 (BP2000)當作氣體擴散層的觸媒載體。在恆定電流長時間放電評估， $\text{La}_{0.6}\text{Ca}_{0.4}\text{Co}_{0.8}\text{Ru}_{0.2}\text{O}_3/\text{BP2000}$ 皆有穩定的電流輸出。另一方面，在氫氣氧化(hydrogen evolution reaction)與氧氣還原(oxygen reduction reaction)極化曲線反應中， $\text{La}_{0.6}\text{Ca}_{0.4}\text{Co}_x\text{Ru}_{1-x}\text{O}_3/\text{BP2000}$ 相較於 $\text{La}_{0.6}\text{Ca}_{0.4}\text{CoO}_3/\text{BP2000}$ 皆表現出較佳的雙效催化活性，在 SSR 法 $\text{La}_{0.6}\text{Ca}_{0.4}\text{Co}_x\text{Ru}_{1-x}\text{O}_3/\text{BP2000}$ 系統中， $\text{La}_{0.6}\text{Ca}_{0.4}\text{Co}_{0.4}\text{Ru}_{0.6}\text{O}_3/\text{BP2000}$ 具有最佳的雙功能催化活性。

研究中，採用機械研磨法研磨 $\text{La}_{0.6}\text{Ca}_{0.4}\text{CoO}_3$ 與 IrO_2 粉末，成功的製備出 $\text{La}_{0.6}\text{Ca}_{0.4}\text{CoIr}_{0.25}\text{O}_{3.5-\delta}$ 觸媒。另一方面，利用檸檬酸鹽法合成在鹼性電解液下具有

氧還原與氧生成的 $\text{La}_{0.6}\text{Ca}_{0.4}\text{Co}_{0.8}\text{Ir}_{0.2}\text{O}_3$ 雙效觸媒。粉末 XRD 圖中展現出以 $\text{La}_{0.6}\text{Ca}_{0.4}\text{CoO}_3$ 為主相，表示 Ir^{4+} 成功進入鈣鈦礦 Co 的位置。在電化學分析中， $\text{La}_{0.6}\text{Ca}_{0.4}\text{CoIr}_{0.25}\text{O}_{3.5-\delta}/\text{CNCs}$ 與 $\text{La}_{0.6}\text{Ca}_{0.4}\text{Co}_{0.8}\text{Ir}_{0.2}\text{O}_3/\text{CNCs}$ 觸媒相對於 $\text{La}_{0.6}\text{Ca}_{0.4}\text{CoO}_3/\text{CNCs}$ ，不論是放電或充電電流對電壓極化曲線皆有較優越的性能表現，比較 Ru 與 Ir 摻雜入 $\text{La}_{0.6}\text{Ca}_{0.4}\text{CoO}_3$ 中，兩者的還原反應電催化性能相近。此外，以表面電位(Zeta Potential)測量表面電位， $\text{La}_{0.6}\text{Ca}_{0.4}\text{Co}_{0.8}\text{Ir}_{0.2}\text{O}_3$ 相對於 $\text{La}_{0.6}\text{Ca}_{0.4}\text{Co}_{0.8}\text{Ir}_{0.2}\text{O}_3$ 有顯著變化。最後，以連續 3 小時為一循環重複氧還原反應/靜置/氧氧化反應， $\text{La}_{0.6}\text{Ca}_{0.4}\text{Co}_{0.8}\text{Ir}_{0.2}\text{O}_3/\text{CNCs}$ 觸媒呈現穩定與持續耐久度。

對於提升電化學活性，除了合成適當的觸媒，開發適當的觸媒載體是另一關鍵議題，因此，本研究利用間苯二酚-甲醛(resorcinol-formaldehyde)的縮合反應合成碳常壓凝膠，做為電化學電雙層電容探討研究，其中反應中選擇醋酸為催化劑，樣品濃度 R:F 為 1:2，R:C 比例控制為 5:1 與 10:1，接下來經過溶劑交換、熱裂解與二氧化碳活化。在溶劑的交換過程可避免乾燥過程中結構收縮，再經過二氧化碳活化後，我們能得到到多孔性的碳結構，其表面積達到 $3419 \text{ m}^2\text{g}^{-1}$ 。由 SEM 觀察到相互交連的泡沫狀結構，由 BET 證實有大量的微孔與中孔。電容特性與動力學探討部分，使用鈦孔穴電極做電化學分析量測，所使用的技術有定電流充放電法(Current Reversal Chronopotentiometry, CRC)，循環伏安法(Cyclic Voltammetry, CV)，以及交流阻抗法(Electrochemical Impedance Spectroscopy, EIS)法。由 CV 與 CRC 結果得知，我們所合成出的碳常壓空氣凝膠相對於市售的 BP2000 具有較佳的比電容與持續耐久度。舉例來說，在電位區間為 0-1 V， 1 Ag^{-1} 得充放電條件下，比電容值為 324.8 Fg^{-1} ，相對來說，沒有經過活化處理的樣品，雖然有類似的相型態，但表面積與比電容大幅降低至 $449 \text{ m}^2\text{g}^{-1}$ 以及 34.7 Fg^{-1} 。

Material Synthesis, Characterization, and Electrochemical Analysis for Bi-functional Gas Diffusion Electrodes and Carbon Ambient Gels

Student: Yun-Min Chang

Advisor: Professor Pu-Wei Wu

Department of Materials Science and Engineering

National Chiao Tung University

Abstract

We employed an amorphous citrate precursor (ACP) method to synthesize stoichiometric $\text{La}_{0.6}\text{Ca}_{0.4}\text{Co}_{0.8}\text{Ru}_{0.2}\text{O}_3$ powders. Besides, a variety of $\text{La}_{0.6}\text{Ca}_{0.4}\text{Co}_x\text{Ru}_{1-x}\text{O}_3$ perovskite oxide ($x=0, 0.2, 0.4, 0.6, 0.8, \text{ and } 1$) were fabricated by solid-state reaction (SSR) method to form oxide powder with various ruthenium (Ru) ratios. X-ray diffraction profiles (XRD) of the as-synthesized powders exhibited the major phase identical is $\text{La}_{0.6}\text{Ca}_{0.4}\text{CoO}_3$, indicating successful incorporation of Ru^{4+} at the Co cation sites. ACP-derived $\text{La}_{0.6}\text{Ca}_{0.4}\text{Co}_{0.8}\text{Ru}_{0.2}\text{O}_3$ exhibited a higher H_2O_2 decomposition rate in KOH solution as opposed to that of ACP-derived $\text{La}_{0.6}\text{Ca}_{0.4}\text{CoO}_3$, which suggested an improved catalytic ability for the oxygen reduction reaction (ORR). In ORR and hydrogen evolution reaction (HER) I-V polarization curves, the SSR-derived $\text{La}_{0.6}\text{Ca}_{0.4}\text{Co}_x\text{Ru}_{1-x}\text{O}_3/\text{BP2000}$ revealed an enhanced bi-functional catalytic ability in comparison with those of $\text{La}_{0.6}\text{Ca}_{0.4}\text{CoO}_3/\text{BP2000}$. $\text{La}_{0.6}\text{Ca}_{0.4}\text{CoIr}_{0.25}\text{O}_{3.5-\delta}$ was prepared by a mechanical alloying process from mixtures of $\text{La}_{0.6}\text{Ca}_{0.4}\text{CoO}_3$ and IrO_2 . The ACP method was

employed to prepare perovskite $\text{La}_{0.6}\text{Ca}_{0.4}\text{Co}_{0.8}\text{Ir}_{0.2}\text{O}_3$ as a bi-functional electrocatalyst for ORR and HER in an alkaline electrolyte. The XRD pattern of the as-synthesized powders exhibited the major phase is $\text{La}_{0.6}\text{Ca}_{0.4}\text{CoO}_3$, indicating successful incorporation of Ir^{4+} at the Co cation sites. Supported on carbon Nanocapsules (CNCs), the $\text{La}_{0.6}\text{Ca}_{0.4}\text{CoIr}_{0.25}\text{O}_{3.5-8}$ and $\text{La}_{0.6}\text{Ca}_{0.4}\text{Co}_{0.8}\text{Ir}_{0.2}\text{O}_3$ particles demonstrated superior performances than those of $\text{La}_{0.6}\text{Ca}_{0.4}\text{CoO}_3$ in both charging and discharging I-V polarizations. For Ru and Ir doped into $\text{La}_{0.6}\text{Ca}_{0.4}\text{CoO}_3$, the electrochemical capabilities displayed similar performance for the ORR. In life time determinations, $\text{La}_{0.6}\text{Ca}_{0.4}\text{Co}_{0.8}\text{Ir}_{0.2}\text{O}_3/\text{CNCs}$ delivered a stable and sustainable behavior with moderate degradation.

In addition to synthesis of suitable electrocatalyst, the other critical issue is to identify appropriate material as electrocatalyst support. Therefore, a resorcinol–formaldehyde (R-F) condensation reaction catalyzed by acetic acid (C) is employed to prepare the carbon ambient gels for electrochemical double layer capacitors. The samples was fabricated with a R:F ratio of 1:2 and R:C ratios of 5:1 and 10:1, followed by solvent exchange, pyrolysis, and CO_2 activation. The solvent exchange allowed negligible structure contraction upon drying, and after CO_2 treatment, we were able to produce porous carbons with a surface area of $3419 \text{ m}^2\text{g}^{-1}$. Electrochemical analysis including cyclic voltammetry (CV), current reversal chronopotentiometry (CRC), and impedance spectroscopy are conducted using a titanium cavity electrode so relevant capacitive characteristics and kinetic parameters could be determined. Both CV and CRC results indicate specific capacitances and life time behaviors are comparable or even better than those of BP 2000.

Acknowledgement

六年，是可以從小養成小孩品格的教育期間，也是學生我完成交大博士的一段重要歷程；在這段可以創造、探索、自我充實與學習的階段，除了完成這份成果報告-博士論文之外，也讓我獲得許多不同經歷與收穫。

首先，感謝吳樸偉教授的細心教導；在他身上，讓我除了獲得專業的研究知識外，也體驗到許多做人處事道理；另外，感謝王禎翰、葉宗洸、張淑閔、陳錦毅、謝宗雍等五位教授，不辭辛勞前往交大材料系，指導學生論文與提醒修正，讓學生的論文更趨於完備。

在研究的過程中，特別感謝吳成有博士，因為吳博士不嫌麻煩的分享了他對於學生研究上的建議與經費上的支持，才能夠讓學生無後顧之憂的完成研究；然而，研究的過程中總是會遭遇許多瓶頸與挫折，但幸好有俊翰學弟分享天馬行空的想法，讓我透過多角度的層面，讓實驗過程中增添更多可能性與研究成果；另外還有育淇學弟，因為有你的共同打拼精神，讓冗長的實驗過程，不會因為等待結果而顯得枯燥乏味。

團結力量大，這句話已是老生常談，但也是不可挑戰的真理；學生在研究期間，所發表的多篇期刊、完成的多項計畫與多場次研討會的共同參與，著實讓學生的研究生活充實與獲得，但是，學生了解，這樣的經歷，透過學生一個人是沒有辦法完成的，因此再次感謝吳樸偉教授的細心指導，以及-濂方、儷曄、致源、映眉、柏均、于凡、茹夢、庭瑜與哲瑋學弟妹的幫忙，還有英文能力比美國人還棒立忠學弟給予英文上的協助，也要感謝生活中給予實質或精神支持的同學朋友-勝結、逸凡、玉塵、兆玲、境好、議文、儷尹、冠傑、尊偉、孟翰、意德、世儒、毓真、致芳、欣君、晨宏、咏錚、和成、耕余、佑慈、佳勳、筱琳、詠策、陳琪、婉瑩、亮余、柏翰、欣儀、依叡、建程、雁汝、韋霖、宥閔、華真與喬君

們實驗上的協助，因為有你們，讓我六年的博士生生活，多采多姿與樂趣。

最後，特別感謝在背後默默給予我支援的爸媽和老婆靈意，因為有你們的支持得以讓我心無旁騖，專心致力於課業及研究上。本研究能夠進行得如此順遂，以及論文能如期完成，不只是我個人的努力還要承蒙大家不吝相助，僅此榮耀獻給大家。



Contents

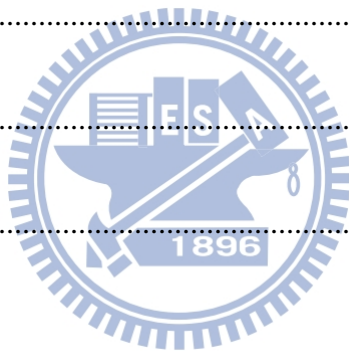
| | |
|--|-------|
| 摘要..... | i |
| Abstract..... | iii |
| Acknowledgement | v |
| Contents | vii |
| List of Tables..... | xi |
| List of Figures | xii |
| List of Symbols..... | xviii |
| Chapter 1 Introduction | 1 |
| 1.1 Background..... | 1 |
| 1.2 Motivations | 2 |
| Chapter 2 Literature Review | 5 |
| 2.1 Alkaline fuel cells | 5 |
| 2.2 Perovskite structure..... | 6 |
| 2.3 Oxygen reduction reaction..... | 8 |
| 2.4 Bi-functional electrocatalysts..... | 9 |
| 2.5 Gas diffusion electrodes and electrocatalyst support materials | 11 |



| | |
|---|----|
| 2.6 Supercapacitors | 12 |
| 2.7 Resorcinol-formaldehyde carbon gels | 14 |
| Chapter 3 Experimental | 16 |
| 3.1 Materials | 16 |
| 3.2 Experimental flowchart..... | 17 |
| 3.2.1 Flowchart for preparation of perovskite catalysts..... | 17 |
| 3.2.2 Flowchart for preparation of carbon ambient gels..... | 18 |
| 3.3 Synthesis of ACP-derived $\text{La}_{0.6}\text{Ca}_{0.4}\text{Co}_{0.8}\text{Ru}_{0.2}\text{O}_3$ and $\text{La}_{0.6}\text{Ca}_{0.4}\text{Co}_{0.8}\text{Ir}_{0.2}\text{O}_3$ | 18 |
| 3.4 Synthesis of SSR-derived $\text{La}_{0.6}\text{Ca}_{0.4}\text{Co}_x\text{Ru}_{1-x}\text{O}_3$ | 19 |
| 3.5 Synthesis of $\text{La}_{0.6}\text{Ca}_{0.4}\text{CoIr}_{0.25}\text{O}_{3.5-8}$ | 19 |
| 3.6 Fabrication of gas diffusion electrodes | 20 |
| 3.7 Synthesis of carbon ambient gels..... | 20 |
| 3.8 Material characterization | 22 |
| 3.8.1 X-ray diffraction (XRD) | 22 |
| 3.8.2 Scanning electron microscope (SEM) | 22 |
| 3.8.3 Brunauer, Emmett, and Teller (BET)..... | 23 |
| 3.8.4 Pycnometers measurement | 23 |

| | |
|--|----|
| 3.8.5 zeta potential | 23 |
| 3.8.6 Raman spectroscopy | 23 |
| 3.8.7 H ₂ O ₂ decomposition measurement | 23 |
| 3.9 Electrochemical measurements..... | 24 |
| 3.9.1 Gas diffusion electrode (GDE) | 24 |
| 3.9.2 Titanium Cavity Electrode (TCE)..... | 25 |
| Chapter 4 Synthesis and Characterization of La _{0.6} Ca _{0.4} Co _x Ru _{1-x} O ₃ for Bi-functional Electrodes | 26 |
| 4.1 Physico-chemical characterizations | 26 |
| 4.1.1 ACP-derived La _{0.6} Ca _{0.4} Co _{0.8} Ru _{0.2} O ₃ | 26 |
| 4.1.2 SSR-derived La _{0.6} Ca _{0.4} Co _{0.4} Ru _{0.6} O ₃ | 37 |
| 4.2 Electrochemical characterizations | 44 |
| 4.2.1 ACP-derived La _{0.6} Ca _{0.4} Co _{0.8} Ru _{0.2} O ₃ | 44 |
| 4.2.2 SSR-derived La _{0.6} Ca _{0.4} Co _{0.4} Ru _{0.6} O ₃ | 53 |
| Chapter 5 Synthesis and Characterization of La _{0.6} Ca _{0.4} CoIr _{0.25} O _{3.5-8} and La _{0.6} Ca _{0.4} Co _{0.8} Ir _{0.2} O ₃ for Bi-functional Electrodes | 63 |
| 5.1 Physico-chemical characterizations | 63 |
| 5.2 Electrochemical characterizations | 71 |

| | |
|--|-----|
| Chapter 6 Synthesis of Large Surface Area Carbon Ambient Gels for Electrochemical Double Layer Capacitors | 86 |
| 6.1 Structural characterizations..... | 86 |
| 6.2 Electrochemical characterizations | 92 |
| Chapter 7 Conclusions and Future Work | 105 |
| 7.1 Conclusions..... | 105 |
| 7.2 Future works | 107 |
| References..... | 109 |
| Vita..... | 130 |
| Publication List | 131 |



List of Tables

| | |
|--|-----|
| Table 3.1 Precursors and catalyst used for the synthesis of carbon ambient gels..... | 22 |
| Table 4.1 The decomposition rate for $\text{La}_{0.6}\text{Ca}_{0.4}\text{Co}_{0.8}\text{Ru}_{0.2}\text{O}_3$ and $\text{La}_{0.6}\text{Ca}_{0.4}\text{CoO}_3$ | 34 |
| Table 4.2 The summary of physical behavior for $\text{La}_{0.6}\text{Ca}_{0.4}\text{Co}_{1-x}\text{Ru}_x\text{O}_3$ | 39 |
| Table 4.3 EDX results of $\text{La}_{0.6}\text{Ca}_{0.4}\text{Co}_{1-x}\text{Ru}_x\text{O}_3$ | 44 |
| Table 4.4 Physical properties of carbonaceous materials | 45 |
| Table 4.5 Voltages at selective current densities in unit of mAcm^{-2} in the ORR I-V curves for $\text{La}_{0.6}\text{Ca}_{0.4}\text{Co}_{0.8}\text{Ru}_{0.2}\text{O}_3/\text{BP2000}$, $\text{La}_{0.6}\text{Ca}_{0.4}\text{CoO}_3/\text{BP2000}$, and $\text{La}_{0.6}\text{Ca}_{0.4}\text{Co}_{0.8}\text{Ru}_{0.2}\text{O}_3$ | 46 |
| Table 6.1 Relevant parameters for the pore properties determined by nitrogen adsorption and desorption isotherms from GA, GB, GC, and GD, respectively. | 90 |
| Table 6.2 Values of specific capacitance (Fg^{-1}) calculated from CV profiles in various potential windows at 20 mVs^{-1} scan rate..... | 94 |
| Table 6.3 Values of specific capacitance (Fg^{-1}) calculated from CV profiles at various scan rates in potential window of 0-1 V..... | 96 |
| Table 6.4 Relevant parameters determined from the CRC measurements at $\pm 1 \text{ Ag}^{-1}$ in potential window of 0-1 V..... | 99 |
| Table 6.5 Parameters from fitting impedance spectra obtained at the open circuit voltage..... | 102 |

List of Figures

| | |
|--|----|
| Figure 2.1 The structure of an alkaline fuel cell. | 6 |
| Figure 2.2 The structure of perovskite with a chemical formula ABO_3 | 7 |
| Figure 4.1 A representative TGA profile for the polymeric precursor of $La_{0.6}Ca_{0.4}Co_{0.8}Ru_{0.2}O_3$ | 27 |
| Figure 4.2 XRD for the as-synthesized (a) $La_{0.6}Ca_{0.4}Co_{0.8}Ru_{0.2}O_3$ and (b) $La_{0.6}Ca_{0.4}CoO_3$. Also shown is the standard pattern of $La_{0.6}Ca_{0.4}CoO_3$ from JCPDS 35.1389. | 29 |
| Figure 4.3 SEM images for the as-synthesized (a) $La_{0.6}Ca_{0.4}Co_{0.8}Ru_{0.2}O_3$ and (b) $La_{0.6}Ca_{0.4}CoO_3$ | 30 |
| Figure 4.4 Plots of $\ln([H_2O_2]_0/[H_2O_2]_t)$ as a function of time for (a) $La_{0.6}Ca_{0.4}Co_{0.8}Ru_{0.2}O_3$ and (b) $La_{0.6}Ca_{0.4}CoO_3$ at 0.01 (■), 0.015 (○), 0.02 (▲), 0.025 (×), and 0.03 g (☆), respectively. | 33 |
| Figure 4.5 Plot of k as a function of actual surface area for $La_{0.6}Ca_{0.4}Co_{0.8}Ru_{0.2}O_3$ (☆) and $La_{0.6}Ca_{0.4}CoO_3$ (■). | 36 |
| Figure 4.6 The XRD pattern of the $La_{0.6}Ca_{0.4}Co_{1-x}Ru_xO_3$ with x =(a) 0, (b) 0.2, (c) 0.4, (d) 0.6, (e) 0.8, and (f) 1..... | 37 |
| Figure 4.7 The unit cell volume versus the stoichiometric Ru. | 38 |
| Figure 4.8 SEM images of (a) $La_{0.6}Ca_{0.4}CoO_3$ (b) $La_{0.6}Ca_{0.4}Co_{0.8}Ru_{0.2}O_3$ (c) | |

| | | | |
|---|-----|--|-----|
| $\text{La}_{0.6}\text{Ca}_{0.4}\text{Co}_{0.6}\text{Ru}_{0.4}\text{O}_3$ | (d) | $\text{La}_{0.6}\text{Ca}_{0.4}\text{Co}_{0.4}\text{Ru}_{0.6}\text{O}_3$ | (e) |
| $\text{La}_{0.6}\text{Ca}_{0.4}\text{Co}_{0.2}\text{Ru}_{0.8}\text{O}_3$. (— scale bar $1\mu\text{m}$).....41 | | | |

Figure 4.9 SEM of $\text{La}_{0.6}\text{Ca}_{0.4}\text{Co}_{0.2}\text{Ru}_{0.8}\text{O}_3$ in (a) image, (b) mapping, (c) and EDX...43

Figure 4.10 The ORR I-V curves for GDEs catalyzed by $\text{La}_{0.6}\text{Ca}_{0.4}\text{Co}_{0.8}\text{Ru}_{0.2}\text{O}_3$ supported on BP2000, VXC72R, and CNCs, respectively.45

Figure 4.11 ORR I-V polarization curves for $\text{La}_{0.6}\text{Ca}_{0.4}\text{Co}_{0.8}\text{Ru}_{0.2}\text{O}_3/\text{BP2000}$ (\star), $\text{La}_{0.6}\text{Ca}_{0.4}\text{CoO}_3/\text{BP2000}$ (\blacksquare), and $\text{La}_{0.6}\text{Ca}_{0.4}\text{Co}_{0.8}\text{Ru}_{0.2}\text{O}_3$ (\times), respectively.47

Figure 4.12 The ORR I-V curves for the GDEs catalyzed by $\text{La}_{0.6}\text{Ca}_{0.4}\text{Co}_{0.8}\text{Ru}_{0.2}\text{O}_3/\text{BP2000}$, $\text{Co}_3\text{O}_4/\text{BP2000}$, and $\text{La}_2\text{O}_3/\text{BP2000}$, respectively. Also shown is the noncatalyzed GDE for comparison purpose.....48

Figure 4.13 Impedance spectra for the (a) $\text{La}_{0.6}\text{Ca}_{0.4}\text{Co}_{0.8}\text{Ru}_{0.2}\text{O}_3/\text{BP2000}$ and (b) $\text{La}_{0.6}\text{Ca}_{0.4}\text{CoO}_3/\text{BP2000}$ at open-circuit voltage (\square), and overpotentials of -100 mV (\circ), -200 mV (\times), and -300 mV (\star), respectively. (c) is the equivalent circuit model used to fit the impedance spectra.51

Figure 4.14 Galvanostatic ORR profiles for $\text{La}_{0.6}\text{Ca}_{0.4}\text{Co}_{0.8}\text{Ru}_{0.2}\text{O}_3/\text{BP2000}$ at current densities of 10 (\blacksquare), 50 (\circ), 100 (\times), and 200 (\star) mAcm^{-2} 52

Figure 4.15 Life time performance for $\text{La}_{0.6}\text{Ca}_{0.4}\text{Co}_{0.8}\text{Ru}_{0.2}\text{O}_3/\text{BP2000}$ (\star) at current density of 10 mAcm^{-2}53

Figure 4.16 The discharging I-V polarization curves of

| | | |
|-------------|---|----|
| | $\text{La}_{0.6}\text{Ca}_{0.4}\text{Co}_{1-x}\text{Ru}_x\text{O}_3/\text{BP2000}$ | 54 |
| Figure 4.17 | The galvanostatic discharge curves for the (a) $\text{La}_{0.6}\text{Ca}_{0.4}\text{Co}_{0.8}\text{Ru}_{0.2}\text{O}_3/\text{BP2000}$ (b) $\text{La}_{0.6}\text{Ca}_{0.4}\text{Co}_{0.6}\text{Ru}_{0.4}\text{O}_3/\text{BP2000}$ (c) $\text{La}_{0.6}\text{Ca}_{0.4}\text{Co}_{0.2}\text{Ru}_{0.8}\text{O}_3/\text{BP2000}$ at current densities of 10 mAcm^{-2} (■), 50 mAcm^{-2} (△), 100 mAcm^{-2} (●), 150 mAcm^{-2} (×), and 200 mAcm^{-2} (☆)..... | 56 |
| Figure 4.18 | The I-V polarization curves of the $\text{La}_{0.6}\text{Ca}_{0.4}\text{Co}_{0.4}\text{Ru}_{0.6}\text{O}_3/\text{BP2000}$ GDE and the catalyzed GDEs with electrocatalysts of Ag/CNC, commercial EVT-Mn, and commercial EVT-MnCo..... | 57 |
| Figure 4.19 | The charging I-V polarization curves of $\text{La}_{0.6}\text{Ca}_{0.4}\text{Co}_{1-x}\text{Ru}_x\text{O}_3/\text{BP2000}$.. | 58 |
| Figure 4.20 | The galvanostatic charge curves for the (a) $\text{La}_{0.6}\text{Ca}_{0.4}\text{CoO}_3/\text{BP2000}$ (b) $\text{La}_{0.6}\text{Ca}_{0.4}\text{Co}_{0.8}\text{Ru}_{0.2}\text{O}_3/\text{BP2000}$ (c) $\text{La}_{0.6}\text{Ca}_{0.4}\text{Co}_{0.4}\text{Ru}_{0.6}\text{O}_3/\text{BP2000}$ at current densities of 10 mAcm^{-2} (■), 50 mAcm^{-2} (△), 100 mAcm^{-2} (●), 150 mAcm^{-2} (×), and 200 mAcm^{-2} (☆)..... | 60 |
| Figure 4.21 | The life time testing of the $\text{La}_{0.6}\text{Ca}_{0.4}\text{Co}_{0.4}\text{Ru}_{0.6}\text{O}_3/\text{BP2000}$ GDE for 100 h discharge followed by 100 h charge at a constant current density of 30 mAcm^{-2} | 61 |
| Figure 4.22 | The SEM images of $\text{La}_{0.6}\text{Ca}_{0.4}\text{Co}_{0.4}\text{Ru}_{0.6}\text{O}_3/\text{BP2000}$ GDE (a) before and (b) after life time testing..... | 62 |
| Figure 5.1 | X-ray results of (a) IrO_2 , (b) ACP-derived $\text{La}_{0.6}\text{Ca}_{0.4}\text{CoO}_3$, (c) $\text{La}_{0.6}\text{Ca}_{0.4}\text{CoIr}_{0.25}\text{O}_{3.5-\delta}$ from the mechanical alloying process, and (d) ACP-derived $\text{La}_{0.6}\text{Ca}_{0.4}\text{Co}_{0.8}\text{Ir}_{0.2}\text{O}_3$ | 65 |

| | |
|--|----|
| Figure 5.2 The XRD profile of the SSR-derived $\text{La}_{0.6}\text{Ca}_{0.4}\text{CoO}_3$ from SSR route. | 67 |
| Figure 5.3 The SEM image of (a) $\text{La}_{0.6}\text{Ca}_{0.4}\text{CoIr}_{0.25}\text{O}_{3.5-\delta}$ after the mechanical alloying process, (b) $\text{La}_{0.6}\text{Ca}_{0.4}\text{CoO}_3$, and (c) ACP-derived $\text{La}_{0.6}\text{Ca}_{0.4}\text{Co}_{0.8}\text{Ir}_{0.2}\text{O}_3$ | 69 |
| Figure 5.4 The EDX mapping of $\text{La}_{0.6}\text{Ca}_{0.4}\text{CoIr}_{0.25}\text{O}_{3.5-\delta}$ | 70 |
| Figure 5.5 Images for CNCs from TEM..... | 71 |
| Figure 5.6 The discharging I-V polarization curves of the noncatalyzed GDE, and catalyzed GDEs with electrocatalysts of IrO_2/CNCs , $\text{La}_{0.6}\text{Ca}_{0.4}\text{CoO}_3$, $\text{La}_{0.6}\text{Ca}_{0.4}\text{CoO}_3/\text{CNCs}$, and $\text{La}_{0.6}\text{Ca}_{0.4}\text{CoIr}_{0.25}\text{O}_{3.5-\delta}/\text{CNCs}$ | 73 |
| Figure 5.7 The charging I-V polarization curves of the noncatalyzed GDE and catalyzed GDEs with electrocatalysts of IrO_2/CNCs , $\text{La}_{0.6}\text{Ca}_{0.4}\text{CoO}_3/\text{CNCs}$, and $\text{La}_{0.6}\text{Ca}_{0.4}\text{CoIr}_{0.25}\text{O}_{3.5-\delta}/\text{CNCs}$ | 74 |
| Figure 5.8 $\text{La}_{0.6}\text{Ca}_{0.4}\text{CoO}_3/\text{CNCs}$ galvanostatic discharging curves at (a) ■ 25 and (b) ● 100 mAcm^{-2} and charging curves at (c) ◆ 25 and (d) ★ 100 mAcm^{-2} . $\text{La}_{0.6}\text{Ca}_{0.4}\text{CoIr}_{0.25}\text{O}_{3.5-\delta}/\text{CNCs}$ galvanostatic discharging curves at (a) ✕ 25 and (b) ▽ 100 mAcm^{-2} and charging curves at (c) ▷ 25 and (d) ○ 100 mAcm^{-2} | 75 |
| Figure 5.9 Oxygen reduction I-V polarization curves of MnO_x , noncatalyzed GDE, and catalyzed GDEs with $\text{La}_{0.6}\text{Ca}_{0.4}\text{Co}_{0.8}\text{Ir}_{0.2}\text{O}_3$ only, $\text{La}_{0.6}\text{Ca}_{0.4}\text{CoO}_3/\text{CNCs}$, and ACP-derived $\text{La}_{0.6}\text{Ca}_{0.4}\text{Co}_{0.8}\text{Ir}_{0.2}\text{O}_3/\text{CNCs}$ | 77 |
| Figure 5.10 Oxygen evolution I-V polarization curves of noncatalyzed GDE and | |

| | |
|--|----|
| <p>catalyzed GDEs with ACP-derived $\text{La}_{0.6}\text{Ca}_{0.4}\text{Co}_{0.8}\text{Ir}_{0.2}\text{O}_3/\text{CNCs}$, $\text{La}_{0.6}\text{Ca}_{0.4}\text{CoO}_3/\text{CNCs}$, and IrO_2/CNCs.....</p> | 78 |
| <p>Figure 5.11 Oxygen reduction I-V polarization curves of noncatalyzed GDE and catalyzed GDEs with $\text{La}_{0.6}\text{Ca}_{0.4}\text{CoIr}_{0.25}\text{O}_{3.5-\delta}/\text{CNCs}$ and ACP-derived $\text{La}_{0.6}\text{Ca}_{0.4}\text{Co}_{0.8}\text{Ir}_{0.2}\text{O}_3/\text{CNCs}$.....</p> | 79 |
| <p>Figure 5.12 Oxygen reduction I-V polarization curves of ACP-derived $\text{La}_{0.6}\text{Ca}_{0.4}\text{Co}_{0.8}\text{Ru}_{0.2}\text{O}_3/\text{CNCs}$ and ACP-derived $\text{La}_{0.6}\text{Ca}_{0.4}\text{Co}_{0.8}\text{Ir}_{0.2}\text{O}_3/\text{CNCs}$.....</p> | 80 |
| <p>Figure 5.13 Zeta potential responses for ACP-derived $\text{La}_{0.6}\text{Ca}_{0.4}\text{Co}_{0.8}\text{Ir}_{0.2}\text{O}_3$ and $\text{La}_{0.6}\text{Ca}_{0.4}\text{CoO}_3$.....</p> | 81 |
| <p>Figure 5.14 Oxygen reduction galvanostatic curves for the ACP-derived $\text{La}_{0.6}\text{Ca}_{0.4}\text{Co}_{0.8}\text{Ir}_{0.2}\text{O}_3/\text{CNCs}$ at current densities of 50 mAcm^{-2} (☆) and 100 mAcm^{-2} (○), as well as $\text{La}_{0.6}\text{Ca}_{0.4}\text{CoO}_3/\text{CNCs}$ at current densities of 50 mAcm^{-2} (▲) and 100 mAcm^{-2} (×).....</p> | 82 |
| <p>Figure 5.15 Oxygen evolution galvanostatic curves for ACP-derived $\text{La}_{0.6}\text{Ca}_{0.4}\text{Co}_{0.8}\text{Ir}_{0.2}\text{O}_3/\text{CNCs}$ at current densities of 50 mAcm^{-2} (☆) and 100 mAcm^{-2} (○), as well as $\text{La}_{0.6}\text{Ca}_{0.4}\text{CoO}_3/\text{CNCs}$ at current densities of 50 mAcm^{-2} (▲) and 100 mAcm^{-2} (×).....</p> | 84 |
| <p>Figure 5.16 The cycle life performance for the ACP-derived $\text{La}_{0.6}\text{Ca}_{0.4}\text{Co}_{0.8}\text{Ir}_{0.2}\text{O}_3/\text{CNCs}$-catalyzed GDE.</p> | 85 |
| <p>Figure 6.1 SEM images for sample (a) GA, (b) GB, (b) GC, and (d) GD.....</p> | 89 |

| | |
|---|-----|
| Figure 6.2 N ₂ adsorption/desorption isotherms of sample GA (□), GB (●), GC (☆), and GD (×)..... | 91 |
| Figure 6.3 Raman spectra for sample GA, GB, GC, and GD..... | 92 |
| Figure 6.4 CV profiles at 20 mVs ⁻¹ from sample GC in potential windows of (a) 0-0.6 V, (b) 0-0.8 V, (c) 0-1 V, and (d) empty TCE of 0-1 V, respectively..... | 94 |
| Figure 6.5 CV profiles for sample GC in potential window of 0-1 V at scan rates of 5, 10, 20, and 50 mVs ⁻¹ , respectively..... | 97 |
| Figure 6.6 CRC cruves at ±1Ag ⁻¹ in potential window of 0-1 V for sample GA, GB, GC, and GD, respectively..... | 98 |
| Figure 6.7 Variation of specific capacitance for sample GA(□), GB(●), GC(☆), GD(×), and BP2000 (▲) obtained from CRC measurements in potential window of 0-1 V at ±1Ag ⁻¹ for 3000 cycles..... | 100 |
| Figure 6.8 (a) Nyquist plots for sample GA, GB, and GC at the open circuit voltage in frequency range of 0.1-20 kHz, as well as (b) the enlarged spectra at high frequency regime. (c) is the equivalent circuit model used to fit the impedance spectra..... | 104 |

List of Symbols

| | |
|-----------------|---|
| I | Current |
| V | Potential |
| R_{CT} | Resistance from faradaic charge transfer reaction |
| CPE_p | Capacitance of constant phase element for faradaic charge transfer reaction |
| R_s | Ohmic resistance from electrolyte, carbon particles, and electrode |
| S_{BET} | BET surface area |
| S_{Micro} | Micropore surface area |
| S_{Ext} | External surface area |
| D_p | Average pore diameter |
| V_{Micro} | Micropore volume |
| V_{Pore} | Total pore volume |
| C_s | The specific capacitance |
| Q | Coulombs of discharge |
| W | Sample weight |
| ΔE , | CV potential window |
| i_c | Cathodic current density |
| v | Scan rate |
| R_s | Electrolyte resistance |
| T | Time |
| C_d | Capacitance |
| $\frac{dE}{dt}$ | Slope for discharging curve |
| W | Warburg impedance |
| CPE_{EDL} | Capacitance of constant phase element for Electrochemical double layer |
| Z | Impedance |
| Y^0 | Capacitance of associated element |
| J | Imaginary unit |
| Ω | Angular frequency of the AC signal |
| A | A dimensionless parameter for fitting purpose |

Chapter 1 Introduction

1.1 Background

Shortage of oil supply amid insatiable demands from developing countries has engendered recent escalation of oil price and accompanying commodity inflation in the market. In addition, excess accumulations of CO₂ in the atmosphere from irresponsible consumption of petroleum and coal in the past century inevitably results in rising ambient temperature, a fact known as “greenhouse effect”. Recently, R. K. Pachauri, chairman of the Intergovernmental Panel on Climate Change (IPCC) and A. A. Gore Jr. (the former U.S. Vice President) were awarded the Nobel Peace Prize on December 2007 at the Oslo City Hall due to the research of climatic change and counteraction of the global warming. Hence, the development of renewable energy has attracted considerable interests in exploring sustainable energy sources as well as green and possibly carbon-free [1].

Energy crisis is one of the most critical issues and everyone try to find the alternatives of clean energy. The renewable energy comes from natural resources including sunlight, wind, tides, rain, and geothermal heat. During past decade, worldwide renewable energy has attracted a great deal of attention on the technologies such as wind power, hydropower, solar energy, biomass, biofuel, and geothermal energy. For this purpose, numerous investigations have focused on the preparation of advanced materials followed by improving energy conversion efficiency as well as low polluting systems to be utilized in the future.

1.2 Motivations

Among many technologies proposed, solar cells, wind power, and fuel cells are recognized as the key technologies that enable a fossil-independent scenario [2-4]. Solar cells are photovoltaic devices in which photon energy from sun light is converted directly into electricity. Development of solar cells dates back to 1970s with the aim to provide electricity for space mission. Present solar cells employ Si-based designs which are robust and can sustain extended usages. However, their photovoltaic efficiencies are rather limited at $\sim 43.5\%$ [5]. Wind energy is friendly to the surrounding environment, as no fossil fuels are burnt to generate electricity from wind energy. However, the wind power is uncontrollable and it varies from zero to storm force. Therefore, wind turbines do not produce the same amount of electricity all the time. Furthermore, it should be built in the countryside due to the noisy of the wind turbines.

Fuel cells, on the other hand, the mechanism run on direct chemical energy conversion to produce electricity through chemical reaction. The operation efficiency for a fuel cell can be as high as $\sim 70\%$. The source of fuel cell is hydrogen and the hydrogen is reduced at the anode followed by positivity charged ion travel through the electrolyte to the cathode. Meanwhile, the oxygen reduction reaction occurs at the cathode and the final product is clear water. There are many type of fuel cell such as proton exchange membrane fuel cell (PEMFC), direct methanol fuel cell (DMFC), solid state fuel cell (SOFC), Molten carbon fuel cell (MCFC), phosphoric acid (PAFC), and alkaline fuel cell (AFC). In AFC system, the non-platinum catalyst can be use due to the alkaline electrolyte. Hence, first of all, this work focuses on alkaline

fuel cell technology.

In chapter 4, we employed an amorphous citrate precursor (ACP) method to synthesize the perovskite of $\text{La}_{0.6}\text{Ca}_{0.4}\text{Co}_{0.8}\text{Ru}_{0.2}\text{O}_3$ and evaluated its catalytic abilities for the ORR in an alkaline electrolyte. Material characterization, H_2O_2 decomposition, and electrochemical analysis were carried out to determine relevant properties. Furthermore, we synthesized the perovskite of $\text{La}_{0.6}\text{Ca}_{0.4}\text{Co}_{1-x}\text{Ru}_x\text{O}_3$ ($x=0, 0.2, 0.4, 0.6, 0.8,$ and 1) by a solid-state reaction (SSR) method and determined $\text{La}_{0.6}\text{Ca}_{0.4}\text{Co}_{0.4}\text{Ru}_{0.6}\text{O}_3$ to possess superior bi-functional catalytic activity for the oxygen reduction and evolution. In this chapter 5, we reported the synthesis of $\text{La}_{0.6}\text{Ca}_{0.4}\text{CoIr}_{0.25}\text{O}_{3.5-\delta}$ and $\text{La}_{0.6}\text{Ca}_{0.4}\text{Co}_{0.8}\text{Ir}_{0.2}\text{O}_3$, as well as the evaluation on their performances as bi-functional electrocatalysts in alkaline electrolyte using carbon nanocapsules (CNCs) as the catalyst support. In addition, electrochemical characterizations were carried out on $\text{La}_{0.6}\text{Ca}_{0.4}\text{CoO}_3$ serving as the reference.

On the other hand, how to storage energy for renewable system is an interesting issue. For energy storage, the supercapacitor is one of the most promising systems due to their numerous features such as high power, high energy density, and long cycle life time [6,7]. It is well know that desirable EDLCs require large surface areas with appropriate pore sizes for facile access of ions from the electrolyte during capacitive charging and discharging. This can be realized by fabricating suitable carbon skeletons followed by a deliberate activation step to remove atomic carbon selectively. In the chapter 6, we explore the preparation of RF-derived ambient gels in conjunction with CO_2 treatment for surface activation so an excessive surface area and suitable pore size can be obtained. The resulting materials are subjected to electrochemical measurements using a titanium cavity electrode (TCE) to determine

their intrinsic capacitive behaviors and relevant kinetic parameters.



Chapter 2 Literature Review

2.1 Alkaline fuel cells

Alkaline fuel cells are regarded as desirable clean energy alternatives to traditional fuels, and they may serve as solutions to ameliorate worsening greenhouse effect [8,9]. The alkaline fuel cell is the first successfully developed fuel cells, whose use date back to 1960s in Apollo space shuttle. The structure of an alkaline fuel cell is shown in Fig. 2.1 [10]. The electrolytes used are alkaline solutions such as KOH or NaOH. Pure hydrogen as the fuel oxidizes at the anode, while air or pure oxygen as the oxidant reduces at the cathode. The fuel cell operates through a redox reaction between hydrogen and oxygen following the equations:



The energy conversion efficiency of alkaline fuel cell is high, up to 70%, which is mainly because the oxygen reduction reaction rate is faster in the alkaline electrolyte than that in acidic electrolyte. Besides, the alkaline fuel has another advantage that non-platinum-group catalysts can be used in the system. However, the air is widely used as the oxidant in alkaline fuel cells, but aqueous alkaline solutions do not reject CO₂. The fuel cells could become “poisoned” through the conversion of KOH to K₂CO₃, resulting in reduced lifetime and efficiency. There are several ways

to conquer CO₂ poisoning problems such as adding filters before inputting air to the electrode, applying the electrochemical methods to eliminate CO₂, cycle purification electrolyte, and using pure oxygen as the oxidant.

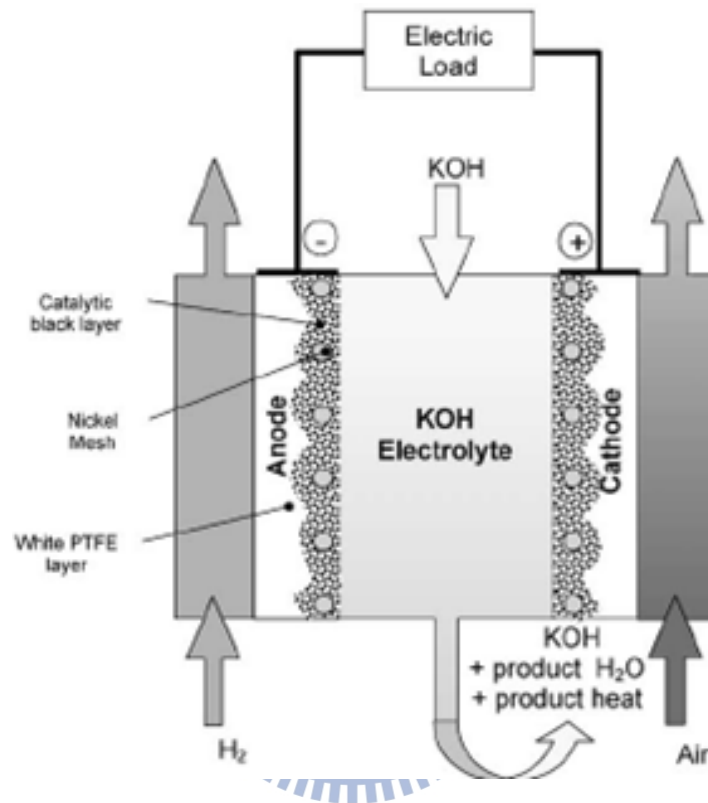


Figure 2.1 The structure of an alkaline fuel cell [10].

2.2 Perovskite structure

The perovskite structure is a compound with an ABO₃ formula as shown in Fig. 2.2 [11]. In the structure, the oxygen ion and cation A form a close packed structure, while the cation B with a smaller size occupies the body-center position. Perovskites have many derivatives by substituting different atoms into A and B sites. For example, the A site can be alkaline earth metals such as La, Ca, and Sr. On the other hand, at the

B site transition metals such as Mn, Co, Ir, and Cu can be used. Therefore, Ca and Sr can be incorporated into perovskite occupying the A site forming $\text{La}_{1-x}\text{Ca}_x\text{CoO}_3$ and $\text{La}_{1-x}\text{Sr}_x\text{CoO}_3$ perovskite structures.

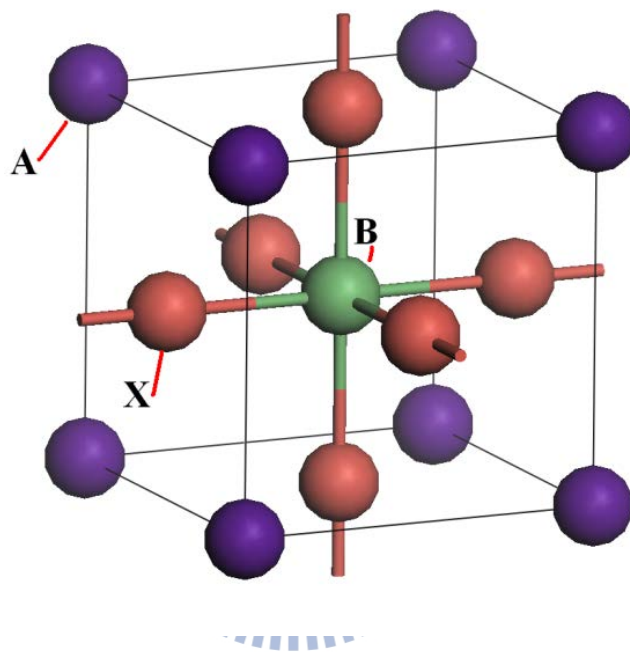


Figure 2.2 The structure of perovskite with a chemical formula ABO_3 [11].

Nowadays, the Ca doped LaCoO_3 perovskite has been exploited as the electrocatalyst in many researches. The $\text{La}_{0.6}\text{Ca}_{0.4}\text{CoO}_3$ has also been exhibited as a bi-functional electrocatalyst with good performances. A wide variety of transition metal ions have been explored for partial replacements at the Co^{3+} sites to improve the oxygen reduction reaction (ORR) kinetics [12,13]. Recently, we synthesized the $\text{La}_{0.6}\text{Ca}_{0.4}\text{CoIr}_{0.25}\text{O}_{3.5-\delta}$ and $\text{La}_{0.6}\text{Ca}_{0.4}\text{Co}_{0.8}\text{Ir}_{0.2}\text{O}_3$, which demonstrate improved performances for both the ORR and oxygen evolution reaction over those of $\text{La}_{0.6}\text{Ca}_{0.4}\text{CoO}_3$ [14,15]. We realize that the successful incorporation of Ir^{4+} at the Co^{3+}

sites is responsible for the catalytic enhancements. Because metallic Ru is known as an ORR electrocatalyst, a similar strategy can be employed to introduce Ru³⁺ at the Co³⁺ sites for possible catalytic reactions [16,17]. The perovskite lattice is expected to provide a stable platform for hosting Ru³⁺. As a result, a reduced amount of Ru is used as opposed to the metallic form.

2.3 Oxygen reduction reaction

ORR is a critical step in fuel cell electrochemistry because a significant overpotential is often required to activate the relatively stable oxygen molecules [18]. Conventional fuel cells involve an acidic electrolyte, noble metals and alloys such as Pt and Pt₃Ni are selected for their chemical inertness [19,20]. However, to reduce the system cost it is necessary to adopt less-expensive materials with comparable performances [21,22]. The ORR in an alkaline electrolyte reveals less polarization loss, leading to a fuel cell with better efficiency [23]. In an alkaline solution, the ORR occurs *via* direct four-electron pathway or two electron peroxide route listed below [24];



The straightforward route is known as the four-electron pathway in which the

oxygen molecule reacts with water and four electrons in a single step to form hydroxyl ions directly (2-4). An alternative one is the peroxide pathway where the oxygen molecule accepts two electrons and water in the first step to convert to peroxide ions (2-5). Subsequently, the peroxide ions react with two more electrons and water leading to the formation of hydroxyl ions (2-6), or decomposition to form hydroxyl ion and oxygen (2-7). In addition, the electrocatalysts that reduce oxygen through the four electron pathway are preferred because less electrode polarization is expected. Many materials have been investigated as an electrocatalyst to enhance the ORR. They include metals (Pt, Ag) [25-30], metal oxides (RuO_2 , MnO_2 , CoO) [31-33], perovskites (LaCoO_3 , $\text{La}_{0.6}\text{Ca}_{0.4}\text{CoO}_3$) [34-38], spinels ($\text{Ni}_x\text{Al}_{1-x}\text{Mn}_2\text{O}_4$, $\text{Ni}_2\text{Co}_2\text{O}_4$, $\text{Mn}_{3x}\text{Co}_{3-3x}\text{O}_4$) [39-41], as well as pyrolyzed N-4 chelate compounds (CoTMPP) [42]. A thorough review was provided recently by Wang, discussing available non-platinum electrocatalysts [43]. Because perovskite is established as the two-electron catalyst, the decomposition of H_2O_2 can be selected as a litmus test for quick catalytic evaluations [44]. For example, Jiang *et al.* studied the ORR ability for cobalt oxide/graphite air electrodes by determining their homogeneous and heterogeneous rate constants for the H_2O_2 decomposition [45]. Because the transition metal ions are the active species for the ORR, Falcón *et al.* adopted a similar technique to correlate the oxidation states of Ni and Fe in $\text{LaFe}_x\text{Ni}_{1-x}\text{O}_{3+\delta}$ [46]. Thus, the novel perovskites were chosen in this research work in alkaline fuel cells.

2.4 Bi-functional electrocatalysts

Oxygen reduction and evolution are critical electrochemical reactions in many industrial applications [47,48]. For example, in solid oxide fuel cells cathode oxygen

reduction is the most energy-consuming step and responsible for the largest polarization loss [49]. Likewise, oxygen evolution poses serious challenges in chlor-alkali productions and water electrolysis cells [48,50]. To accelerate electrochemical reactions, electrocatalysts are used and they are typically designed and synthesized for single purpose only. However, in particular systems such as rechargeable metal-air, air-metal hydride, and regenerative fuel cell, bi-functional electrocatalysts are required [51-53]. An excellent review was provided recently by Jörissen detailing materials selection and construction principle of bi-functional oxygen-air electrodes [54]. Conventional fabrication methods for bi-functional gas diffusion electrodes (GDE) entail lamination of current collector, carbonaceous materials impregnated with suitable electrocatalysts, and polytetrafluorethylene (PTFE) resin.

Oxides including perovskites (ABO_3), spinels (AB_2O_4), and pyrochlores ($A_2B_2O_7$) have been investigated extensively for their bi-functional catalytic abilities in alkaline electrolyte [55,56]. Among them, the perovskites have received considerable attention because of reasonable electrical conductivity and corrosion resistance. Previously, Bockris and Otagawa had conducted comprehensive analysis on electrocatalysis in perovskites [38]. Among the plausible candidate materials, the lanthanum cobaltate ($LaCoO_3$) was documented widely in literatures for its simple synthesis and incorporation of various dopants in a wide variety of compositions [57-60]. Tiwari *et al.* suggested that B site cation (i.e., Co^{3+}) in $LaCoO_3$ directly contributes to the catalytic performances [61]. As a result, many efforts including introduction of additional cations, as well as controlling the degree of oxygen vacancies were engaged to manipulate oxidation states of Co. To date, $La_{0.6}Ca_{0.4}CoO_3$

has demonstrated impressive characteristics and thus can be found in many cell samples [62,63].

Iridium oxide (IrO_2) is used as the dimensionally stable anode in chlor alkali cells [55]. It processes the rutile structure where the Ir^{4+} is coordinated by six neighboring oxygen atoms forming an octahedron. Surprisingly, the IrO_2 exhibits excellent electrical conductivity and corrosion resistance, that are desirable for many catalytic reactions. For example, De Pauli and Trasatti prepared mixed oxides of IrO_2 and SnO_2 and reported impressive behaviors of oxygen evolution in acid electrolyte [64]. Unfortunately, implementation of IrO_2 for oxygen evolution in alkaline electrolyte is less studied due to the concerns on possible dissolution [65]. Because of similar octahedral coordination of Ir^{4+} in IrO_2 and Co^{3+} in LaCoO_3 , it would be interesting to explore possible replacements of Ir^{4+} at Co^{3+} sites in perovskite matrix. In this way, we expect the perovskite structure provides the necessary chemical stability in alkaline electrolyte while the Ir^{4+} contributes to the oxygen evolution.

2.5 Gas diffusion electrodes and electrocatalyst support materials

A gas diffusion electrodes (GDE) is required for fuel cells and metal air batteries. The GDE is a porous platform incorporating current collector, hydrophobic polytetrafluoroethylene (PTFE) resin and carbonaceous material impregnated with catalytic nanoparticles [66,67]. The porosity, pore structure, and hydrophobicity of the GDE must be carefully designed to allow an extensive reaction interface between the gaseous oxygen and liquid electrolyte in the vicinity of the electrocatalyst. To date, it

is recognized that the GDE is the crucial component enabling successful implementation of fuel cells.

Many carbonaceous materials have been investigated as possible electrocatalyst supports [68-70]. They range from conventional carbon powders such as Vulcan XC72, Black Pearls, Shawiningan Blacks and active carbons, to less familiar ones including glassy carbons, carbon fibers and hard carbon spherules [71-73]. A detailed discussion was recently provided by Dicks [74]. With recent progress in the synthesis of nanostructured materials, exotic forms of carbon such as carbon nanotubes (CNTs) and carbon nanocapsules (CNCs) have been reported [75,76]. The CNTs exhibit extraordinary physical properties such as mechanical strength, excellent electronic and thermal conductivity, as well as chemical stability and high surface area. These are desirable physical properties for electrocatalyst supports. Hence, the CNTs' applicability as an electrocatalyst support has received much attention recently. For example, Kongkanand *et al.* observed significant enhancements in the electrocatalytic activities of single-walled CNTs decorated with Pt nanoparticles [77]. A similar result was reported by Che *et al.* and they attributed the enhanced capabilities to the accessible inner surface of CNTs [78]. In addition, the strategy of hybrid carbonaceous materials has been explored. Huang *et al.* mixed active carbons with the CNTs and observed substantial improvements in electrocatalytic performance once Pt was loaded [79].

2.6 Supercapacitors

Supercapacitors have attracted considerable attention recently because they

possess the advantages in power output, energy density, and cycle life compared with conventional rechargeable batteries, for the applications in electric vehicles, power tools and uninterrupted power systems [80-91]. From the standpoint of operation mechanism, there are two types of supercapacitors; EDLCs and pseudocapacitors. The EDLCs store charges *via* ions adsorption/desorption at the interface between the electrode and electrolyte [84-88, 92,93]. In contrast, the pseudocapacitors entail facile faradaic reactions occurring on the electrode material to store charges in different oxidation states such as hydrous RuO_2 , V_2O_5 , NiO , and MnO_2 [94-106]. For example the hydrous RuO_2 exhibits the best performance resulting from its distinctive characteristics of highly reversible and fast faradaic reaction mechanism, high specific capacitance, and very good conductivity.

Among them, the pseudocapacitors are able to deliver larger capacitances but with cost premium and relatively short cycle life. Therefore, there have been considerable interests in exploring alternative electrode materials. Carbonaceous materials are the electrode materials used in the majority of commercially available EDLCs, possessing the advantages of low cost and long cycle life. Besides, specific capacitor of EDLC can be increased by using organic electrolytes [107-109]. Since the charge/discharge reaction on the electrode surface provides a shorter ions moving path without chemical reaction, the EDLC exhibits a low internal resistance through interactive-free electrodes. As a result, EDLC conducts non-faradaic process, which is completely reversible under a higher power density. Besides, material properties including surface area, pore sizes, pore size distribution, surface functional group and electrolyte window can be controlled to improve EDLC [110,111]. For the EDLCs, the capacitive responses are proportional to the effective surface area available for

ions adsorption/desorption so an excessive surface area with a desirable porosity for the electrode material is necessary. To date, considerable efforts have devoted to the carbon-based materials since their rich varieties exhibit a wide range of pore sizes, surface areas, electric conductivities, and surface properties. In literature, carbonaceous materials including active carbons, carbon blacks, glassy carbons, and nanostructured carbons (carbon nanotubes, nanocapsules, nanofibers, gels) have been investigated [112-119]. Among them, the carbon xerogels and aerogels possess unique properties of extremely low density and high porosity [120,121].

2.7 Resorcinol-formaldehyde carbon gels

The carbon xerogels and aerogels are synthesized *via* a sol-gel process in which precursors in liquid states are properly mixed, and condense to form continuous colloidal networks, followed by solvent removal and pyrolysis to obtain a porous carbon structure with interconnected channels. One of the sol-gel approaches that has been studied extensively is the polycondensation of resorcinol ® and formaldehyde (F) [120-122]. According to Elkhatat and Al-Muhtaseb [123], the concentrations of the precursors, catalysts, solvents, and pH value play important roles in determining the resulted morphologies and porosities of the gel structures. In addition, the solvent removal step for the wet gels is critical because the drag of surface tension induces contraction of the colloidal networks resulting in substantial reduction in the pore size. So far, many R-F derived porous carbons have been prepared and evaluated for possible applications in EDLCs, catalysis (as a catalyst support), filtration, gas separation, and adsorption [121, 123,124].

Previously, many RF-derived xerogels and aerogels have been synthesized and evaluated for capacitive behaviors [125,126]. The preparation of xerogels involves direct solvent evaporation that engenders notable structural contraction and possible collapse at the extreme case. As a result, after pyrolysis the carbon xerogels typically contain 25% porosity with reveal a moderate surface area ($150\text{-}900\text{ m}^2\text{g}^{-1}$) and small pores (1-10 nm) [127]. In contrast, the carbon aerogels experience a supercritical drying step that sublimates the solvents with negligible shrinkage of carbon networks. After pyrolysis, the carbon aerogels demonstrate a substantially larger surface area and pore volume, and consequently, a larger capacitance [127-129]. Despite of those merits, the carbon aerogels are of little commercial interest because the supercritical drying is energy-consuming and improper for production in large quantity. On the other hand, the carbon xerogels suffer from unnecessary structure alteration and hence, their pore size and pore volume are not adequate for EDLC applications. An alternative preparation route to minimize structure contraction during sol-gel transformation is *via* repeated solvent exchanges that reduce the surface tension of the solvent sequentially in the wet gels [126]. In this way, the solvent with reduced surface tension is able to evaporate slowly rendering a dried gel known as “ambient gel” whose structure is closely resemble to that of aerogel. This enables a large number of mesopores and macropores in the carbon skeleton. This ambient gel could be of potential interest because its desirable surface area and porosity, as well as the simple drying process.

Chapter 3 Experimental

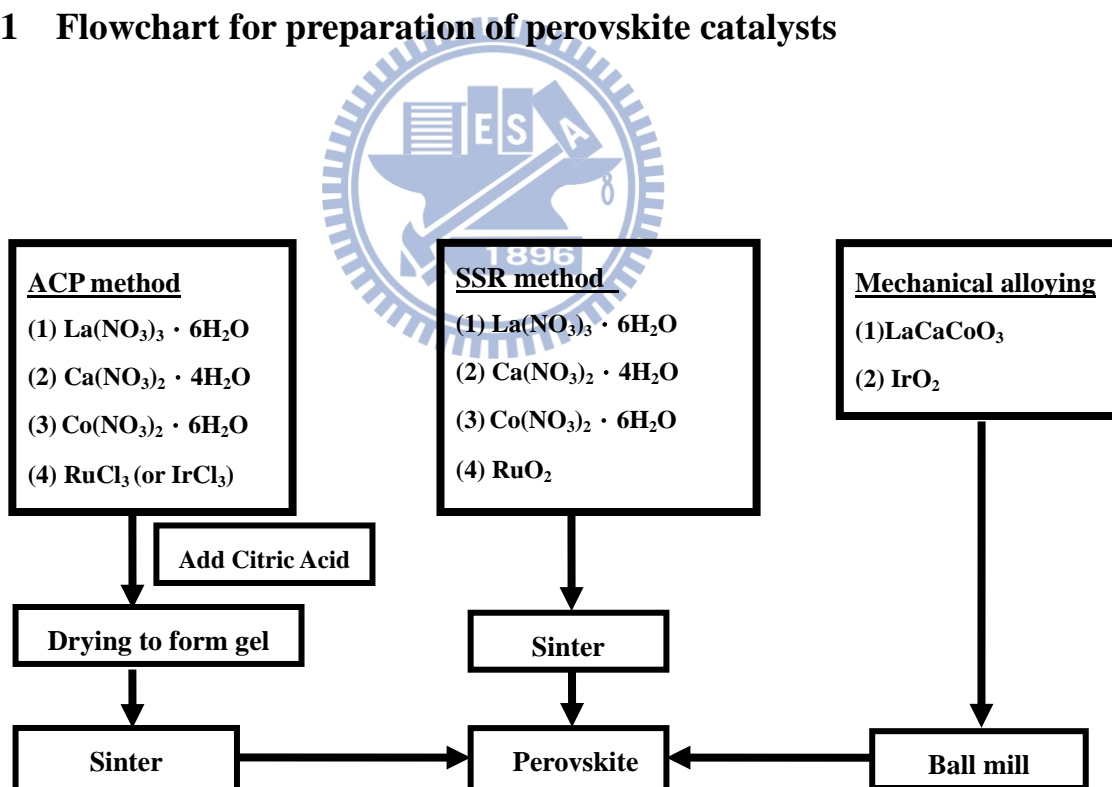
3.1 Materials

| | Materials | Source | Purity |
|-----|--|---------------|---------|
| 1. | La(NO ₃) ₃ •6H ₂ O | Alfa aesar | 99.9 % |
| 2. | Ca(NO ₃) ₂ •4H ₂ O | Showa | 98 % |
| 3. | Co(NO ₃) ₃ •6H ₂ O | Riedel-deHaen | 99 % |
| 4. | RuCl ₃ •nH ₂ O | Sigma-aldrich | 99.99 % |
| 5. | RuO ₂ | Alfa aesar | 99.95% |
| 6. | IrCl ₃ •nH ₂ O | Sigma-aldrich | 99.98% |
| 7. | IrO ₂ | Alfa aesar | 99.99 % |
| 8. | Citric acid | Sigma-aldrich | 99.5 % |
| 9. | KOH | Showa | 85 % |
| 10. | H ₂ O ₂ | Riedel-deHaen | 35 % |
| 11. | Vulcan XC-72 | Cabot | - |
| 12. | Black pearl 2000 | Taipower | - |
| 13. | Polytetrafluoroethylene (T-30) | Dupont | 60 % |
| 14. | Polyvinyl alcohol (Mw=2,000–12,000) | Sigma-aldrich | 99+ % |
| 15. | Gas diffusion electrode | eVionyx Lic. | |
| 16. | Zn rod | 奇峰五金行 | 99.99 % |
| 17. | Resorcinol | Acros | 98 % |

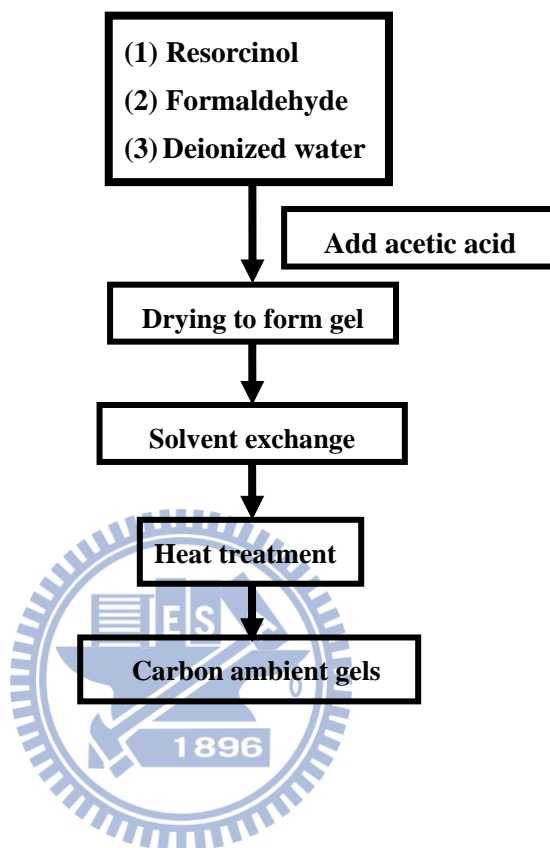
| | | | |
|-----|--------------|---------------|--------|
| 18. | Formaldehyde | J. B. Baker | 37 % |
| 19. | Acetic acid | Sigma-aldrich | 99.7 % |
| 20. | Acetone | Sigma-aldrich | 99.9 % |
| 21. | Cyclohexane | Sigma-aldrich | 99.5 % |
| 22 | AC1100 | Taipower | |

3.2 Experimental flowchart

3.2.1 Flowchart for preparation of perovskite catalysts



3.2.2 Flowchart for preparation of carbon ambient gels



3.3 Synthesis of ACP-derived $\text{La}_{0.6}\text{Ca}_{0.4}\text{Co}_{0.8}\text{Ru}_{0.2}\text{O}_3$ and $\text{La}_{0.6}\text{Ca}_{0.4}\text{Co}_{0.8}\text{Ir}_{0.2}\text{O}_3$

The ACP method was adopted to prepare stoichiometric $\text{La}_{0.6}\text{Ca}_{0.4}\text{Co}_{0.8}\text{Ru}_{0.2}\text{O}_3$ (or $\text{La}_{0.6}\text{Ca}_{0.4}\text{Co}_{0.8}\text{Ir}_{0.2}\text{O}_3$) perovskite in which $\text{La}(\text{NO}_3)_3 \cdot 6\text{H}_2\text{O}$, $\text{Ca}(\text{NO}_3)_2 \cdot 4\text{H}_2\text{O}$, $\text{Co}(\text{NO}_3)_3 \cdot 6\text{H}_2\text{O}$, and $\text{RuCl}_3 \cdot n\text{H}_2\text{O}$ (or $\text{IrCl}_3 \cdot x\text{H}_2\text{O}$) were dissolved at a proper ratio in excess deionized water with citric acid. The molar ratio for the citric acid to the metal ions was 1:1. The mixture underwent moderate heating and stirring at 80°C for 6 h to form a viscous gel, followed by oven drying for 24 h. Subsequently the dry gel was

ignited in air to burn off polymeric precursors, forming a dark aggregate. Afterward, the sample was subjected to a heat treatment in air at 650°C for 4 h to form fine powders designated as ACP-derived $\text{La}_{0.6}\text{Ca}_{0.4}\text{Co}_{0.8}\text{Ru}_{0.2}\text{O}_3$ and ACP-derived $\text{La}_{0.6}\text{Ca}_{0.4}\text{Co}_{0.8}\text{Ir}_{0.2}\text{O}_3$.

3.4 Synthesis of SSR-derived $\text{La}_{0.6}\text{Ca}_{0.4}\text{Co}_x\text{Ru}_{1-x}\text{O}_3$

Perovskite-type oxides $\text{La}_{0.6}\text{Ca}_{0.4}\text{Co}_{1-x}\text{Ru}_x\text{O}_3$ ($x=0, 0.2, 0.4, 0.6, 0.8, \text{ and } 1$) were synthesized by SSR method. $\text{La}(\text{NO}_3)_3 \cdot 6\text{H}_2\text{O}$, $\text{Ca}(\text{NO}_3)_2 \cdot 4\text{H}_2\text{O}$, $\text{Co}(\text{NO}_3)_2 \cdot 6\text{H}_2\text{O}$, as well as RuO_2 were thoroughly mixed by a mortar and pestle followed by a two-stage sintering process including 600°C in the air for 4 h and 800°C in air for 4 h, respectively.

3.5 Synthesis of $\text{La}_{0.6}\text{Ca}_{0.4}\text{CoIr}_{0.25}\text{O}_{3.5-\delta}$

The $\text{La}_{0.6}\text{Ca}_{0.4}\text{CoIr}_{0.25}\text{O}_{3.5-\delta}$ perovskite powders were prepared by mechanical alloying of IrO_2 (99.99% Alfa Aesar) and $\text{La}_{0.6}\text{Ca}_{0.4}\text{CoO}_3$ at a molar ratio of 1:4. The $\text{La}_{0.6}\text{Ca}_{0.4}\text{CoO}_3$ was synthesized by ACP method where proper ratios of $\text{La}(\text{NO}_3)_3$, $\text{Ca}(\text{NO}_3)_2$, and $\text{Co}(\text{NO}_3)_2$ were dissolved in water and citrate acid first, and followed by initial drying to form a gel. A sintering process was carried out at 650°C in air for 4 h to obtain particles with desirable composition of $\text{La}_{0.6}\text{Ca}_{0.4}\text{CoO}_3$. Mechanical alloying of IrO_2 and $\text{La}_{0.6}\text{Ca}_{0.4}\text{CoO}_3$ was conducted with a planetary high energy ball mill in air atmosphere containing ZrO_2 balls for 12 h. Each batch included 1.6 g $\text{La}_{0.6}\text{Ca}_{0.4}\text{CoO}_3$ and 0.4 g IrO_2 .

3.6 Fabrication of gas diffusion electrodes

The gas diffusion electrode (GDE) catalytic layer was fabricated by mixing 30 wt % perovskite catalysts, 30 wt % poly(tetrafluoroethylene) (Dupont T-30), 10 wt % poly(vinyl alcohol) ($M_w=2,000-12,000$), and 30 wt % carbonaceous materials (Vulcan XC72R (VXC72R), carbon nanocapsules (CNCs), and black pearl 2000 (BP2000)) in 10 mL deionized water at 10^4 rpm for 5 min to render a homogeneous slurry. Subsequently, the slurry was brush-painted repeatedly onto a commercially available GDE (eVionyx, Inc.) to reach a catalyst loading of 2.4 and 4.8 mg cm^{-2} . Next, the catalyzed GDE was heated at 350°C for 30 min to remove residual solvents. Afterward, the sample was rolled and pressed into a thickness of 300 μm .

3.7 Synthesis of carbon ambient gels

The carbon ambient gel was prepared by a condensation reaction between R and F, followed by solvent exchange and CO_2 activation to render an excessive surface area. First, R and F (37 wt%) were mixed in a 1:2 molar ratio in deionized water under ultrasonication for 10 min at 26°C . After complete dissolution of resorcinol, acetic acid was added as a catalyst to promote the condensation reaction forming colloids in the mixture. Subsequently, the mixture was sealed in a container at 70°C for 72 h with constant vibration to allow the transformation from a sol suspension to a wet gel. After gelation, the sample was removed from the oven and washed for 72 h in which 50% of acetone was drained and replaced with fresh acetone every 24 h. Next, the process was repeated again for another 72 h with cyclohexane. These solvent

exchange steps were conducted at 26°C so the surface tension for the liquid phase was reduced sequentially to minimize structural contraction for the solid phase upon solvent evaporation. Afterward, the sample was dried at 26 °C for 24 h to evaporate remaining cyclohexane, leaving a free-standing dark orange ambient gel. Finally, the ambient gel was placed in a tube furnace for two-stage heat treatments. The first stage was performed in Ar atmosphere at 950 °C for 1 h to decompose organic residues (pyrolysis reaction) where the dark orange ambient gel shrunk significantly to become the black porous carbon. In the second stage, at 950°C the CO₂ was purged and 99.99% CO₂ was introduced for 3 h to activate the surface of the porous carbon. By adjusting precursor and catalyst concentration, we were able to prepare ambient gels with various porosities and surface areas. The resulting samples were designated as GA, GB, and GC, respectively. The exact amounts for the precursors, catalyst, deionized water, as well as ratios for the R/C and R/W are listed in Table 3.1. In order to distinguish the effect of CO₂ activation, we also carried out identical sample preparation steps except the CO₂ activation was replaced with Ar treatment for another 3 h (labeled as GD as a reference sample).

Table 3.1 Precursors and catalyst used for the synthesis of carbon ambient gels.

| | | GA | GB | GC | GD |
|-------------|----------------------------------|-------|-------|-------|-------|
| Precursors | R: resorcinol (g) | 9.25 | 14.75 | 14.75 | 14.75 |
| | F: formaldehyde (g) | 5.05 | 8.04 | 8.04 | 8.04 |
| Catalyst | C: acetic acid (μL) | 965 | 1533 | 766.5 | 766.5 |
| Solvent | W: deionized water (g) | 50 | 50 | 50 | 50 |
| | R:F | 1:2 | 1:2 | 1:2 | 1:2 |
| Molar ratio | R:C | 5:1 | 5:1 | 10:1 | 10:1 |
| | R:W | 1:5.4 | 1:3.4 | 1:3.4 | 1:3.4 |
| | Burn-off ^a (wt%) | 95.3 | 95.3 | 96.4 | 88.3 |

^a total weight loss of carbon ambient gels after 950 °C pyrolysis and CO₂ activation.

3.8 Material characterization

3.8.1 X-ray diffraction (XRD)

A Siemens D5000 X-ray diffractometer with the wavelength of Cu-K α radiation of 0.154 nm was used to identify relevant phase and crystallinity of the synthesized powders.

3.8.2 Scanning electron microscope (SEM)

Their morphologies were observed by a scanning electron microscope (SEM, JEOL JSM-6700F and JSM-6500F).

3.8.3 Brunauer, Emmett, and Teller (BET)

The surface area was obtained by Brunauer, Emmett, and Teller (BET) method by Micromeritics Tristar 3000, Micromeritics ASAP2020 and Quantachrome NOVA-1000A. A density function theory (DFT) program was employed to estimate relevant parameters in pore size and pore distribution.

3.8.4 Pycnometers measurement

The values for density was obtained by using AccuPyc 1340 (Micromeritics).

3.8.5 zeta potential

The zeta potential results were obtained by a NICOMO 380ZLS.

3.8.6 Raman spectroscopy

Raman spectroscopy (Raman spectrometer LabRAM HR800) was performed on the sample to examine their crystallinity.

3.8.7 H₂O₂ decomposition measurement

A H₂O₂ decomposition measurement was employed to evaluate the catalytic ability for the ORR. Small amounts of La_{0.6}Ca_{0.4}Co_{0.8}Ru_{0.2}O₃ powders (0.01, 0.015, 0.02, 0.025, and 0.03 g) were suspended in 30 mL of 13 wt % KOH aqueous solution for 10 min at 25°C, followed by injection of 1.15 M H₂O₂ solution of 2 mL. The amount of O₂ released was carefully collected as a function of time.

3.9 Electrochemical measurements

3.9.1 Gas diffusion electrode (GDE)

Electrochemical analysis was conducted with a Solartron SI1287 potentiostat for oxygen reduction and evolution in I-V polarizations, galvanostatic measurements, and life time determination. The GDE (3 cm^2), serving as the working electrode, was exposed to ambient air on the back side. A Ti mesh coated with $\text{RuO}_2/\text{IrO}_2$ was used as the counter electrode, and a Zn rod (99.99 wt%) (or Ag/AgCl) was selected as the reference electrode. The Zn rod was chosen because its reading indicated the operating voltage of a zinc-air cell. A 7 M KOH aqueous solution was used as the electrolyte. The I-V polarization curves were measured at 1 mAs^{-1} . Impedance analysis was carried out using a Solartron SI1255B with a 10 mV stimulus for the frequency range of 0.1-20 kHz at the open-circuit voltage, and overpotentials of -100 , -200 and -300 mV. The recorded spectra were fitted by the ZView software to determine their respective charge transfer resistances and relevant kinetic parameters. Galvanostatic profiles were obtained for current densities of 10, 50, 100, and 200 mAcm^{-2} . Two kinds of life time test. First, the GDE was subjected to 10 mAcm^{-2} and the resulting voltage was recorded. On the other hand, the GDEs experienced repeating sequences of oxygen reduction (0.5 h), resting (1 h), oxygen evolution (0.5 h), and resting (1 h) at 25 mAcm^{-2} with a constant inflow of CO_2 -filtered air. Identical procedures were conducted on the ACP-derived $\text{La}_{0.6}\text{Ca}_{0.4}\text{CoO}_3$ for comparison purpose. In addition, the electrochemical measurements were carried out on the $\text{La}_{0.6}\text{Ca}_{0.4}\text{CoO}_3$ and IrO_2 serving as the reference. The $\text{La}_{0.6}\text{Ca}_{0.4}\text{CoO}_3$ was synthesized from the amorphous citrate precursor method (ACP) and its synthetic details were

reported elsewhere [37]. All the electrochemical experiments were performed at 25°C .

3.9.2 Titanium Cavity Electrode (TCE)

For electrochemical analysis to determine the double layer capacitance, a three-electrode cell was used in which a J-shape TCE, with 2 mm in diameter and 200 mm in length, was adopted as the working electrode. The bottom of the TCE contained a cylindrical cavity with 1 mm in diameter and 1 mm in depth for sample loading. The sample was placed on a glass sheet and pressed compactly to fill the bottom cavity. The exact weight was measured by a microbalance with an accuracy of 2-3 μg . Details on the TCE and its testing results on commercially available carbon blacks have been reported earlier [109]. Pt foil ($2 \times 5 \text{ cm}^2$) and Ag/AgCl were used as the counter and reference electrodes, respectively. Values for the double layer capacitance were determined *via* CV measurement and current reversal chronopotentiometry (CRC) in 0.5 M H_2SO_4 aqueous solution at 26 °C using a Solartron SI1287 potentiostat and 1255B frequency response analyzer. The CV profiles were recorded at scan rates of 5, 10, 20, and 50 mVs^{-1} , in potential windows of 0-0.6, 0-0.8, and 0-1 V, respectively. The CRC measurements were carried out at $\pm 1 \text{ Ag}^{-1}$ in a potential window of 0-1 V. In life time test, the sample was subjected to repeated CRC scans at $\pm 1 \text{ Ag}^{-1}$ in a potential window of 0-1 V. Impedance spectra were obtained at the open circuit voltage with a sinusoidal signal of 10 mV at frequencies between 0.1 and 20 kHz. The resulting spectra were fitted by a ZView software to retrieve relevant electrochemical parameters.

Chapter 4 Synthesis and Characterization of $\text{La}_{0.6}\text{Ca}_{0.4}\text{Co}_x\text{Ru}_{1-x}\text{O}_3$ for Bi-functional Electrodes

4.1 Physico-chemical characterizations

4.1.1 ACP-derived $\text{La}_{0.6}\text{Ca}_{0.4}\text{Co}_{0.8}\text{Ru}_{0.2}\text{O}_3$

Successful formation of polycrystalline perovskite phase from the ACP approach is known to depend on a variety of factors including the source of salts and their molar ratios, the type of chelating acids, pH value of precursor, as well as the sintering temperature, time, and atmosphere. In general, a higher sintering temperature is always preferred for an impurity-free perovskite phase, albeit with a significantly reduced surface area. However, in this work we attempt to synthesize perovskite $\text{La}_{0.6}\text{Ca}_{0.4}\text{Co}_{0.8}\text{Ru}_{0.2}\text{O}_3$ powders for ORR catalytic actions. Subsequently, the as-synthesized powders are impregnated onto the carbonaceous supports for electrochemical evaluations. Hence, a reasonable surface area for $\text{La}_{0.6}\text{Ca}_{0.4}\text{Co}_{0.8}\text{Ru}_{0.2}\text{O}_3$ powder is necessary. According to previous studies, in similar ACP routes, the perovskite phase can be formed at temperatures as low as 550-650°C [13,61,130-134]. We select a sintering process of 650°C for 4 h in air, hoping to reach a balance between crystallinity and surface area. To further confirm the sintering temperature of 650°C is appropriate, we conduct a thermogravimetric analyzer (TGA) on the polymeric precursors of $\text{La}_{0.6}\text{Ca}_{0.4}\text{Co}_{0.8}\text{Ru}_{0.2}\text{O}_3$ and its result is provided in Fig. 4.1. Apparently, there are three distinct regimes of weight loss for temperature range

of 25-800°C, which is typical for the ACP process. In the first regime of 25-300°C, the rapid weight loss is associated with the preliminary breakdown of organic components and solvent evaporation. In the second regime of 300-400°C, the notable weight loss is attributed to the decomposition of organic components and initial formation of oxide phase. In the last regime of 400-650°C, there appears a gradual weight loss as the perovskite phase is formed with improving crystallinity. Notably, there appears a negligible weight loss after 650°C. This sintering temperature is confirmed by a TGA conducted on the polymeric precursors of $\text{La}_{0.6}\text{Ca}_{0.4}\text{Co}_{0.8}\text{Ru}_{0.2}\text{O}_3$.

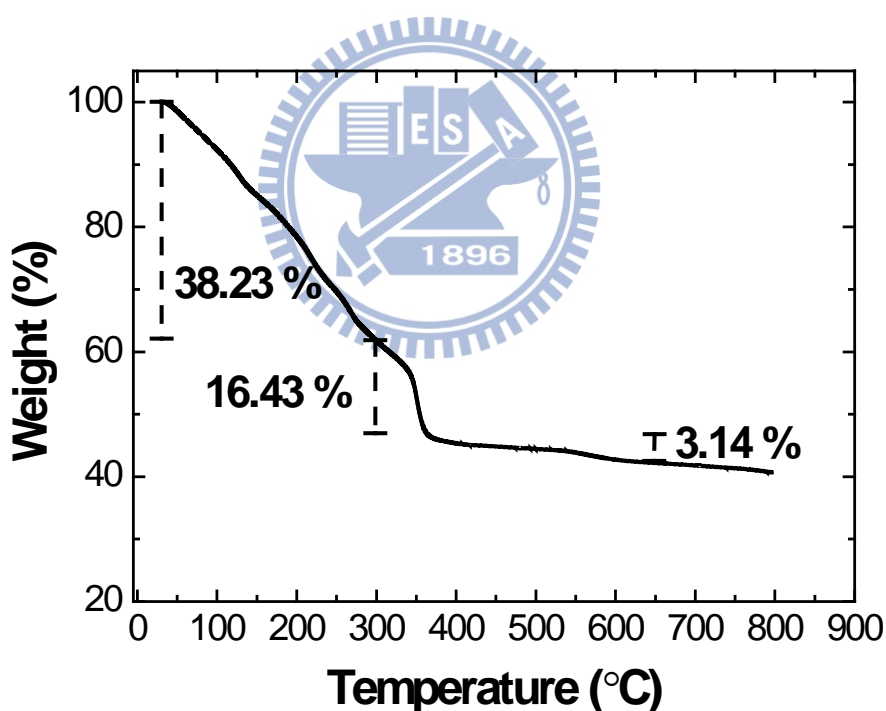


Figure 4.1 A representative TGA profile for the polymeric precursor of $\text{La}_{0.6}\text{Ca}_{0.4}\text{Co}_{0.8}\text{Ru}_{0.2}\text{O}_3$.

Fig. 4.2 presents the XRD profiles for as-synthesized $\text{La}_{0.6}\text{Ca}_{0.4}\text{Co}_{0.8}\text{Ru}_{0.2}\text{O}_3$ and

$\text{La}_{0.6}\text{Ca}_{0.4}\text{CoO}_3$ along with the standard diffraction pattern for $\text{La}_{0.6}\text{Ca}_{0.4}\text{CoO}_3$ (JCPDS no. 35.1389) as a reference. As shown in Fig. 4.2(a), $\text{La}_{0.6}\text{Ca}_{0.4}\text{Co}_{0.8}\text{Ru}_{0.2}\text{O}_3$ revealed a crystalline perovskite phase (ABO_3) with relevant diffraction peaks attributed to those of standard $\text{La}_{0.6}\text{Ca}_{0.4}\text{CoO}_3$. However, there were two minor peaks at $2\theta=30.74^\circ$ and 36.86° , which were identified as La_2O_3 (JCPDS no. 74-1144) and Co_3O_4 (JCPDS no. 78-1969), respectively. From the XRD result of Fig. 4.2(b), a minor phase of Co_3O_4 was also identified in addition to the crystalline $\text{La}_{0.6}\text{Ca}_{0.4}\text{CoO}_3$ phase. We did not observe any diffraction peak from RuO_2 , suggesting that the incorporation of Ru^{3+} at the Co^{3+} sites was achieved successfully. Because Ru^{3+} (0.82 \AA) was relatively larger in size to Co^{3+} (0.69 \AA), the introduction of Ru^{3+} into the perovskite lattice was expected to engender a moderate expansion in lattice parameters, resulting in a slight shift of diffraction peaks to smaller angle side. Indeed, the (024) peak for standard $\text{La}_{0.6}\text{Ca}_{0.4}\text{CoO}_3$ was shifted from 47.56° to 47.02° once $\text{La}_{0.6}\text{Ca}_{0.4}\text{Co}_{0.8}\text{Ru}_{0.2}\text{O}_3$ was formed.

To address the concern over the incomplete synthesis of the $\text{La}_{0.6}\text{Ca}_{0.4}\text{Co}_{0.8}\text{Ru}_{0.2}\text{O}_3$ perovskite, indeed, at 650°C there was a presence of undesirable La_2O_3 and Co_3O_4 , as evidenced by the XRD. However, their residual amount is rather small. In our earlier work of the ACP-derived $\text{La}_{0.6}\text{Ca}_{0.4}\text{Co}_{0.8}\text{Ir}_{0.2}\text{O}_3$ perovskite, at an identical sintering of 650°C for 4 h, we also observed a small amount of La_2O_3 and Co_3O_4 [15]. Hence, we realized that these undesirable oxides are inherent to the ACP process.

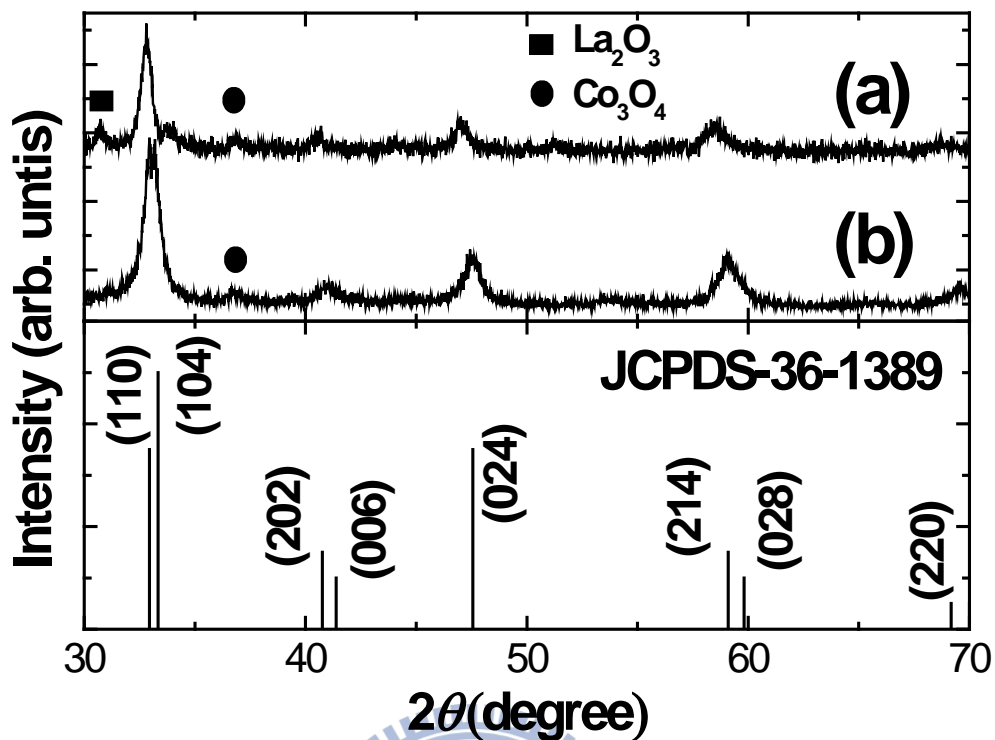


Figure 4.2 XRD for the as-synthesized (a) $\text{La}_{0.6}\text{Ca}_{0.4}\text{Co}_{0.8}\text{Ru}_{0.2}\text{O}_3$ and (b) $\text{La}_{0.6}\text{Ca}_{0.4}\text{CoO}_3$. Also shown is the standard pattern of $\text{La}_{0.6}\text{Ca}_{0.4}\text{CoO}_3$ from JCPDS 35.1389.

Fig. 4.3 provides the SEM images for the $\text{La}_{0.6}\text{Ca}_{0.4}\text{Co}_{0.8}\text{Ru}_{0.2}\text{O}_3$ and $\text{La}_{0.6}\text{Ca}_{0.4}\text{CoO}_3$ powders. As shown in Fig. 4.3(a), $\text{La}_{0.6}\text{Ca}_{0.4}\text{Co}_{0.8}\text{Ru}_{0.2}\text{O}_3$ appeared in a foam-like microstructure with the presence of various micropores in 0.5-3 μm sizes. Unfortunately, individual primary particles were not distinguishable from the image. This foam-like microstructure was typical for the ACP-derived powders experiencing mild sintering treatments as sintering at higher temperatures produced larger particles with significant coalescence, which was not desirable for catalytic ability. The SEM image shown in Fig. 4.3(b) for the ACP-derived $\text{La}_{0.6}\text{Ca}_{0.4}\text{CoO}_3$ also confirmed a porous microstructure with varied pore sizes. Its morphology was rather similar to that of $\text{La}_{0.6}\text{Ca}_{0.4}\text{Co}_{0.8}\text{Ru}_{0.2}\text{O}_3$.

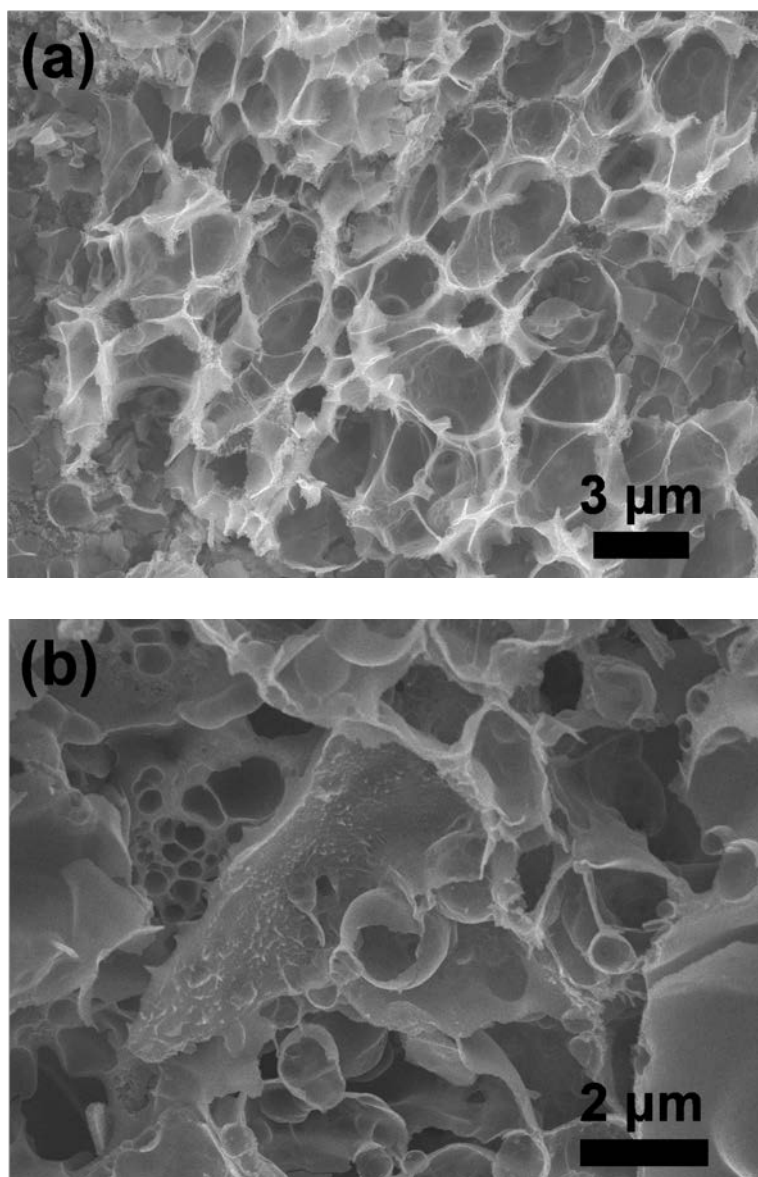


Figure 4.3 SEM images for the as-synthesized (a) $\text{La}_{0.6}\text{Ca}_{0.4}\text{Co}_{0.8}\text{Ru}_{0.2}\text{O}_3$ and (b) $\text{La}_{0.6}\text{Ca}_{0.4}\text{CoO}_3$.

The decomposition of dissolved H_2O_2 in an alkaline electrolyte can be used as the indicator for the ORR. This method is particularly suitable to perovskite, which is known as a two-electron catalyst. When the perovskite powders are suspended in the electrolyte, the decomposition of H_2O_2 proceeds as follows;



As time progresses, the concentration of H_2O_2 is decreased in conjunction with steady oxygen formation. Hence, by measuring the amount of oxygen evolved, we could determine the decomposition rate for H_2O_2 . According to Falcón et al., decomposition of H_2O_2 in the perovskite is presumed to be a first-order reaction in which the reaction rate is proportional to the H_2O_2 concentration [46];

$$-\frac{d[\text{H}_2\text{O}_2]_t}{dt} = k[\text{H}_2\text{O}_2]_t \quad (4-2)$$

where $[\text{H}_2\text{O}_2]_t$ is the H_2O_2 concentration at time t and k is the first-order rate constant. Therefore, after integration on both sides, we could obtain

$$-\frac{d[\text{H}_2\text{O}_2]_t}{[\text{H}_2\text{O}_2]_t} = k dt \quad (4-3)$$

This would lead to a straight line with the k as the slope if we plot the relation of $\ln([\text{H}_2\text{O}_2]_0/[\text{H}_2\text{O}_2]_t)$ as a function of t . $[\text{H}_2\text{O}_2]_t$ can be obtained via the following relation;

$$[\text{H}_2\text{O}_2]_t = [\text{H}_2\text{O}_2]_0 - 2 \times \frac{P_{\text{O}_2} V_{\text{O}_2}}{RTV_{\text{sol}}} \quad (4-4)$$

where $[\text{H}_2\text{O}_2]_0$ is the initial concentration of H_2O_2 when the decomposition begins, $[\text{H}_2\text{O}_2]_t$ is the remaining H_2O_2 concentration at time t , P_{O_2} is 1 atm, T is 298 K, V_{O_2} is the evolved O_2 volume at time t , and V_{sol} is the total volume for the solution.

Fig. 4.4 presents the plots of $\ln([\text{H}_2\text{O}_2]_0/[\text{H}_2\text{O}_2]_t)$ as a function of time for various amounts of $\text{La}_{0.6}\text{Ca}_{0.4}\text{Co}_{0.8}\text{Ru}_{0.2}\text{O}_3$ and $\text{La}_{0.6}\text{Ca}_{0.4}\text{CoO}_3$. As shown in Fig. 4.4(a), an increment in $\text{La}_{0.6}\text{Ca}_{0.4}\text{Co}_{0.8}\text{Ru}_{0.2}\text{O}_3$ loading resulted in a faster decomposition of H_2O_2

which was typical in catalysis. Unexpectedly, the linearity was only observed for samples in the initial stage. In particular, once $\text{La}_{0.6}\text{Ca}_{0.4}\text{Co}_{0.8}\text{Ru}_{0.2}\text{O}_3$ loading was sufficiently large, we recorded an accelerated H_2O_2 decomposition. This suggested that the first-order kinetic assumption was not fully applicable for $\text{La}_{0.6}\text{Ca}_{0.4}\text{Co}_{0.8}\text{Ru}_{0.2}\text{O}_3$. A better linearity was witnessed for $\text{La}_{0.6}\text{Ca}_{0.4}\text{CoO}_3$, as shown in Fig. 4.4(b). The decomposition rate for $\text{La}_{0.6}\text{Ca}_{0.4}\text{CoO}_3$ was consistently lower than that of $\text{La}_{0.6}\text{Ca}_{0.4}\text{Co}_{0.8}\text{Ru}_{0.2}\text{O}_3$ at identical weights as listed in Table 4.1, which infers a high ORR ability for the latter.



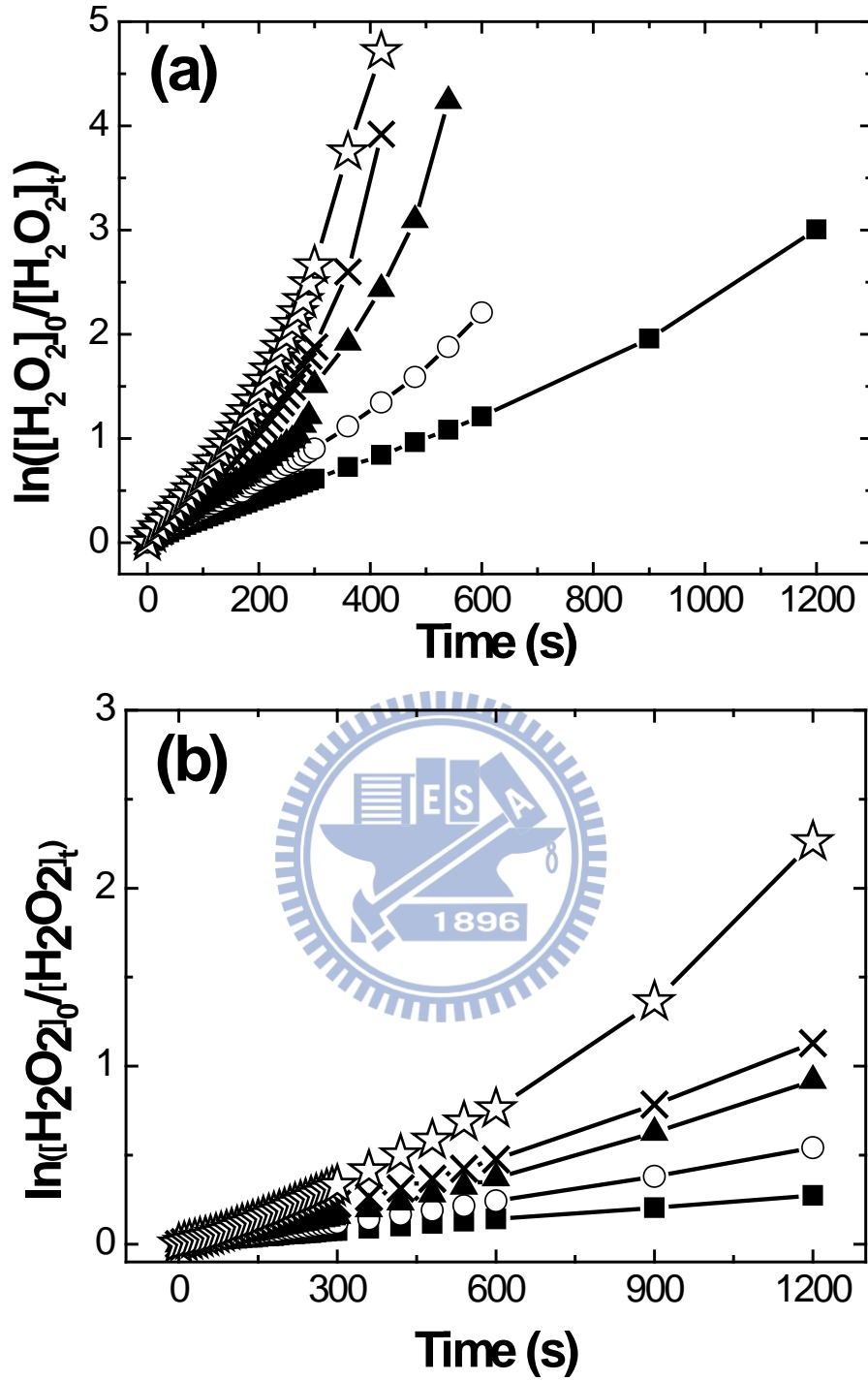


Figure 4.4 Plots of $\ln([H_2O_2]_0/[H_2O_2]_t)$ as a function of time for (a) $La_{0.6}Ca_{0.4}Co_{0.8}Ru_{0.2}O_3$ and (b) $La_{0.6}Ca_{0.4}CoO_3$ at 0.01 (■), 0.015 (○), 0.02 (▲), 0.025 (×), and 0.03 g (☆), respectively.

Table 4.1 The decomposition rate for $\text{La}_{0.6}\text{Ca}_{0.4}\text{Co}_{0.8}\text{Ru}_{0.2}\text{O}_3$ and $\text{La}_{0.6}\text{Ca}_{0.4}\text{CoO}_3$.

| $k \times 10^{-3} \text{ (s}^{-1}\text{)}$ | 10 (mg) | 15 (mg) | 20 (mg) | 25 (mg) | 30 (mg) |
|--|---------|---------|---------|---------|---------|
| $\text{La}_{0.6}\text{Ca}_{0.4}\text{Co}_{0.8}\text{Ru}_{0.2}\text{O}_3$ | 2.29 | 3.37 | 6.35 | 7.33 | 9.84 |
| $\text{La}_{0.6}\text{Ca}_{0.4}\text{CoO}_3$ | 0.205 | 0.301 | 0.405 | 0.505 | 0.591 |

In typical heterogeneous reactions, the actual surface area is critical as it determines the available sites for catalytic actions. Therefore, it would be necessary to obtain the true surface area for both $\text{La}_{0.6}\text{Ca}_{0.4}\text{CoO}_3$ and $\text{La}_{0.6}\text{Ca}_{0.4}\text{Co}_{0.8}\text{Ru}_{0.2}\text{O}_3$ to compare their catalytic abilities. The BET surface area for $\text{La}_{0.6}\text{Ca}_{0.4}\text{CoO}_3$ and $\text{La}_{0.6}\text{Ca}_{0.4}\text{Co}_{0.8}\text{Ru}_{0.2}\text{O}_3$ was 9.2 and 11.6 m^2g^{-1} , respectively. Fig. 4.5 presents the plot of k , which was selected from the linear regime of Fig. 4.4, as a function of actual surface area for both samples. Notably, the k value for the $\text{La}_{0.6}\text{Ca}_{0.4}\text{CoO}_3$ remained relatively unchanged. In contrast, the k value for the $\text{La}_{0.6}\text{Ca}_{0.4}\text{Co}_{0.8}\text{Ru}_{0.2}\text{O}_3$ rose with increasing surface area.

We realized that in our system the decomposition of H_2O_2 might occur in a pseudo-homogeneous first-order reaction as shown in Eq. 3-5 [44]. Hence, during the experiments under constant stirring, it was likely that the microstructure of perovskite powders was altered which exposed to a larger surface area. As a result, we observed accelerated O_2 evolution as a function of time and catalyst loading.

$$-\frac{d[\text{H}_2\text{O}_2]_t}{dt} = k[\text{H}_2\text{O}_2]_t[\text{Catalyst}] \quad (3-5)$$

Actually, the k value for $\text{La}_{0.6}\text{Ca}_{0.4}\text{CoO}_3$ was increased slightly with H_2O_2

decomposition time and catalyst loading. Its value was found to increase from 2.05×10^{-4} to $5.91 \times 10^{-4} \text{ s}^{-1}$. Because both $\text{La}_{0.6}\text{Ca}_{0.4}\text{CoO}_3$ and $\text{La}_{0.6}\text{Ca}_{0.4}\text{Co}_{0.8}\text{Ru}_{0.2}\text{O}_3$ followed the pseudo-homogeneous first-order reaction, they behaved similarly, as shown in Fig. 4.5. Since both the intercept at the infinitesimal surface area and the slope for $\text{La}_{0.6}\text{Ca}_{0.4}\text{Co}_{0.8}\text{Ru}_{0.2}\text{O}_3$ were substantially larger than those of $\text{La}_{0.6}\text{Ca}_{0.4}\text{CoO}_3$, we determined that the former possesses a superior catalytic performance for H_2O_2 decomposition. This would likely lead to a better ORR GDE for $\text{La}_{0.6}\text{Ca}_{0.4}\text{Co}_{0.8}\text{Ru}_{0.2}\text{O}_3$.



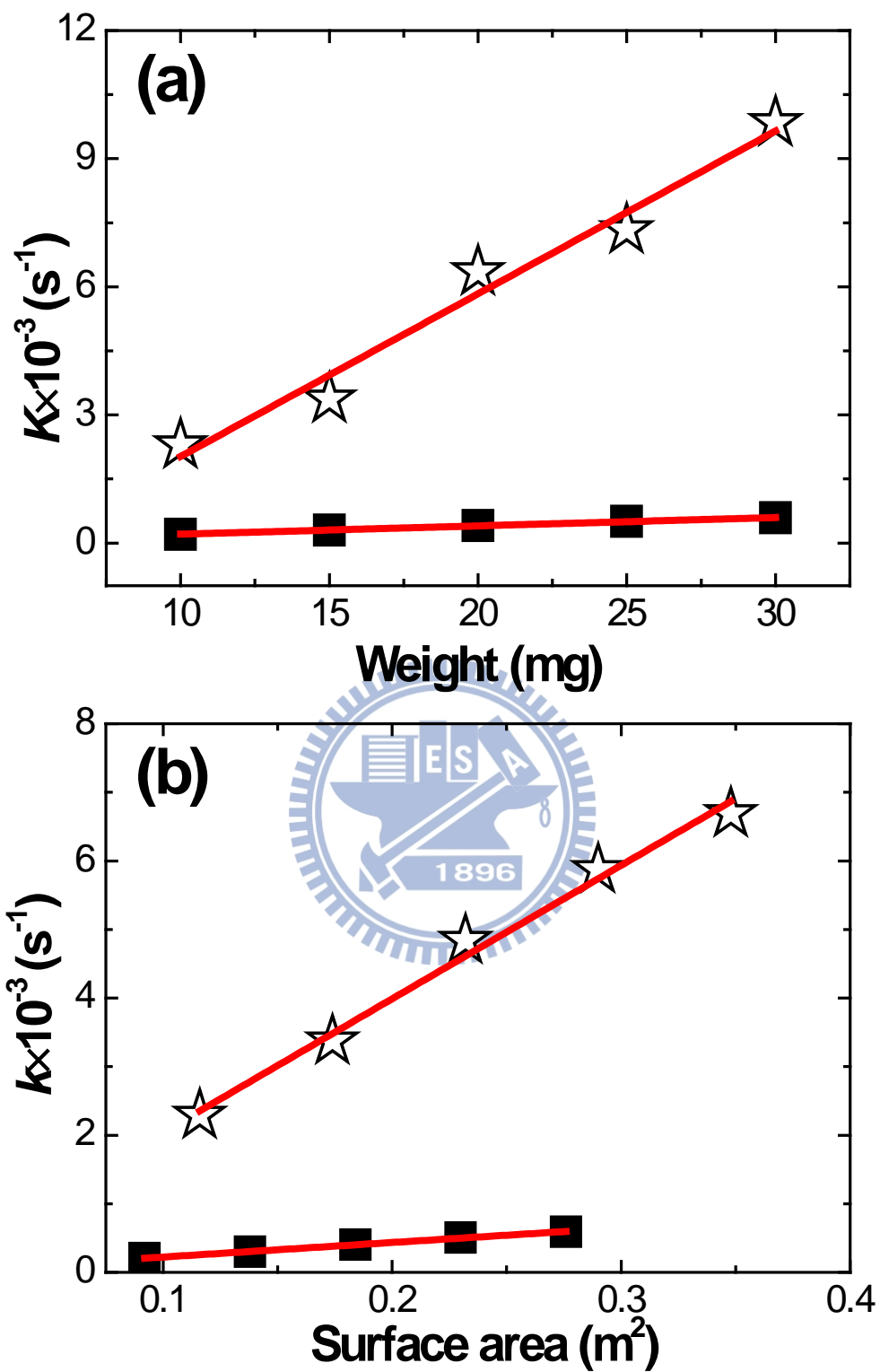


Figure 4.5 Plot of k as a function of actual surface area for $\text{La}_{0.6}\text{Ca}_{0.4}\text{Co}_{0.8}\text{Ru}_{0.2}\text{O}_3$ (☆) and $\text{La}_{0.6}\text{Ca}_{0.4}\text{CoO}_3$ (■).

4.1.2 SSR-derived $\text{La}_{0.6}\text{Ca}_{0.4}\text{Co}_{0.4}\text{Ru}_{0.6}\text{O}_3$

The XRD scans of the SSR-derived $\text{La}_{0.6}\text{Ca}_{0.4}\text{Co}_{1-x}\text{Ru}_x\text{O}_3$ are shown in Fig. 4.6. After sintering at 600°C and 800°C for 4 h, it is observed that the major phase is the desirable $\text{La}_{0.6}\text{Ca}_{0.4}\text{CoO}_3$ perovskite (JCPDS-35.1389). The RuO_2 phase was not present, suggesting successful introduction of Ru^{4+} into Co^{4+} sites. Unfortunately, there is a minor impurity phase of RuO_2 in $\text{La}_{0.6}\text{Ca}_{0.4}\text{RuO}_3$ catalyst. In addition, all XRD peaks shift slightly toward the low angle side (up to $\text{La}_{0.6}\text{Ca}_{0.4}\text{Co}_{0.4}\text{Ru}_{0.6}\text{O}_3$) due to larger Ru^{3+} (0.68 \AA) ions replacing smaller Co^{3+} (0.61 \AA) ions.

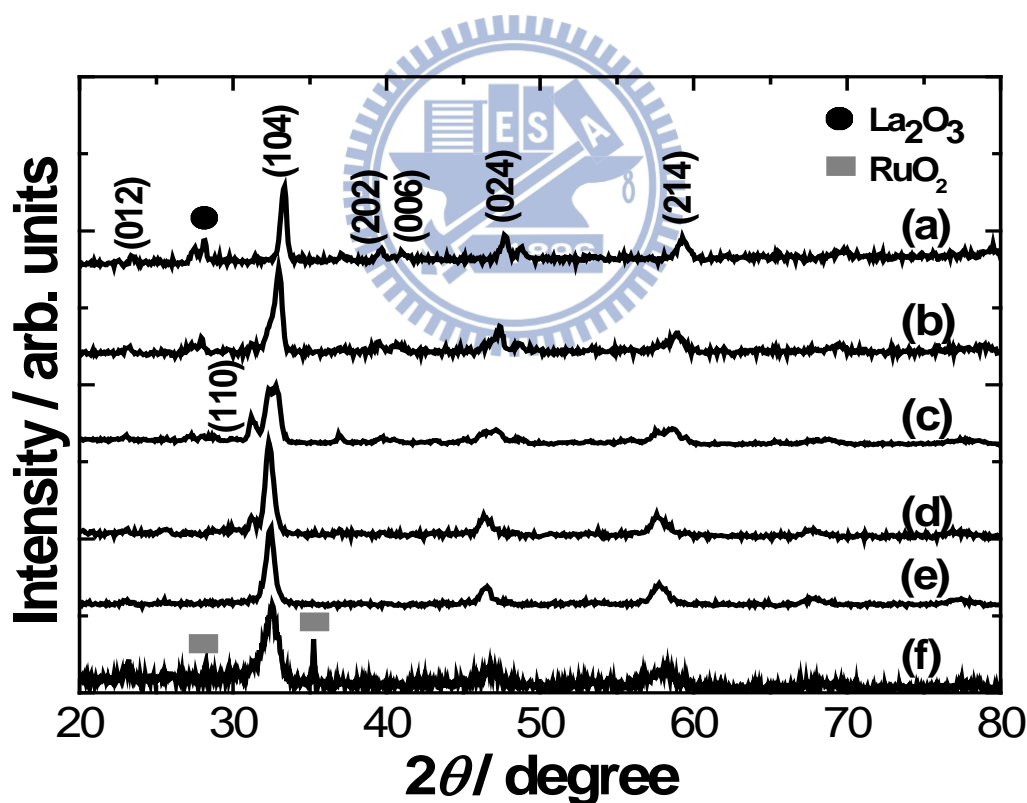


Figure 4.6 The XRD pattern of the $\text{La}_{0.6}\text{Ca}_{0.4}\text{Co}_{1-x}\text{Ru}_x\text{O}_3$ with $x=(a) 0$, (b) 0.2, (c) 0.4, (d) 0.6, (e) 0.8, and (f) 1.

Fig. 4.7 presents the unit cell volume (hexagonal, $V=a^2c \times \sin 60^\circ$) as a function of

stoichiometric rate of Ru, with shows that a linear relationship with the Ru amount (up to $\text{La}_{0.6}\text{Ca}_{0.4}\text{Co}_{0.4}\text{Ru}_{0.6}\text{O}_3$). It can be seen from Table 4.2 that both the lengths a- and c-axes increase from (5.40, 13.18) at $x=0$ to (5.53, 13.71) at $x=0.6$, but it they decline for $x=0.8$ in $\text{La}_{0.6}\text{Ca}_{0.4}\text{Co}_{1-x}\text{Ru}_x\text{O}_3$. It is indicated that the Co^{3+} and Ru^{3+} have the different ionic radii due to the replacement of smaller radius Co^{3+} (0.61 Å) by larger ionic radius Ru^{3+} (0.68 Å). Therefore, the lattice parameters and volume of unit cell were increased as displayed in Table 4.2. On the other hand, a moderate decrease in unit cell volume form $x=0.8$ to 1 due to impurity phase of RuO_2 . Besides, the surface areas of perovskite were displayed in Table 4.2. Note that the surface areas of the perovskite catalysts depend on thermal process. In our case, the $\text{La}_{0.6}\text{Ca}_{0.4}\text{Co}_{1-x}\text{Ru}_x\text{O}_3$ were sintered under same temperature. Hence, the surface areas of $\text{La}_{0.6}\text{Ca}_{0.4}\text{Co}_{1-x}\text{Ru}_x\text{O}_3$ were changed slightly between 7 and 10 m^2g^{-1} as listed in Table 3-2.

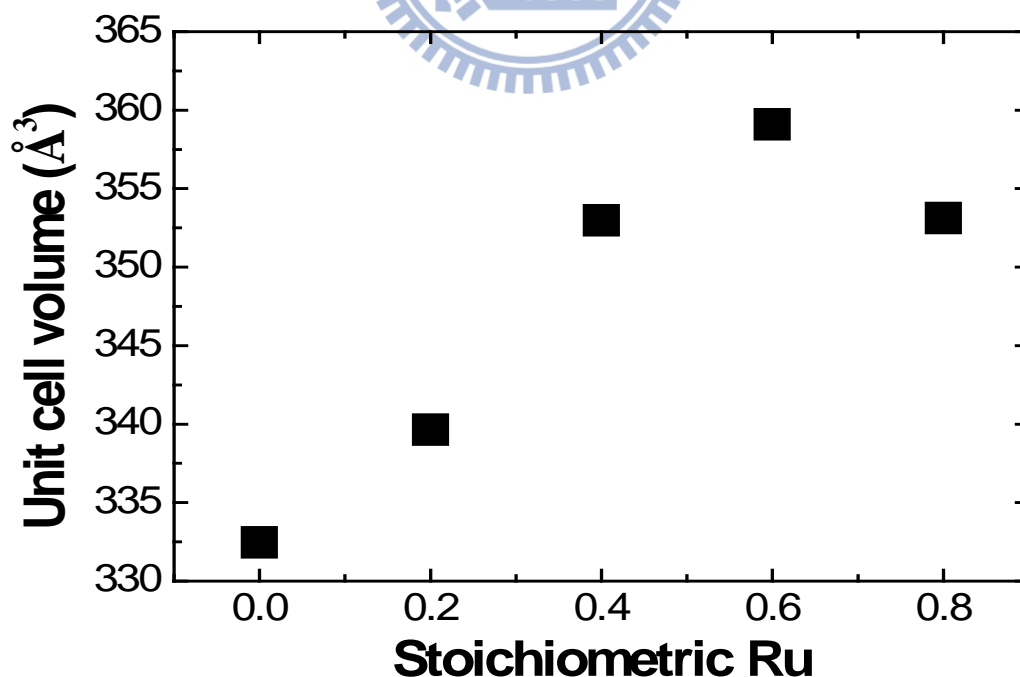


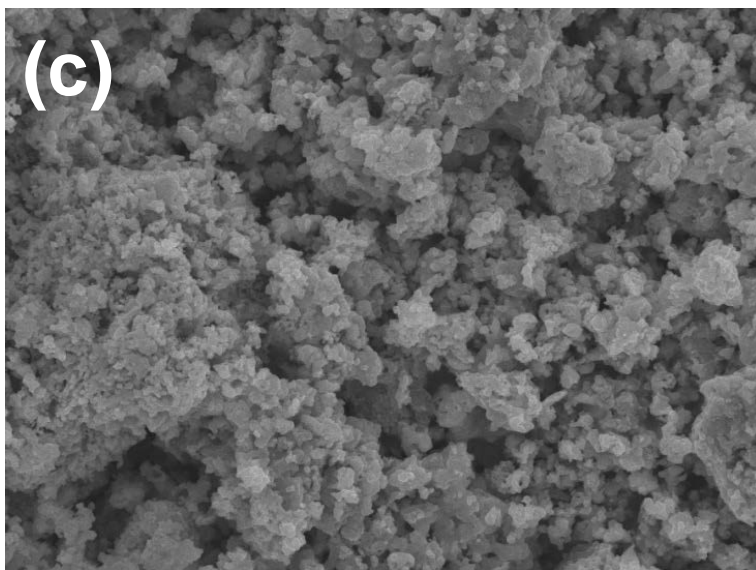
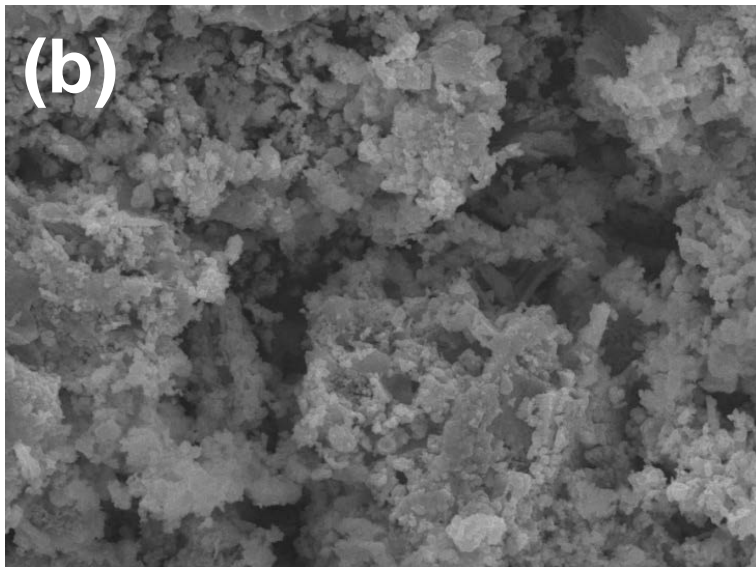
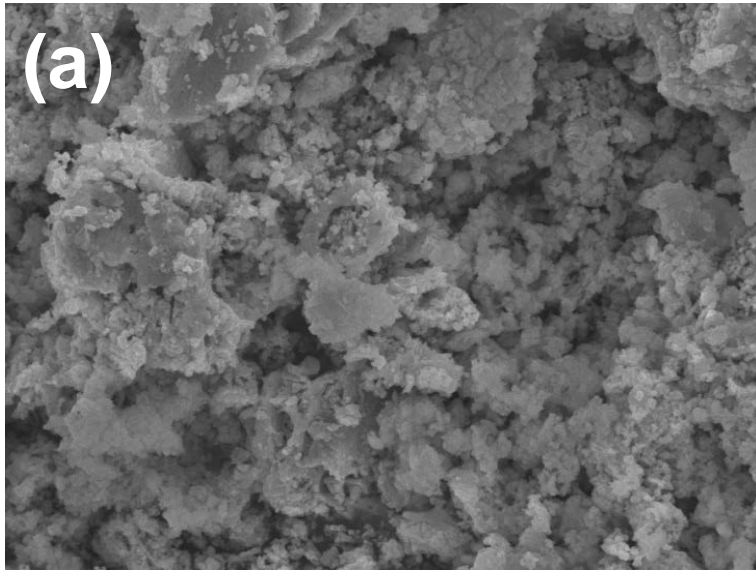
Figure 4.7 The unit cell volume versus the stoichiometric Ru.

Table 4.2 The summary of physical behavior for $\text{La}_{0.6}\text{Ca}_{0.4}\text{Co}_{1-x}\text{Ru}_x\text{O}_3$.

| Sample | Lattice parameter ^a (Å) | | Unit-cell volume (Å ³) | Surface Area (m ² g ⁻¹) |
|---|---------------------------------------|----------|---------------------------------------|--|
| | <i>a</i> | <i>c</i> | <i>V</i> | |
| $\text{La}_{0.6}\text{Ca}_{0.4}\text{CoO}_{3\pm\delta}$ | 5.40 | 13.18 | 332.47 | 9.10 |
| $\text{La}_{0.6}\text{Ca}_{0.4}\text{Co}_{0.8}\text{Ru}_{0.2}\text{O}_{3\pm\delta}$ | 5.43 | 13.30 | 339.64 | 9.61 |
| $\text{La}_{0.6}\text{Ca}_{0.4}\text{Co}_{0.6}\text{Ru}_{0.4}\text{O}_{3\pm\delta}$ | 5.52 | 13.39 | 352.98 | 9.41 |
| $\text{La}_{0.6}\text{Ca}_{0.4}\text{Co}_{0.4}\text{Ru}_{0.6}\text{O}_{3\pm\delta}$ | 5.53 | 13.71 | 359.10 | 7.15 |
| $\text{La}_{0.6}\text{Ca}_{0.4}\text{Co}_{0.2}\text{Ru}_{0.8}\text{O}_{3\pm\delta}$ | 5.50 | 13.48 | 356.13 | 6.99 |

^aThe lattice parameters have been calculated according to hexagonal axes as listed in ICDD Card No. 36-1389.

The SEM morphology of the perovskite catalysts with different Ru ratios are observed in SEM as shown in Fig. 4.8. After the SSR method, the particles seem to consist of agglomerated and non-uniform particle size distribution in all samples. In addition, morphologies synthesized from different methods, ACP and SSR, displayed totally different morphologies. Further, the powders exhibited substantial sintering and those primary particle sizes are around 100 to 300 nm in all samples.



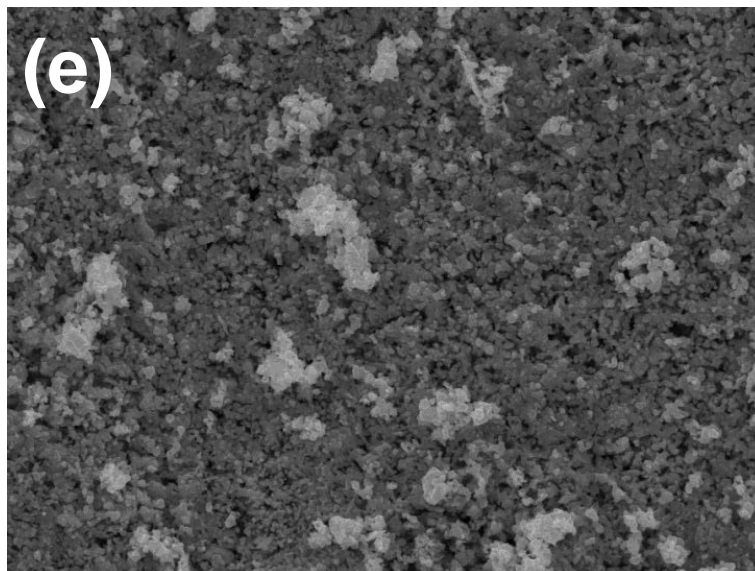
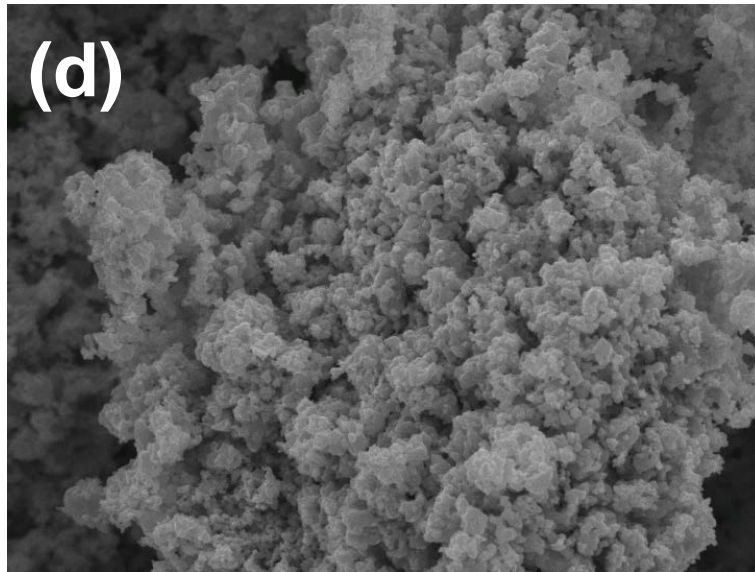
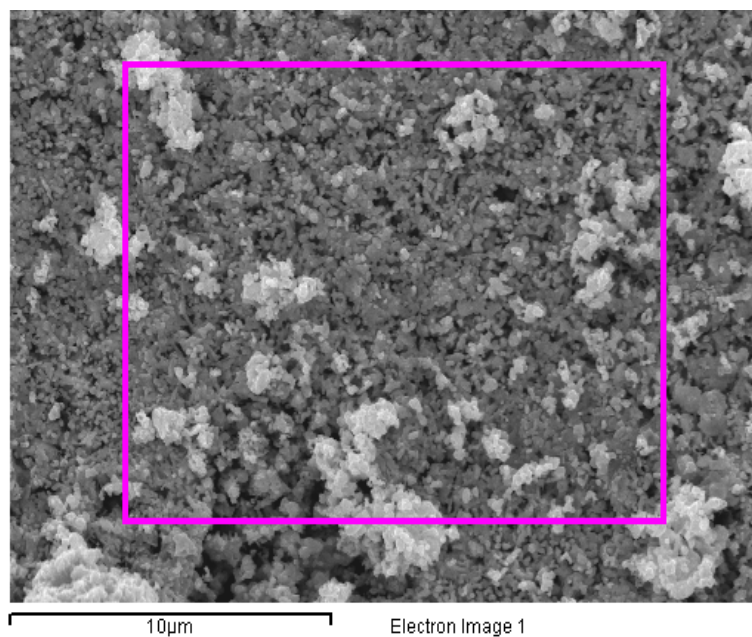


Figure 4.8 SEM images of (a) $\text{La}_{0.6}\text{Ca}_{0.4}\text{CoO}_3$ (b) $\text{La}_{0.6}\text{Ca}_{0.4}\text{Co}_{0.8}\text{Ru}_{0.2}\text{O}_3$ (c) $\text{La}_{0.6}\text{Ca}_{0.4}\text{Co}_{0.6}\text{Ru}_{0.4}\text{O}_3$ (d) $\text{La}_{0.6}\text{Ca}_{0.4}\text{Co}_{0.4}\text{Ru}_{0.6}\text{O}_3$ (e) $\text{La}_{0.6}\text{Ca}_{0.4}\text{Co}_{0.2}\text{Ru}_{0.8}\text{O}_3$. (— scale bar $1\mu\text{m}$)

After the SEM observations, the following Figs. 3.9(a)-(c) show the image, EDX, and EDX mapping of $\text{La}_{0.6}\text{Ca}_{0.4}\text{Co}_{0.2}\text{Ru}_{0.8}\text{O}_3$ while the atomic ratio of $\text{La}_{0.6}\text{Ca}_{0.4}\text{Co}_{1-x}\text{Ru}_x\text{O}_3$ results listed Table 4.3. In addition, the mapping results confirmed that all the cations were evenly distributed in the perovskite phase, which suggested successful incorporation of Ru in general.



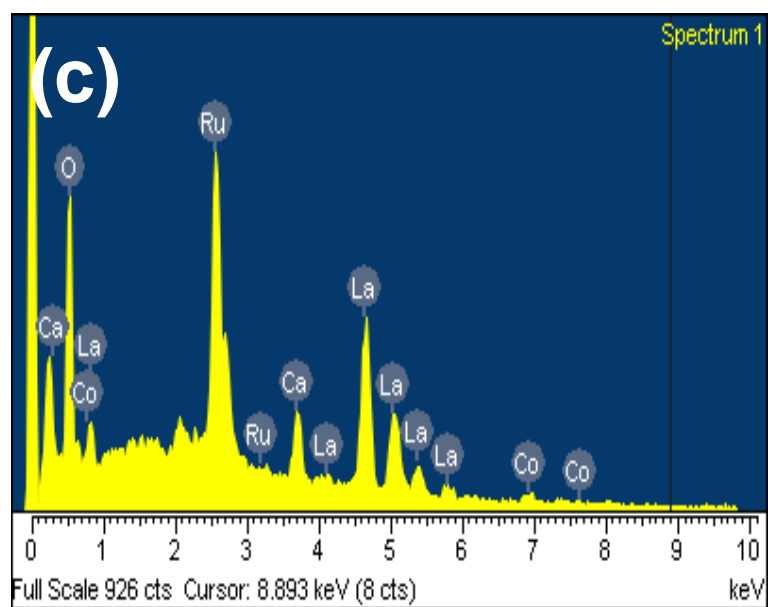
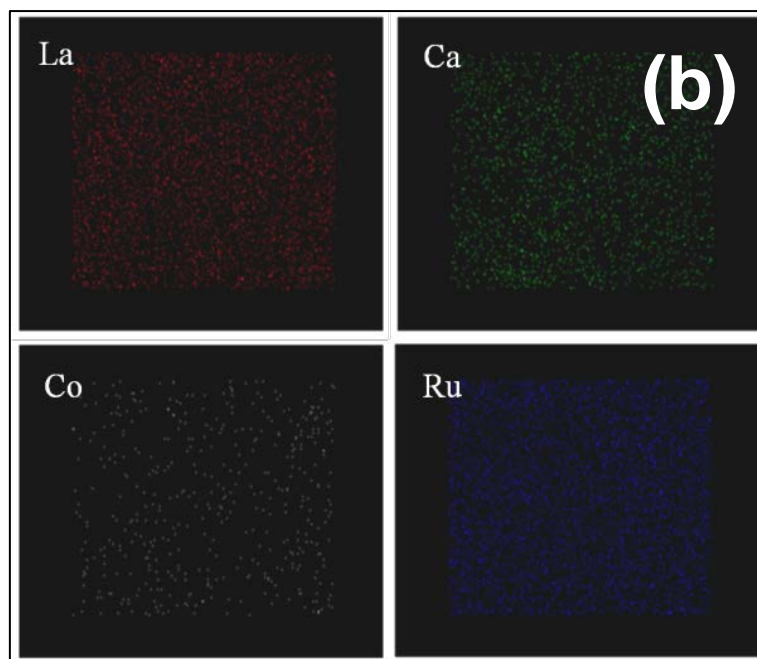


Figure 4.9 SEM of $\text{La}_{0.6}\text{Ca}_{0.4}\text{Co}_{0.2}\text{Ru}_{0.8}\text{O}_3$ in (a) image, (b) mapping, (c) and EDX.

Table 4.3 EDX results of $\text{La}_{0.6}\text{Ca}_{0.4}\text{Co}_{1-x}\text{Ru}_x\text{O}_3$.

| Atomic (%) | La | Ca | Co | Ru | Total |
|---|-------|-------|-------|-------|--------|
| $\text{La}_{0.6}\text{Ca}_{0.4}\text{CoO}_{3\pm\delta}$ | 31.66 | 22.75 | 45.59 | - | 100.00 |
| $\text{La}_{0.6}\text{Ca}_{0.4}\text{Co}_{0.8}\text{Ru}_{0.2}\text{O}_{3\pm\delta}$ | 31.85 | 19.93 | 38.48 | 9.74 | 100.00 |
| $\text{La}_{0.6}\text{Ca}_{0.4}\text{Co}_{0.6}\text{Ru}_{0.4}\text{O}_{3\pm\delta}$ | 32.25 | 17.62 | 28.55 | 21.58 | 100.00 |
| $\text{La}_{0.6}\text{Ca}_{0.4}\text{Co}_{0.4}\text{Ru}_{0.6}\text{O}_{3\pm\delta}$ | 30.95 | 18.30 | 19.54 | 31.21 | 100.00 |
| $\text{La}_{0.6}\text{Ca}_{0.4}\text{Co}_{0.2}\text{Ru}_{0.8}\text{O}_{3\pm\delta}$ | 32.25 | 20.18 | 10.56 | 37.01 | 100.00 |

4.2 Electrochemical characterizations

4.2.1 ACP-derived $\text{La}_{0.6}\text{Ca}_{0.4}\text{Co}_{0.8}\text{Ru}_{0.2}\text{O}_3$

It is known that the type of carbons and their pretreatment methods play critical roles in their performances as catalyst supports. The corresponding mechanism for the carbon-catalyst interaction differs contingent on the type of carbonaceous material and catalyst. In our case, the carbon materials of VXC72R, CNC, and BP2000 were first made into the GDEs to determine their intrinsic electrocatalytic abilities as shown in Fig. 4.10. The $\text{La}_{0.6}\text{Ca}_{0.4}\text{Co}_{0.8}\text{Ru}_{0.2}\text{O}_3$, and carbonaceous materials were mixed together in order to determine their discharging I-V polarization curves. In addition, the BP2000-derived GDE demonstrated a moderately better performance than those derived from the carbon nanocapsules, and Vulcan XC72R. Table 4.4 summarizes some physic behavior of carbonaceous materials.

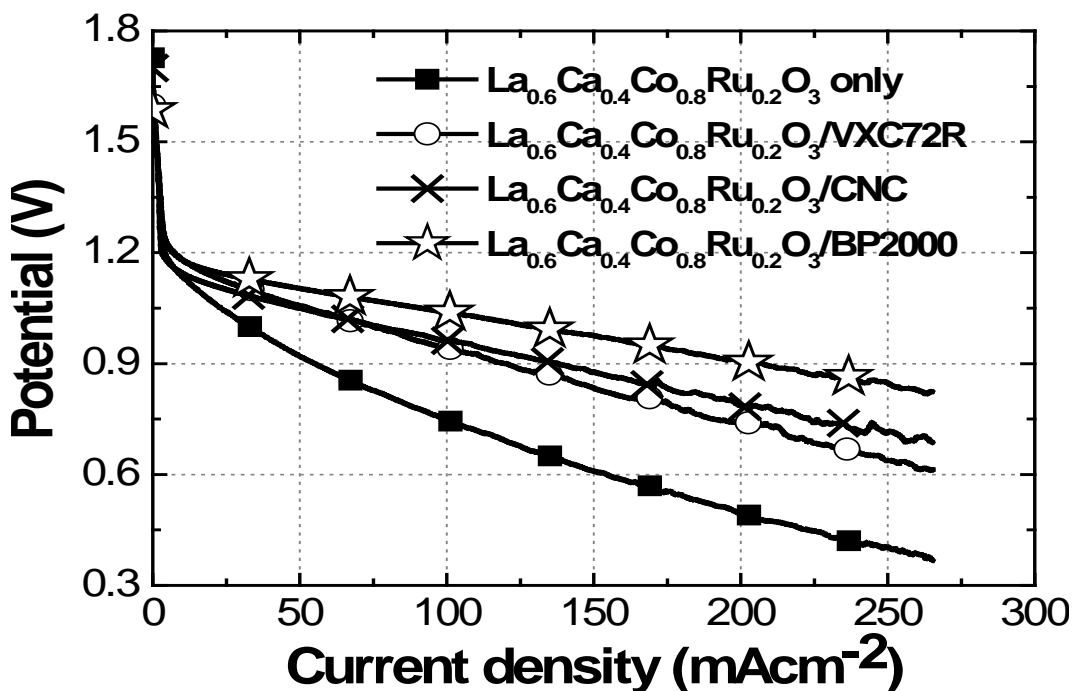


Figure 4.10 The ORR I-V curves for GDEs catalyzed by $\text{La}_{0.6}\text{Ca}_{0.4}\text{Co}_{0.8}\text{Ru}_{0.2}\text{O}_3$ supported on BP2000, VXC72R, and CNCs, respectively.

Table 4.4 Physical properties of carbonaceous materials

| GDLs | Loading (mgcm^{-2}) | Thickness (mm) | Resistivity ($\text{m}\Omega\text{-cm}$) |
|--------|-----------------------------------|-------------------|---|
| XC72R | 1.0 | 0.38 | 54.73 |
| CNCs | 1.0 | 0.38 | 46.52 |
| BP2000 | 1.0 | 0.38 | 35.59 |
| GDE | - | 0.38 | 94.76 |

We selected BP2000 as the catalyst support because it exhibited a desirable surface area suitable for catalyst impregnation. For the ORR the carbon support with the largest available surface area is preferred provided that the catalyst dispersion can be prepared without excessive binders and dispersants [135]. Fig. 4.11 provides the

ORR I-V profiles for the GDEs with electrocatalysts of $\text{La}_{0.6}\text{Ca}_{0.4}\text{Co}_{0.8}\text{Ru}_{0.2}\text{O}_3$, $\text{La}_{0.6}\text{Ca}_{0.4}\text{Co}_{0.8}\text{Ru}_{0.2}\text{O}_3/\text{BP2000}$, and $\text{La}_{0.6}\text{Ca}_{0.4}\text{CoO}_3/\text{BP2000}$. Table 4.5 lists the voltage reading from selective current densities in the ORR I-V curves. These curves exhibited typical I-V characteristics where the potential values were found to decrease gradually from 1.6 V with increasing current densities. Among these samples, $\text{La}_{0.6}\text{Ca}_{0.4}\text{Co}_{0.8}\text{Ru}_{0.2}\text{O}_3/\text{BP2000}$ exhibited the largest catalytic ability, delivering 1.039 and 0.907 V at 100 and 200 mAcm^{-2} , respectively. In contrast, $\text{La}_{0.6}\text{Ca}_{0.4}\text{CoO}_3/\text{BP2000}$ exhibited potentials of 0.983 and 0.648 V at identical current densities. This corresponds to a notable 0.259 V reduction in overpotential at 200 mAcm^{-2} for $\text{La}_{0.6}\text{Ca}_{0.4}\text{Co}_{0.8}\text{Ru}_{0.2}\text{O}_3/\text{BP2000}$. The unsupported $\text{La}_{0.6}\text{Ca}_{0.4}\text{Co}_{0.8}\text{Ru}_{0.2}\text{O}_3$ revealed an accelerated voltage deterioration with increasing current densities. This behavior was not unexpected because earlier literature had confirmed a synergistic effect for perovskite supported on a carbonaceous substrate [24,135].

Table 4.5 Voltages at selective current densities in unit of mAcm^{-2} in the ORR I-V curves for $\text{La}_{0.6}\text{Ca}_{0.4}\text{Co}_{0.8}\text{Ru}_{0.2}\text{O}_3/\text{BP2000}$, $\text{La}_{0.6}\text{Ca}_{0.4}\text{CoO}_3/\text{BP2000}$, and $\text{La}_{0.6}\text{Ca}_{0.4}\text{Co}_{0.8}\text{Ru}_{0.2}\text{O}_3$.

| | 50 | 100 | 150 | 200 |
|--|-------|-------|-------|-------|
| $\text{La}_{0.6}\text{Ca}_{0.4}\text{Co}_{0.8}\text{Ru}_{0.2}\text{O}_3/\text{BP2000}$ | 1.103 | 1.039 | 0.985 | 0.907 |
| $\text{La}_{0.6}\text{Ca}_{0.4}\text{CoO}_3/\text{BP2000}$ | 1.134 | 0.983 | 0.822 | 0.648 |
| $\text{La}_{0.6}\text{Ca}_{0.4}\text{Co}_{0.8}\text{Ru}_{0.2}\text{O}_3$ | 0.920 | 0.746 | 0.608 | 0.490 |

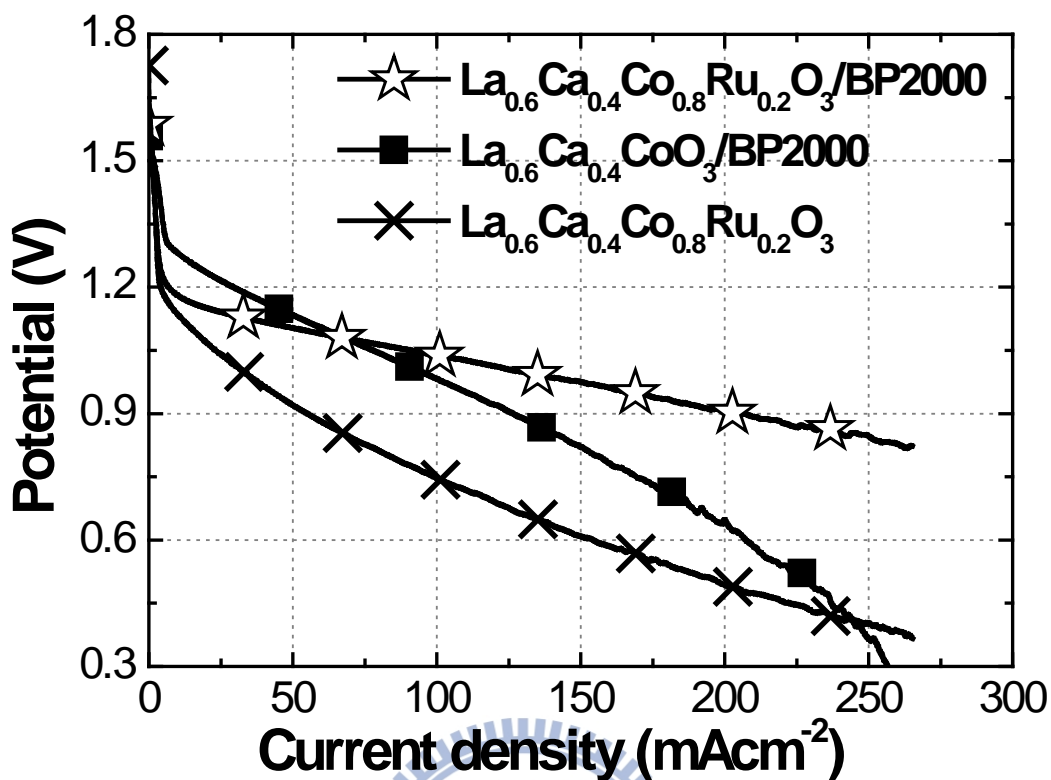


Figure 4.11 ORR I-V polarization curves for $\text{La}_{0.6}\text{Ca}_{0.4}\text{Co}_{0.8}\text{Ru}_{0.2}\text{O}_3/\text{BP2000}$ (\star), $\text{La}_{0.6}\text{Ca}_{0.4}\text{CoO}_3/\text{BP2000}$ (\blacksquare), and $\text{La}_{0.6}\text{Ca}_{0.4}\text{Co}_{0.8}\text{Ru}_{0.2}\text{O}_3$ (\times), respectively.

As shown in the Fig. 4.2(b), for the ACP-derived $\text{La}_{0.6}\text{Ca}_{0.4}\text{CoO}_3$ powders, there appears a minor phase of Co_3O_4 . In contrast, both Co_3O_4 and La_2O_3 are present for the $\text{La}_{0.6}\text{Ca}_{0.4}\text{Co}_{0.8}\text{Ru}_{0.2}\text{O}_3$ powders. To verify the ORR catalytic ability for Co_3O_4 and La_2O_3 , we purchased both chemicals (La_2O_3 : Aldrich, 99.9 wt % and Co_3O_4 : Showa, 99.5 wt % Co_3O_4 + 5 wt % CoO) and fabricated the GDEs with identical catalyst loadings. The resulting ORR I-V curves are shown in Fig. 4.12. As shown, both Co_3O_4 and La_2O_3 revealed moderate catalytic abilities and their performances are considerably reduced. Apparently, there are marginal improvements as opposed to that of noncatalyzed GDE. According to Neburchilov *et al.*, the ORR catalytic ability for La_2O_3 is limited because of its poor electrical conductivity [18]. Furthermore, Co_3O_4 is unstable during the ORR in alkaline electrolyte although it reveals a moderate

ability. Therefore, we concluded that the minute phases of Co_3O_4 and La_2O_3 in $\text{La}_{0.6}\text{Ca}_{0.4}\text{Co}_{0.8}\text{Ru}_{0.2}\text{O}_3$ are not likely to contribute significantly to the ORR action.

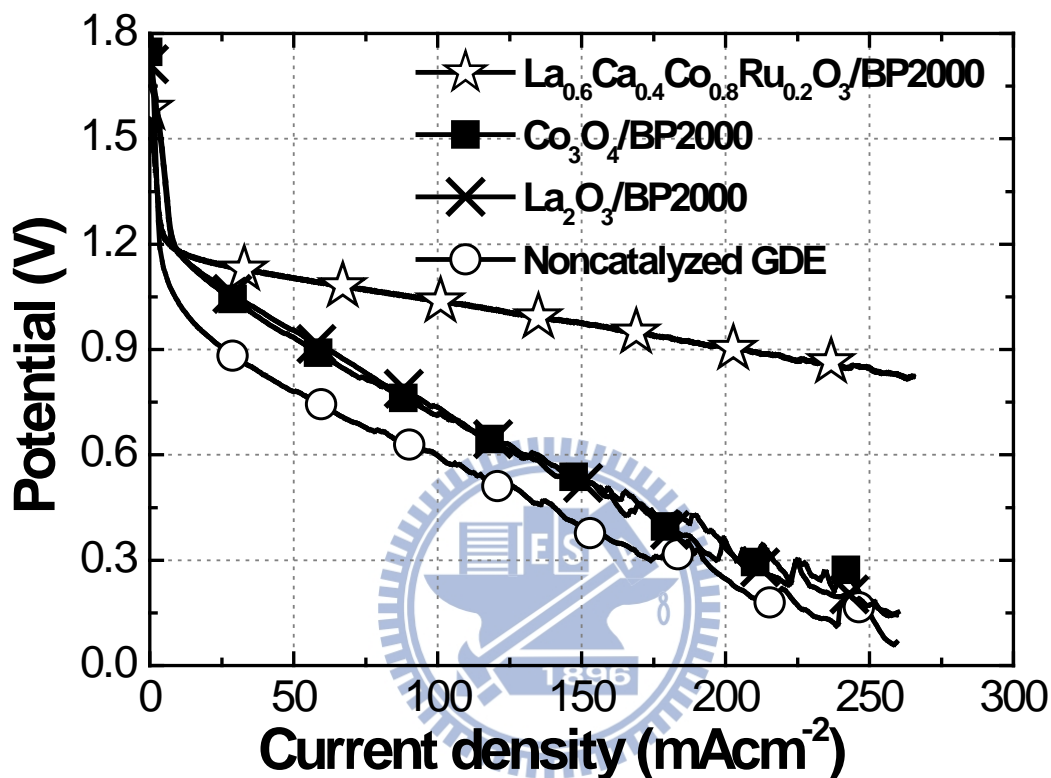
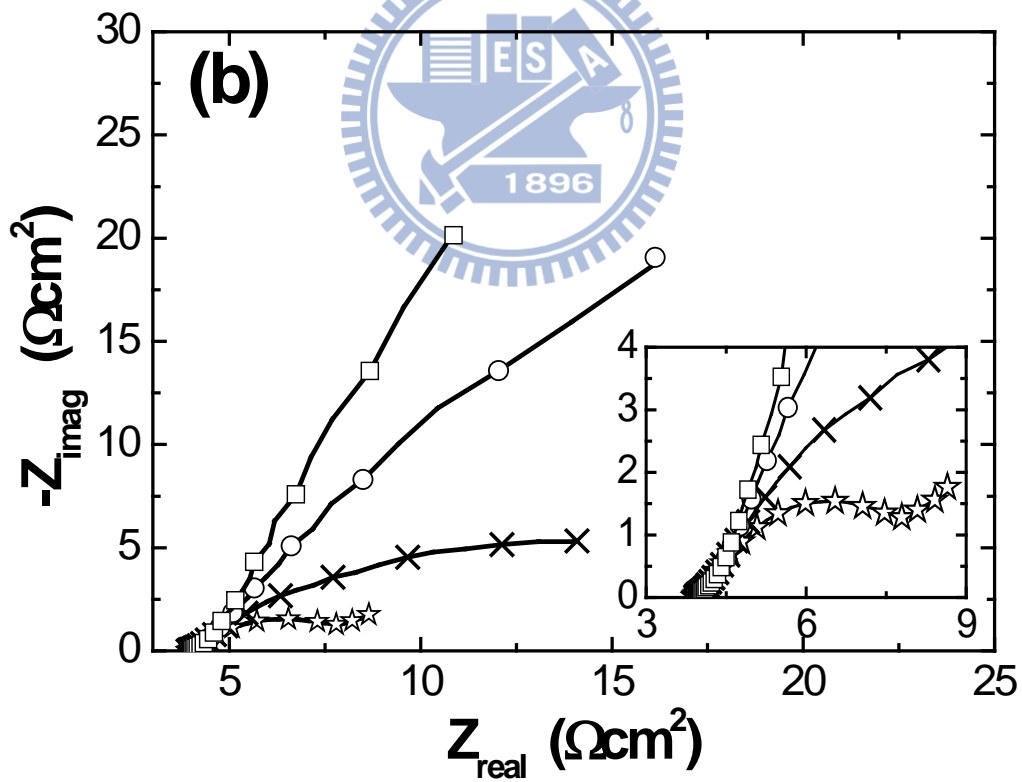
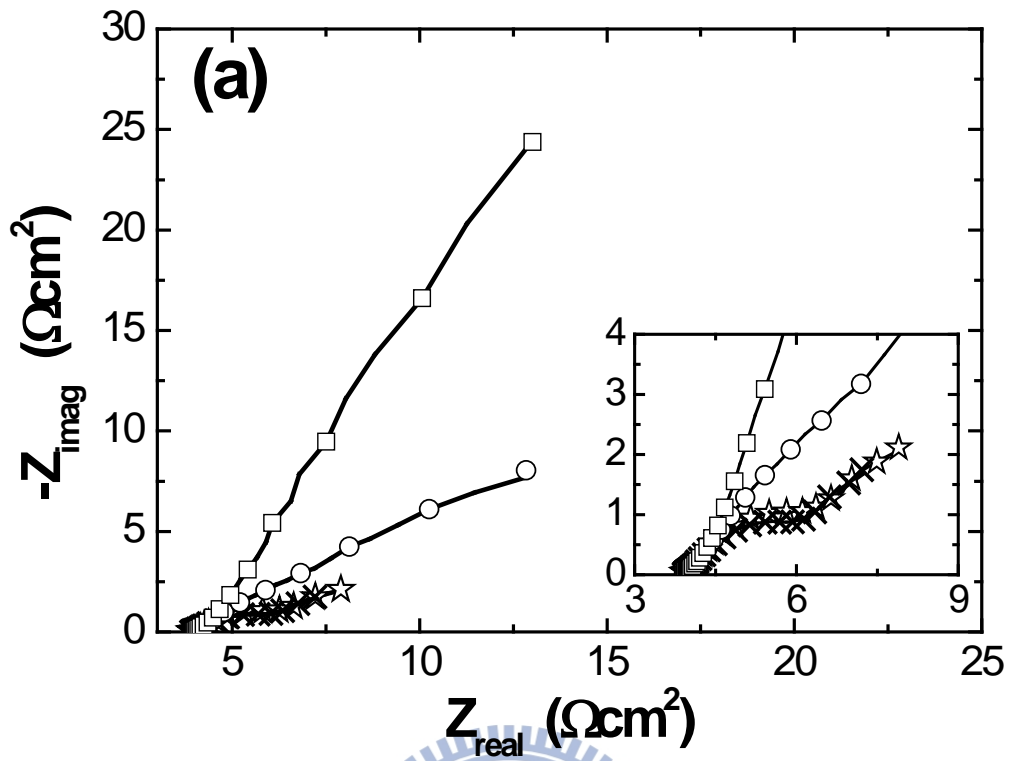


Figure 4.12 The ORR I-V curves for the GDEs catalyzed by $\text{La}_{0.6}\text{Ca}_{0.4}\text{Co}_{0.8}\text{Ru}_{0.2}\text{O}_3/\text{BP2000}$, $\text{Co}_3\text{O}_4/\text{BP2000}$, and $\text{La}_2\text{O}_3/\text{BP2000}$, respectively. Also shown is the noncatalyzed GDE for comparison purpose.

The impedance measurements were carried out on $\text{La}_{0.6}\text{Ca}_{0.4}\text{Co}_{0.8}\text{Ru}_{0.2}\text{O}_3/\text{BP2000}$ and $\text{La}_{0.6}\text{Ca}_{0.4}\text{CoO}_3/\text{BP2000}$ to estimate the charge-transfer resistance (R_{CT}) directly without interference from the electrolyte IR loss. Fig. 4.13 presents their impedance spectra in Nyquist plots at the open-circuit voltage as well as under polarizations of -100 , -200 , and -300 mV. As shown in Fig. 4.13(a), $\text{La}_{0.6}\text{Ca}_{0.4}\text{Co}_{0.8}\text{Ru}_{0.2}\text{O}_3/\text{BP2000}$ exhibited a large Warburg impedance at the

open-circuit voltage, which was attributed to the double-layer capacitance of the cell. Under cathodic polarizations, the impedance was reduced steadily with an increasing overpotential in conjunction with a distinct semi-circle at the high frequency regime. This behavior is clearly shown in the inset of Fig. 4.13(a). It is understood that the intercept for the semi-circle at the highest frequency represented the electrolyte resistance and its diameter indicated the value for R_{CT} . Apparently, the R_{CT} became smaller at larger overpotentials. This behavior was consistent with the electrode reactions reported previously [136-138]. Identical behaviors were observed for $\text{La}_{0.6}\text{Ca}_{0.4}\text{CoO}_3/\text{BP2000}$, as shown in Fig. 4.13(b). At the open-circuit voltage, we recorded a large Warburg impedance whose value was close to that of $\text{La}_{0.6}\text{Ca}_{0.4}\text{Co}_{0.8}\text{Ru}_{0.2}\text{O}_3/\text{BP2000}$. This was likely because both $\text{La}_{0.6}\text{Ca}_{0.4}\text{Co}_{0.8}\text{Ru}_{0.2}\text{O}_3$ and $\text{La}_{0.6}\text{Ca}_{0.4}\text{CoO}_3$ probably due to similar specific surface area. Once the cathodic overpotential was imposed, the impedance spectra moved downward and the formation of semi-circle became apparent. An electrode with a smaller R_{CT} is recognized for a facile faradaic reaction. Therefore, the equivalent circuit model for the fitting the impedance spectra is provided in Fig. 4.13(c). From these spectra, the R_{CT} for both $\text{La}_{0.6}\text{Ca}_{0.4}\text{Co}_{0.8}\text{Ru}_{0.2}\text{O}_3/\text{BP2000}$ and $\text{La}_{0.6}\text{Ca}_{0.4}\text{CoO}_3/\text{BP2000}$ at -300 mV were 4.556 and $5.429 \text{ } \Omega\text{cm}^2$, respectively. This confirmed the better catalytic ability for the ORR of $\text{La}_{0.6}\text{Ca}_{0.4}\text{Co}_{0.8}\text{Ru}_{0.2}\text{O}_3/\text{BP2000}$.



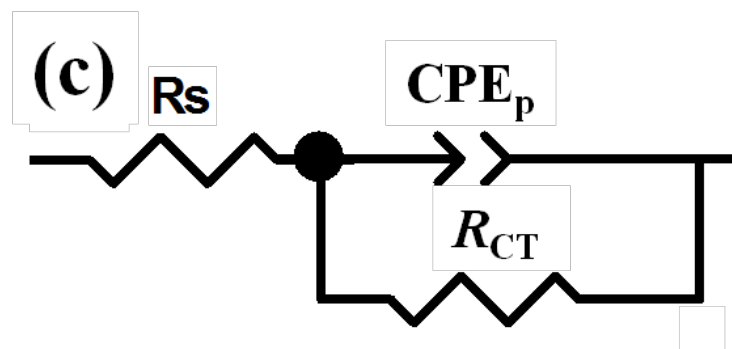


Figure 4.13 Impedance spectra for the (a) $\text{La}_{0.6}\text{Ca}_{0.4}\text{Co}_{0.8}\text{Ru}_{0.2}\text{O}_3/\text{BP2000}$ and (b) $\text{La}_{0.6}\text{Ca}_{0.4}\text{CoO}_3/\text{BP2000}$ at open-circuit voltage (\square), and overpotentials of -100 mV (\circ), -200 mV (\times), and -300 mV (\star), respectively. (c) is the equivalent circuit model used to fit the impedance spectra.

To verify the sustainable catalytic abilities for the ORR, we carried out galvanostatic measurements for $\text{La}_{0.6}\text{Ca}_{0.4}\text{Co}_{0.8}\text{Ru}_{0.2}\text{O}_3/\text{BP2000}$ at selective current densities of 10, 50, 100, and 150 mAcm^{-2} . Fig. 4.14 presents the resulting voltage profiles for 10 min. As shown, the voltage plateaus for most of the samples were relatively flat and their values were consistent with those reported in our earlier I-V polarization curves. At 150 mAcm^{-2} , there was a slight fluctuation on the voltage response in conjunction with a slow decline, which was likely caused by a limitation on the O_2 supply. Despite of this moderate performance degradation at 150 mAcm^{-2} , catalytic behavior for $\text{La}_{0.6}\text{Ca}_{0.4}\text{Co}_{0.8}\text{Ru}_{0.2}\text{O}_3/\text{BP2000}$ was rather stable and sustainable provided that the current density was maintained below 100 mAcm^{-2} .

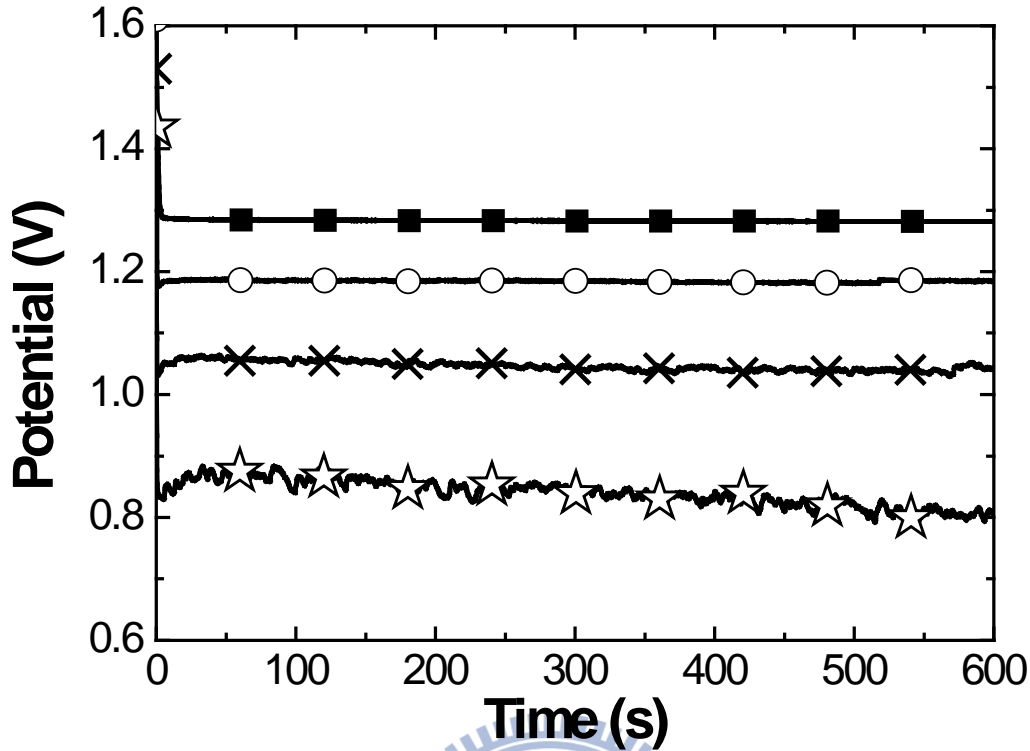


Figure 4.14 Galvanostatic ORR profiles for $\text{La}_{0.6}\text{Ca}_{0.4}\text{Co}_{0.8}\text{Ru}_{0.2}\text{O}_3/\text{BP2000}$ at current densities of 10 (■), 50 (○), 100 (×), and 200 (☆) mAcm^{-2} .

The life time performance for $\text{La}_{0.6}\text{Ca}_{0.4}\text{Co}_{0.8}\text{Ru}_{0.2}\text{O}_3/\text{BP2000}$ was evaluated at 4.8 mgcm^{-2} loading (considering the weight of $\text{La}_{0.6}\text{Ca}_{0.4}\text{Co}_{0.8}\text{Ru}_{0.2}\text{O}_3$ only) for a current density of 10 mAcm^{-2} . The resulting voltage profile is presented in Fig. 4.15 in which the voltage curve experienced a gradual decline from 1.233 V at a slope of 0.063 mVh^{-1} . At the 2000th h, $\text{La}_{0.6}\text{Ca}_{0.4}\text{Co}_{0.8}\text{Ru}_{0.2}\text{O}_3/\text{BP2000}$ still maintained a respectable 1.108 V. Because the life time experiment was conducted with unfiltered ambient air, the residual CO_2 engendered carbonation in the KOH electrolyte that not only affected the electrolyte conductivity but also altered the GDE microstructure. As a result, the voltage response expectedly decreased with the prolonged CO_2 exposure. At the 2622th h, we observed a sudden drop in voltage, which was believed to be due to the last stage of electrolyte flooding that inundated the catalytic surface entirely.

This was likely because in our GDE, $\text{La}_{0.6}\text{Ca}_{0.4}\text{Co}_{0.8}\text{Ru}_{0.2}\text{O}_3/\text{BP2000}$ was brush-painted on its surface as a thin layer.

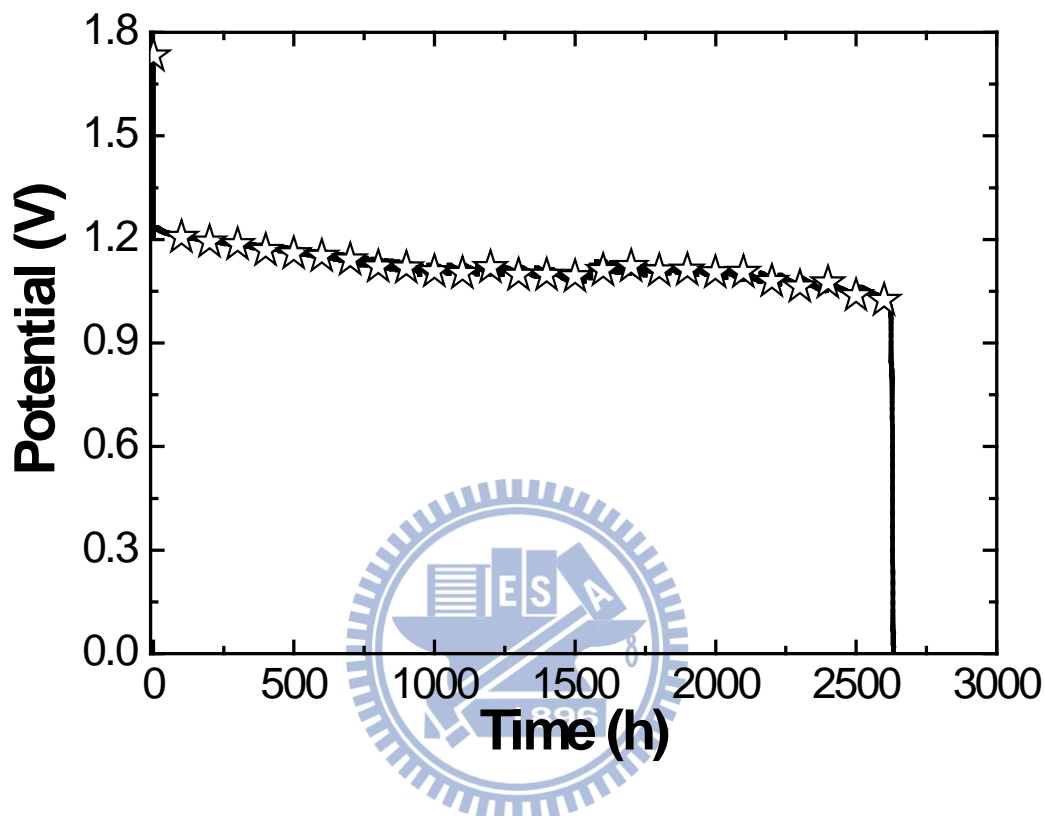


Figure 4.15 Life time performance for $\text{La}_{0.6}\text{Ca}_{0.4}\text{Co}_{0.8}\text{Ru}_{0.2}\text{O}_3/\text{BP2000}$ (☆) at current density of 10 mAcm^{-2} .

4.2.2 SSR-derived $\text{La}_{0.6}\text{Ca}_{0.4}\text{Co}_{0.4}\text{Ru}_{0.6}\text{O}_3$

Fig. 4.16 shows the discharging I-V polarization curves of perovskite catalysts containing different amount of supported Ru on BP2000. It is worth mentioned that the perovskite catalysts exhibit much improvement for the doped one over the non-doped one. In addition, the composition of $\text{La}_{0.6}\text{Ca}_{0.4}\text{Co}_{0.4}\text{Ru}_{0.6}\text{O}_3/\text{BP2000}$ GDE possesses the best catalytic ability.

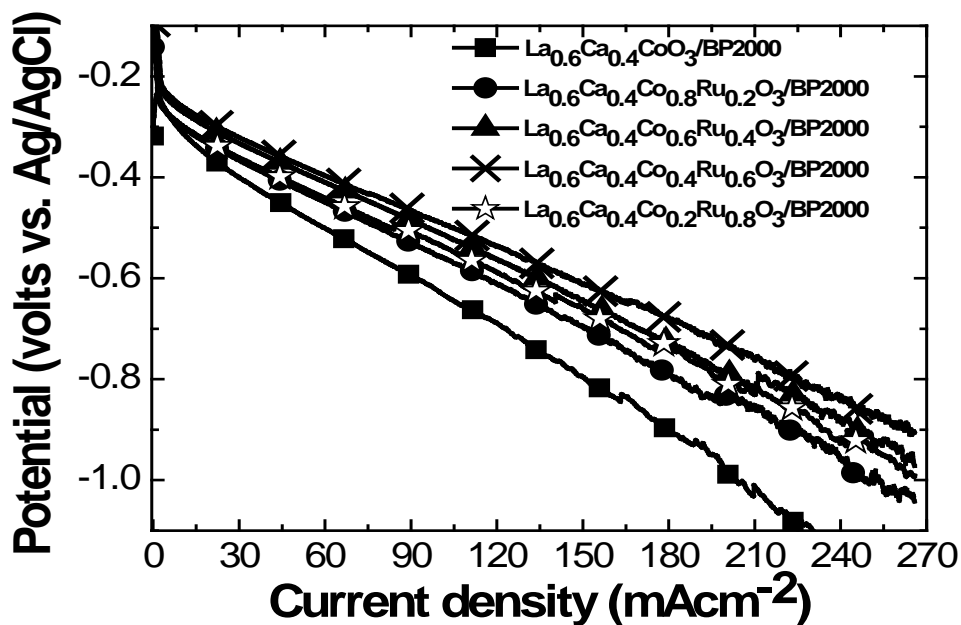
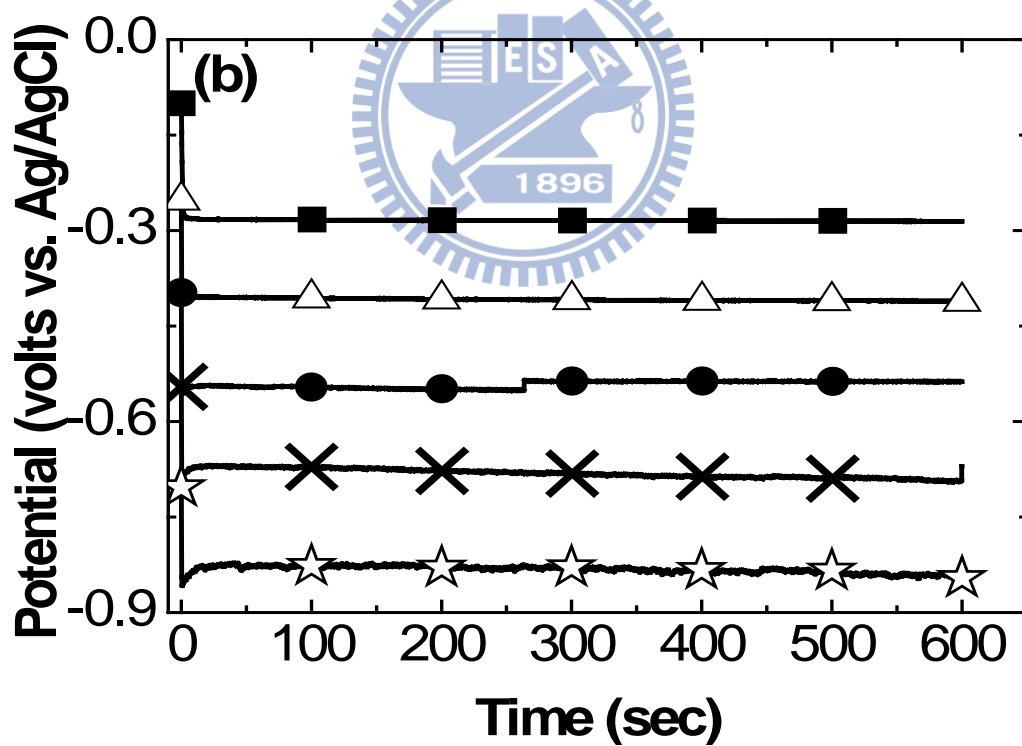
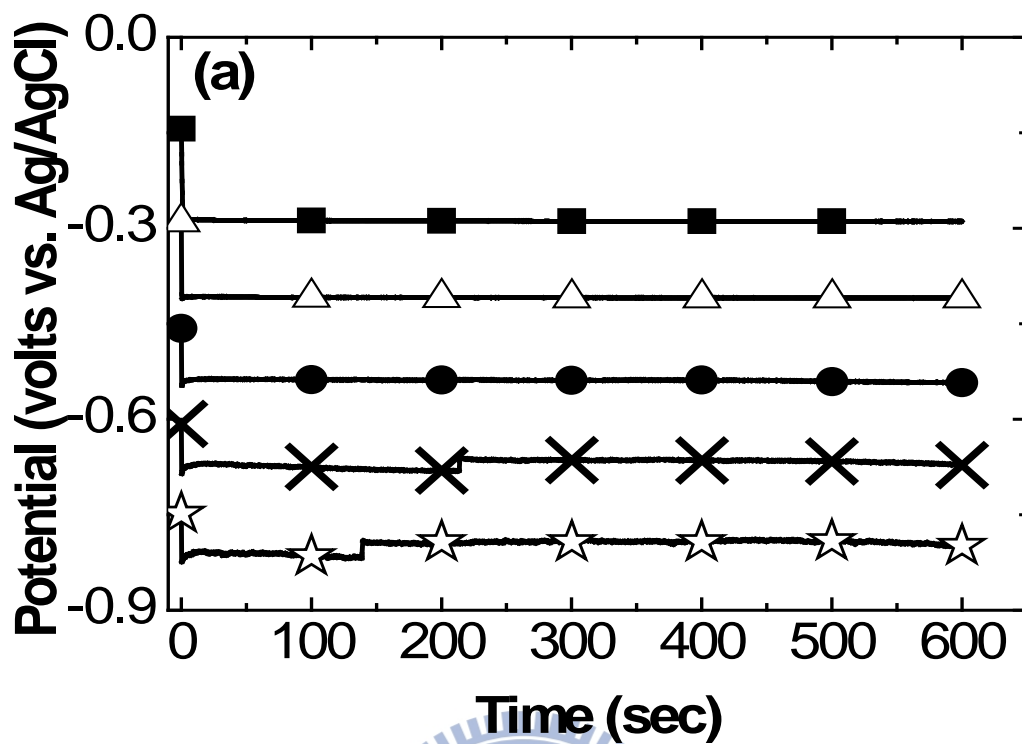


Figure 4.16 The discharging I-V polarization curves of $\text{La}_{0.6}\text{Ca}_{0.4}\text{Co}_{1-x}\text{Ru}_x\text{O}_3/\text{BP2000}$.

Furthermore, the galvanostatic discharge curves for 10 min from current density of 10 mAcm^{-2} to 200 mAcm^{-2} are shown in Figs. 3.17(a)-(c). As clearly presented, the discharges curves are rather flat. In addition, the voltage readings are consistent with those recorded earlier in the discharging I-V polarization curves (Fig. 4.16).



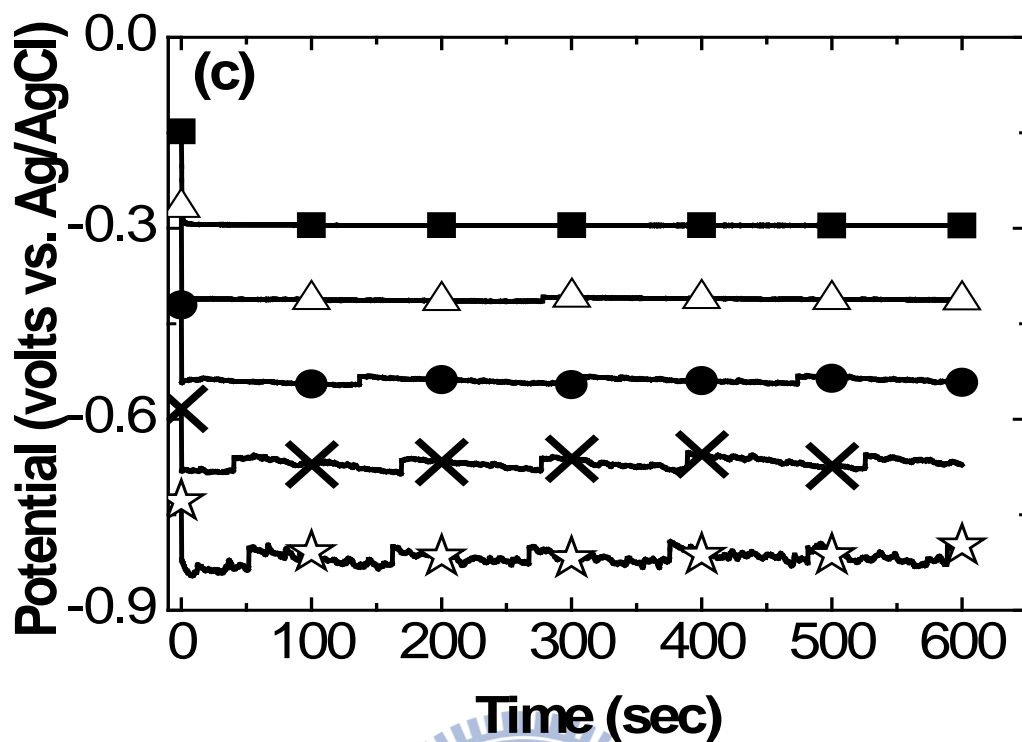


Figure 4.17 The galvanostatic discharge curves for the (a) $\text{La}_{0.6}\text{Ca}_{0.4}\text{Co}_{0.8}\text{Ru}_{0.2}\text{O}_3/\text{BP2000}$ (b) $\text{La}_{0.6}\text{Ca}_{0.4}\text{Co}_{0.6}\text{Ru}_{0.4}\text{O}_3/\text{BP2000}$ (c) $\text{La}_{0.6}\text{Ca}_{0.4}\text{Co}_{0.2}\text{Ru}_{0.8}\text{O}_3/\text{BP2000}$ at current densities of 10 mAcm^{-2} (■), 50 mAcm^{-2} (△), 100 mAcm^{-2} (●), 150 mAcm^{-2} (×), and 200 mAcm^{-2} (☆).

Further comparisons with known electrocatalysts are illustrated in Fig. 4.18. The $\text{La}_{0.6}\text{Ca}_{0.4}\text{Co}_{0.4}\text{Ru}_{0.6}\text{O}_3/\text{BP2000}$ GDE shows comparable performance with commercial product of EVT-Mn, EVT-MnCo, and home-made Ag/CNC. Indeed, $\text{La}_{0.6}\text{Ca}_{0.4}\text{Co}_{0.4}\text{Ru}_{0.6}\text{O}_3/\text{BP2000}$ GDE possesses the best electrochemical performance.

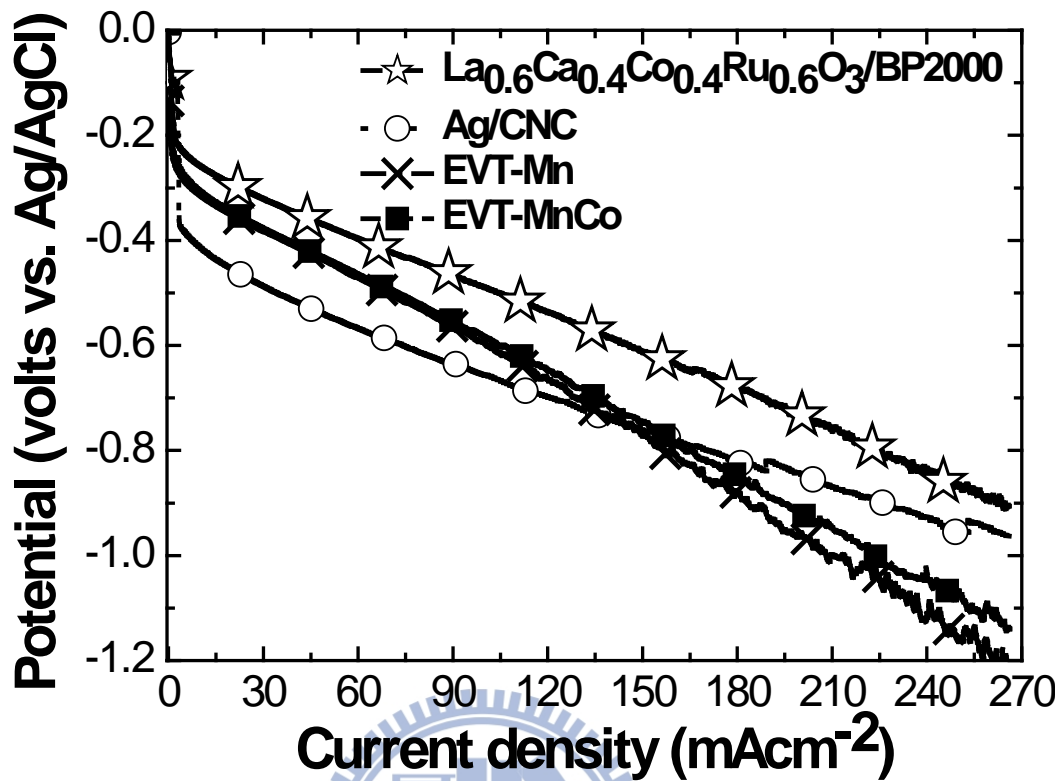


Figure 4.18 The I-V polarization curves of the La_{0.6}Ca_{0.4}Co_{0.4}Ru_{0.6}O₃/BP2000 GDE and the catalyzed GDEs with electrocatalysts of Ag/CNC, commercial EVT-Mn, and commercial EVT-MnCo.

Fig. 4.19 shows the charging I-V polarization curves of perovskite catalyses containing various Ru contents. As shown in the figure, the perovskites with Ru doping exhibit consistent performance enhancements over that of undoped one. Furthermore, once the Ru content was increased, further improvement in the electrochemical performance was observed.

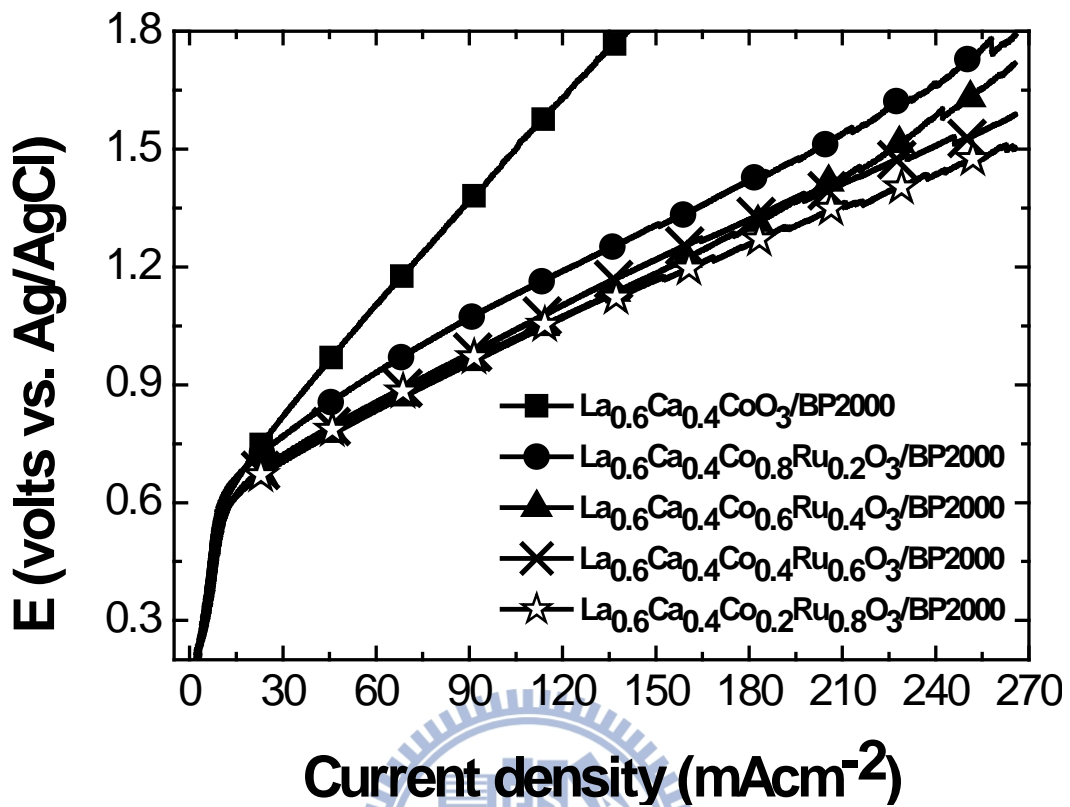
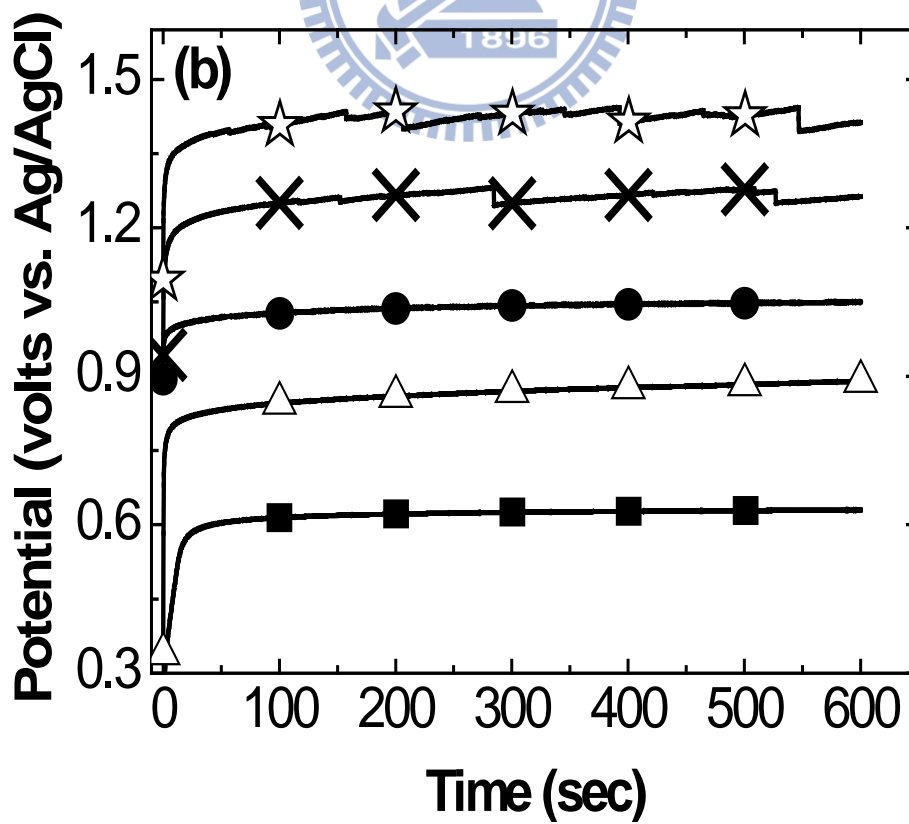
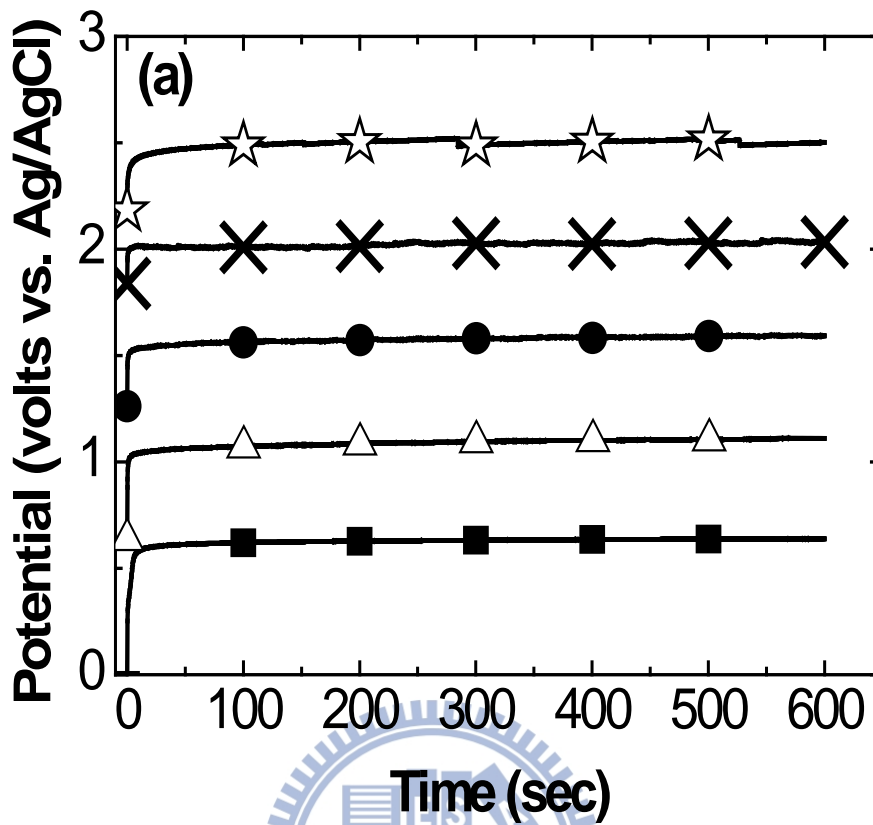


Figure 4.19 The charging I-V polarization curves of $\text{La}_{0.6}\text{Ca}_{0.4}\text{Co}_{1-x}\text{Ru}_x\text{O}_3/\text{BP2000}$.

Again, Fig. 4.20 provides the galvanostatic charge curves for 10 min from 10 mAcm^{-2} to 200 mAcm^{-2} . Clearly, the $\text{La}_{0.6}\text{Ca}_{0.4}\text{Co}_{1-x}\text{Ru}_x\text{O}_3/\text{BP2000}$ GDEs are consistently superior than the undoped one. Notably, these charging curves are rather flat for 10 min.



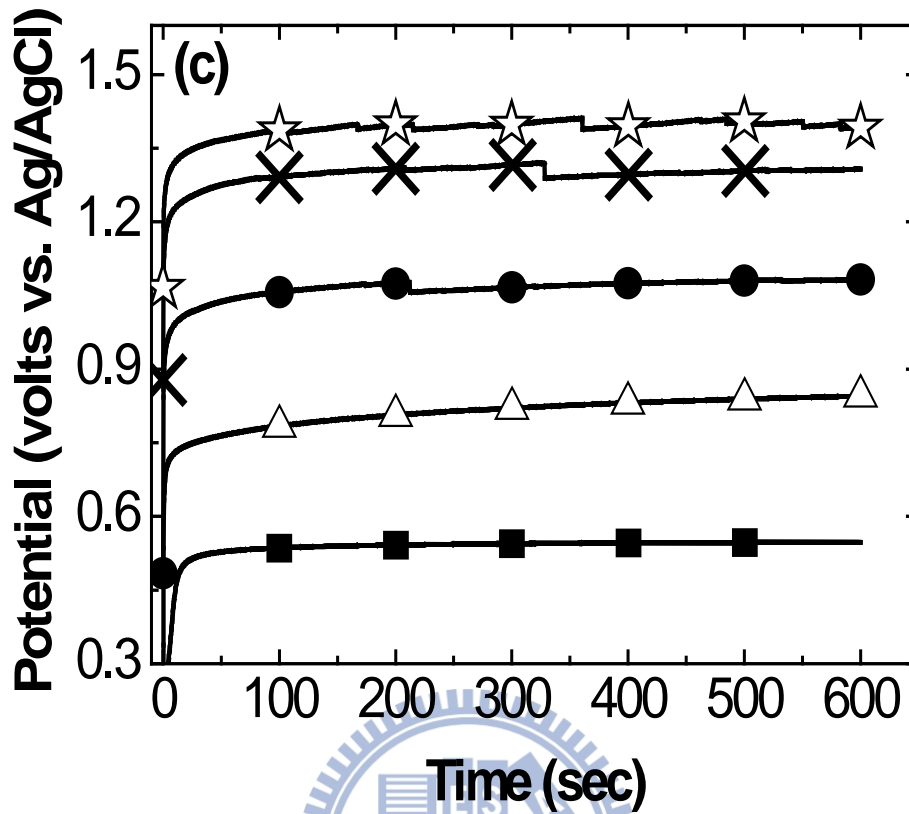


Figure 4.20 The galvanostatic charge curves for the (a) $\text{La}_{0.6}\text{Ca}_{0.4}\text{CoO}_3/\text{BP2000}$ (b) $\text{La}_{0.6}\text{Ca}_{0.4}\text{Co}_{0.8}\text{Ru}_{0.2}\text{O}_3/\text{BP2000}$ (c) $\text{La}_{0.6}\text{Ca}_{0.4}\text{Co}_{0.4}\text{Ru}_{0.6}\text{O}_3/\text{BP2000}$ at current densities of 10 mAcm^{-2} (■), 50 mAcm^{-2} (△), 100 mAcm^{-2} (●), 150 mAcm^{-2} (×), and 200 mAcm^{-2} (☆).

Finally, to confirm our Ru-doped perovskites are truly functional in practical cases, we conducted the test for 100-h discharge followed by 100-h charge at a constant current density of 30 mAcm^{-2} as shown in Fig. 4.21. Remarkably, the potential profiles are rather flat for the 200 h durations. Furthermore, the SEM images of electrode taken before and after the life time test shown in Fig. 4.22(a) and (b), respectively. Smooth carbon surfaces with a homogeneous distribution of the catalysts were observed in Fig. 4.22(a). However, the cracks on the surface of electrode were observed after the life time testing due to the oxygen pass through electrode as shown

in Fig. 4.22(b). It is suggested that the result from the cracks were formed under oxygen reduction and oxygen evolution reaction.

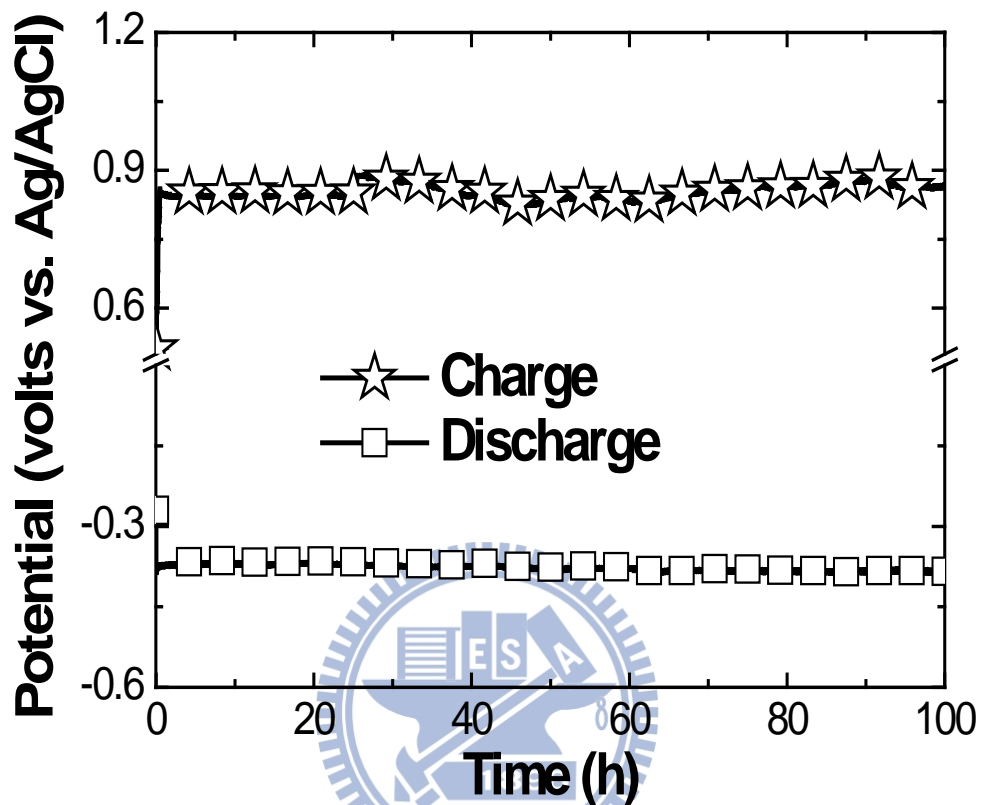


Figure 4.21 The life time testing of the $\text{La}_{0.6}\text{Ca}_{0.4}\text{Co}_{0.4}\text{Ru}_{0.6}\text{O}_3/\text{BP2000}$ GDE for 100 h discharge followed by 100 h charge at a constant current density of 30 mAcm^{-2} .

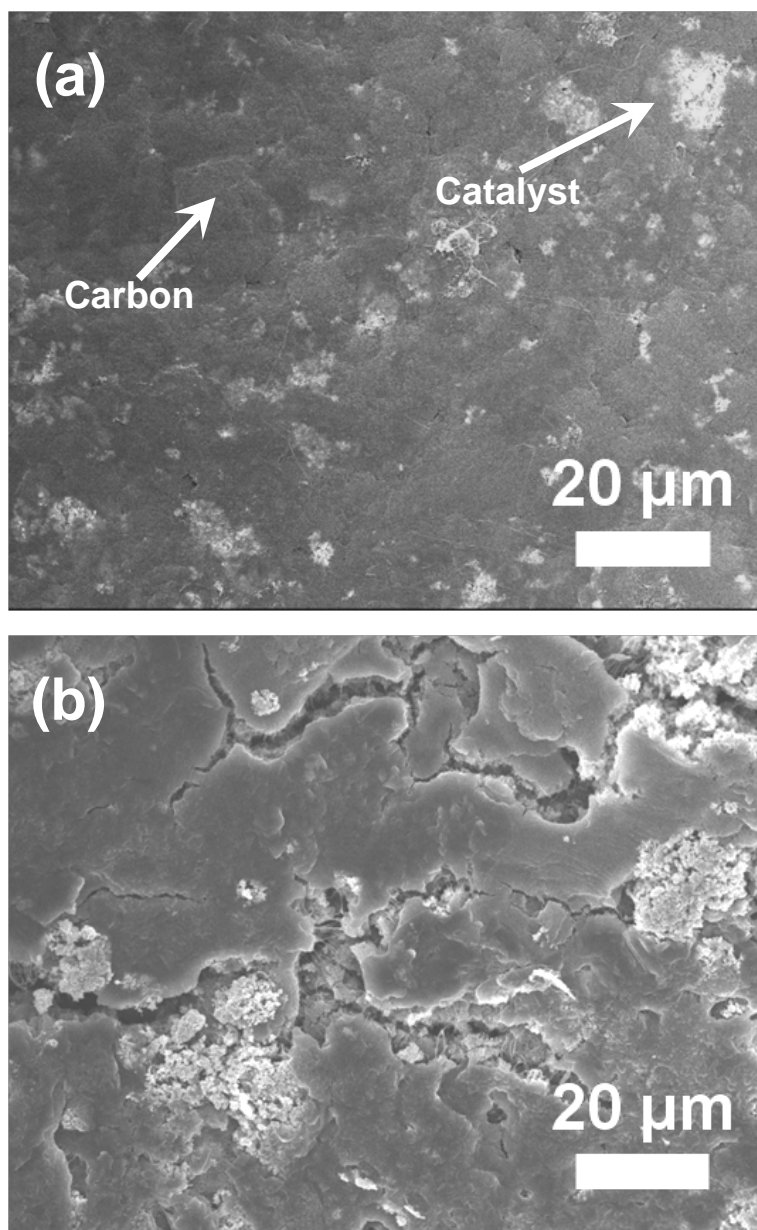


Figure 4.22 The SEM images of $\text{La}_{0.6}\text{Ca}_{0.4}\text{Co}_{0.4}\text{Ru}_{0.6}\text{O}_3/\text{BP2000}$ GDE (a) before and (b) after life time testing.

Chapter 5 Synthesis and Characterization of $\text{La}_{0.6}\text{Ca}_{0.4}\text{CoIr}_{0.25}\text{O}_{3.5-\delta}$ and $\text{La}_{0.6}\text{Ca}_{0.4}\text{Co}_{0.8}\text{Ir}_{0.2}\text{O}_3$ for Bi-functional Electrodes

5.1 Physico-chemical characterizations

First developed by Benjamin *et al.*, the mechanical alloying process has become a mature technique to fabricate metastable phases that are difficult to synthesize from conventional routes [139]. It typically involves a high energy milling treatment at room temperature to break/coalesce constituent powders depending on their brittle or ductile features. To date, the mechanical alloying was demonstrated to prepare mixed oxide powders of $\text{RuO}_2\text{-SnO}_2$ as well as binary PtRu alloys for electrocatalytic applications [140,141].

Fig. 5.1 presents the XRD patterns of IrO_2 , ACP-derived $\text{La}_{0.6}\text{Ca}_{0.4}\text{CoO}_3$, $\text{La}_{0.6}\text{Ca}_{0.4}\text{CoIr}_{0.25}\text{O}_{3.5-\delta}$ after mechanical alloying process, and ACP-derived $\text{La}_{0.6}\text{Ca}_{0.4}\text{Co}_{0.8}\text{Ir}_{0.2}\text{O}_3$. The XRD result of the IrO_2 (Fig. 5.1(a)) exhibited a rutile structure while the ACP derived powders indicated pure perovskite $\text{La}_{0.6}\text{Ca}_{0.4}\text{CoO}_3$ (Fig. 5.1(b)), which agrees perfectly with the $\text{La}_{0.6}\text{Ca}_{0.4}\text{CoO}_3$ JCPDS standard data (35.1389). Similarly, we observed an extra diffraction peak at $2\theta=36.90^\circ$. Simultaneous presence of these noises indicated that the undesirable phase comes from residue inherent to the ACP synthesis. This suggested heat treatment of 550°C in

air for 4 h is sufficient to decompose the precursors and form the desirable perovskite phase. After mechanical alloying for 12 h, the resulting powders exhibited a pattern that contains all the diffraction peaks of $\text{La}_{0.6}\text{Ca}_{0.4}\text{CoO}_3$, confirming successful incorporation of Ir^{4+} at Co^{3+} sites as shown in Fig. 5.1(c). However, the XRD pattern of the resulting powders exhibited moderate noises inferring likely compromise in crystallinity during the high energy ball milling process. Structural alteration sustained during mechanical alloying was not unexpected [142]. Nevertheless, it is to be noted that IrO_2 peaks disappeared entirely. This confirms the result reported earlier by Gaudet *et al.* that mechanical alloying is an effective method to prepare mixed oxides in a single phase without involving solution state mixing and high temperature diffusion [140].

On the other hand, XRD results for the ACP-derived $\text{La}_{0.6}\text{Ca}_{0.4}\text{Co}_{0.8}\text{Ir}_{0.2}\text{O}_3$ powders are provided in Fig. 5.1(d). As shown in Fig. 5.1(d), ACP-derived $\text{La}_{0.6}\text{Ca}_{0.4}\text{Co}_{0.8}\text{Ir}_{0.2}\text{O}_3$ exhibited a crystalline perovskite phase (ABO_3). Unfortunately, there were minor signals possibly from the oxides of La_2O_3 ($2\theta = 36.84^\circ$) and Co_3O_4 ($2\theta = 65.08^\circ$). Nevertheless, we did not observe any diffraction peak from IrO_2 , suggesting that the incorporation of Ir^{4+} at the Co cation sites was achieved as expected. Calculation of the lattice parameters using high angle diffraction peaks indicated at $c = 13.25 \text{ \AA}$ and $a = 5.44 \text{ \AA}$ for c and a axis, respectively. These values are slightly larger than those of $\text{La}_{0.6}\text{Ca}_{0.4}\text{CoO}_3$ ($c = 13.09 \text{ \AA}$ and $a = 5.43 \text{ \AA}$) from standard JCPDS stand data 35.1389. The volume expansion is expected because the size of Ir^{4+} (0.76 \AA) is larger than that of Co^{3+} ($\text{Co}^{3+} = 0.69 \text{ \AA}$ and $\text{Co}^{4+} = 0.67 \text{ \AA}$). Again, the diffraction peaks of ACP-derived $\text{La}_{0.6}\text{Ca}_{0.4}\text{Co}_{0.8}\text{Ir}_{0.2}\text{O}_3$ matched well with those of the standard $\text{La}_{0.6}\text{Ca}_{0.4}\text{CoO}_3$ perovskite.

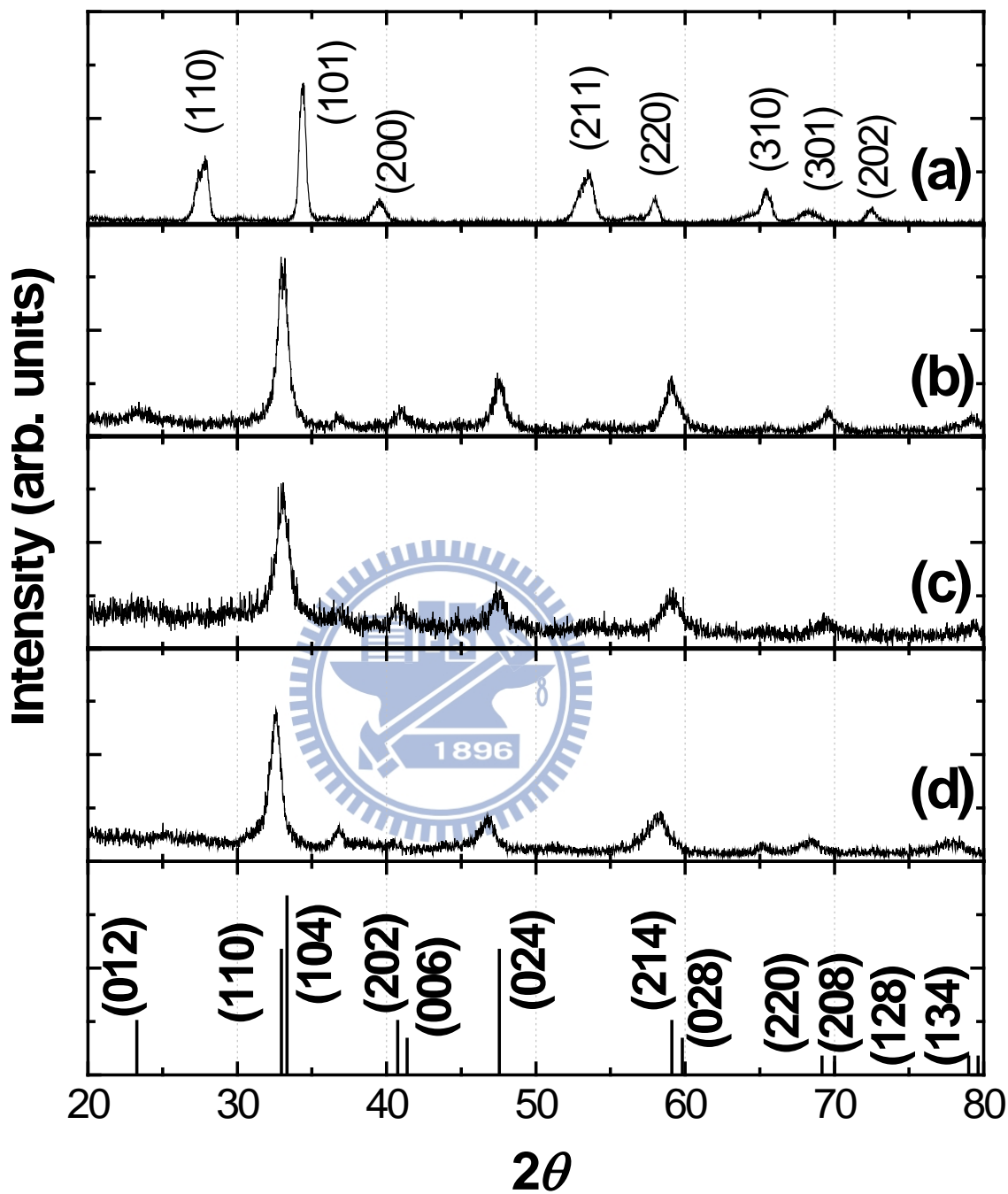


Figure 5.1 X-ray results of (a) IrO_2 , (b) ACP-derived $\text{La}_{0.6}\text{Ca}_{0.4}\text{CoO}_3$, (c) $\text{La}_{0.6}\text{Ca}_{0.4}\text{CoIr}_{0.25}\text{O}_{3.5-\delta}$ from the mechanical alloying process, and (d) ACP-derived $\text{La}_{0.6}\text{Ca}_{0.4}\text{Co}_{0.8}\text{Ir}_{0.2}\text{O}_3$.

Previous studies reported the preparations of materials by the mechanical alloying in which the resulting compositions are simply a solid solution of individual constituents, or incorporation of the minority phase into the majority phase [143-147]. In our case after mechanical alloying, the XRD results of the powders indicated complete disappearance of the minority phase of rutile IrO_2 and the majority phase of perovskite $\text{La}_{0.6}\text{Ca}_{0.4}\text{CoO}_3$ remained relatively intact. This suggested that Ir^{4+} and O^{2-} are incorporated into the perovskite matrix. Hence, the composition of the resulted powders is $\text{La}_{0.6}\text{Ca}_{0.4}\text{CoIr}_{0.25}\text{O}_{3.5}$.

To further investigate the exact composition of the resulting powders, we adopted the iodometric titration method, which has been used extensively in literatures to estimate the composition of complex oxides [147,148]. The iodometric titration was carried out to determine the oxygen content of the perovskite indirectly by calculating the average oxidation state of Co cations. This is because variations of the oxygen content in the perovskite structure reflects changes in the oxidation state of Co cations. In our samples, the average oxidation state of Co cations from the iodometric titration measurements is 3.2 assuming the Ir cations remain as Ir^{4+} . Therefore, the composition of our powders is estimated as $\text{La}_{0.6}\text{Ca}_{0.4}\text{CoIr}_{0.25}\text{O}_{3.4069}$. Combining information from literature reports as well as experimental results from the iodometric titration we believe it is appropriate to label our material as $\text{La}_{0.6}\text{Ca}_{0.4}\text{CoIr}_{0.25}\text{O}_{3.5-\delta}$.

We also attempted to synthesize $\text{La}_{0.6}\text{Ca}_{0.4}\text{CoO}_3$ from SSR route at identical conditions like that of $\text{La}_{0.6}\text{Ca}_{0.4}\text{Co}_{0.8}\text{Ir}_{0.2}\text{O}_3$. However, instead of the desirable perovskite phases we obtained the mixed phase powders as revealed by the XRD result of provided in Fig. 5.2. Therefore, we did not carry out further electrochemical

characterizations. However, we believe the ACP-derived $\text{La}_{0.6}\text{Ca}_{0.4}\text{CoO}_3$ should serve as a good benchmark. In our recent publication [55], the ACP-derived $\text{La}_{0.6}\text{Ca}_{0.4}\text{CoO}_3$ was used as the reference because it exhibited a pure perovskite phase as shown in Fig. 5.1(b).

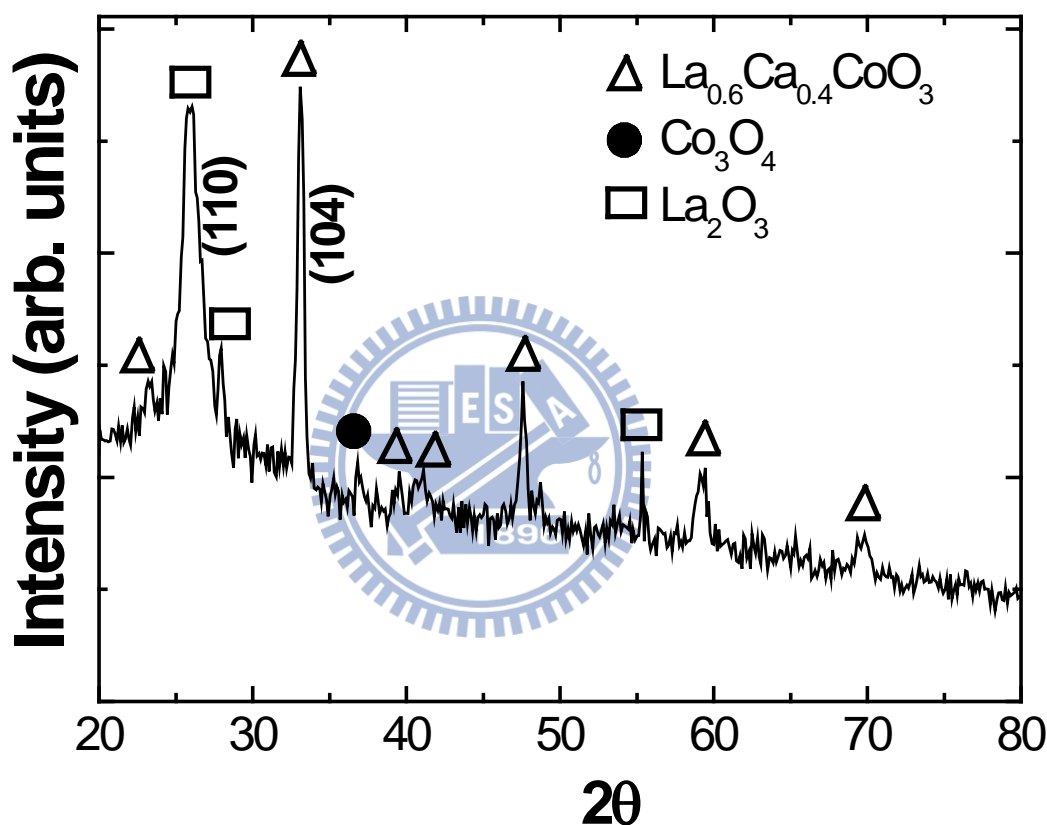
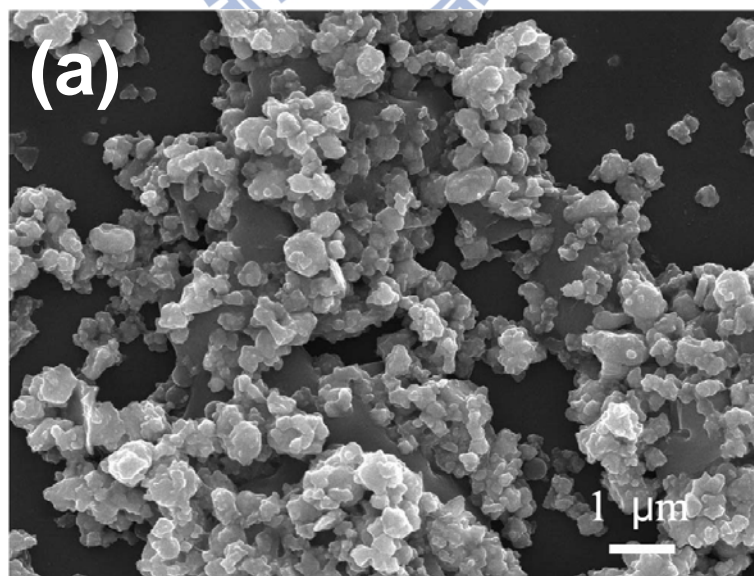


Figure 5.2 The XRD profile of the SSR-derived $\text{La}_{0.6}\text{Ca}_{0.4}\text{CoO}_3$ from SSR route.

Fig. 5.3(a) exhibits the SEM image of $\text{La}_{0.6}\text{Ca}_{0.4}\text{CoIr}_{0.25}\text{O}_{3.5-\delta}$ powders after mechanical alloying. The powders mixtures exhibited particles aggregated in irregular shape with primary particles of 300-500 nm in sizes. Prior to the mechanical alloying, the particle sizes of IrO_2 were between 10-30 nm. Some coalescence of oxides

particles resulting from mechanical alloying was observed. The picture for $\text{La}_{0.6}\text{Ca}_{0.4}\text{CoO}_3$ (shown in Fig. 5.3(b)) reveals a foam-like morphology, with larger pores of 445 nm. The SEM image is consistent with BET measurements in reduction of surface area from $9.51 \text{ m}^2\text{g}^{-1}$ of ACP-derived $\text{La}_{0.6}\text{Ca}_{0.4}\text{CoO}_3$ to $5.62 \text{ m}^2\text{g}^{-1}$ of $\text{La}_{0.6}\text{Ca}_{0.4}\text{CoIr}_{0.25}\text{O}_{3.5-\delta}$. As shown in Fig. 5.3(c), ACP-derived $\text{La}_{0.6}\text{Ca}_{0.4}\text{Co}_{0.8}\text{Ir}_{0.2}\text{O}_3$ appeared in a foam-like structure with the presence of micropores of 245 nm size. Individual particles were not discernible, and the aggregates had irregular shapes. The appearance of a foam-like microstructure is expected because our sintering process was carried out under relatively mild conditions, i.e., 650°C for 4 h. We realize that sintering at higher temperatures could produce larger particles with excessive coalescence. BET measurements on the ACP-derived $\text{La}_{0.6}\text{Ca}_{0.4}\text{Co}_{0.8}\text{Ir}_{0.2}\text{O}_3$ powders indicated the surface area is $13.31 \text{ m}^2\text{g}^{-1}$.



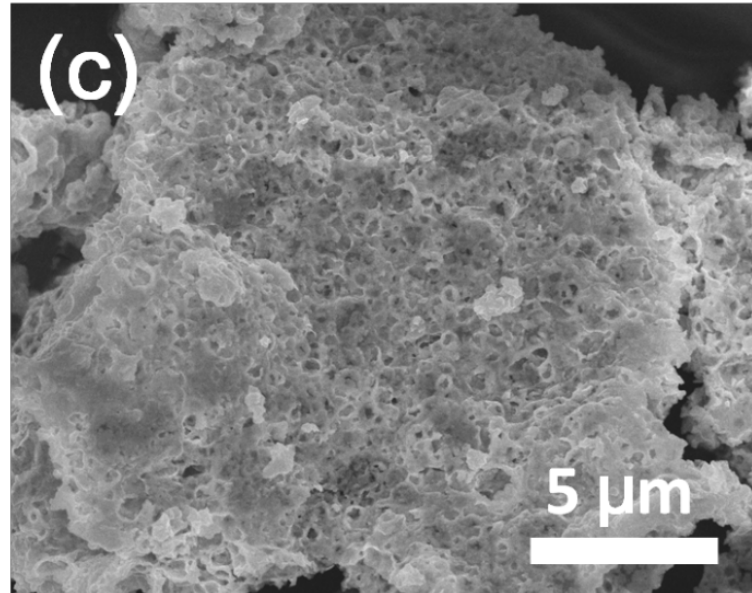
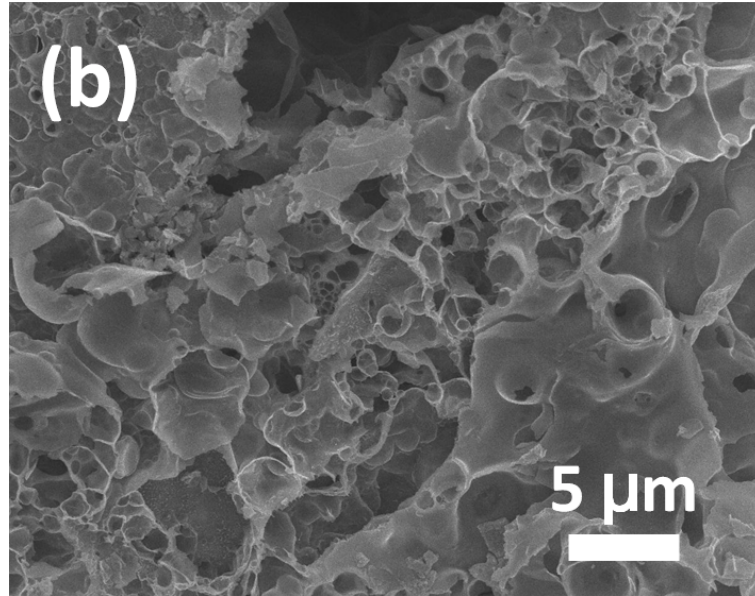


Figure 5.3 The SEM image of (a) $\text{La}_{0.6}\text{Ca}_{0.4}\text{CoIr}_{0.25}\text{O}_{3.5-\delta}$ after the mechanical alloying process, (b) $\text{La}_{0.6}\text{Ca}_{0.4}\text{CoO}_3$, and (c) ACP-derived $\text{La}_{0.6}\text{Ca}_{0.4}\text{Co}_{0.8}\text{Ir}_{0.2}\text{O}_3$.

In addition, the EDX mapping of the $\text{La}_{0.6}\text{Ca}_{0.4}\text{CoIr}_{0.25}\text{O}_{3.5-\delta}$ powders indicated uniform distributions of Ir as shown in Fig. 5.4. Our results suggest successful incorporation of Ir^{4+} at the Co cation sites, confirming the formation of $\text{La}_{0.6}\text{Ca}_{0.4}\text{CoIr}_{0.25}\text{O}_{3.5-\delta}$.

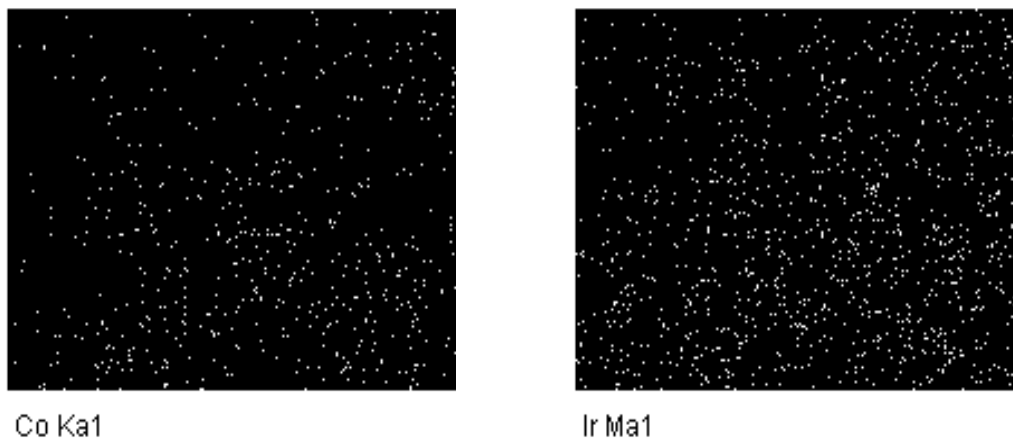
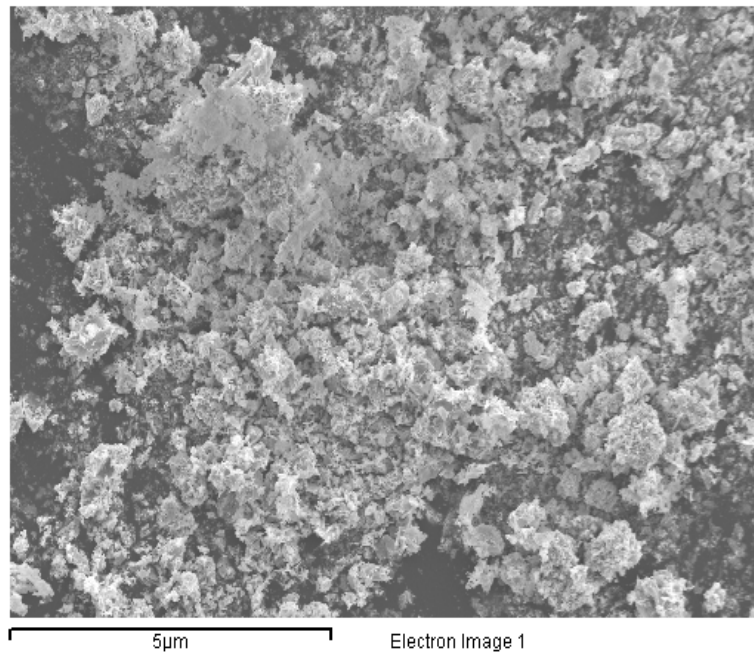


Figure 5.4 The EDX mapping of $\text{La}_{0.6}\text{Ca}_{0.4}\text{CoIr}_{0.25}\text{O}_{3.5-\delta}$.

5.2 Electrochemical characterizations

In our earlier study of oxygen reduction electrocatalysts in alkaline electrolyte, we identified the CNCs as the excellent substrates for catalyst support [23]. We attributed their superb characteristics to near spherical shape with graphene layers on perimeters. The CNCs ($330 \text{ m}^2\text{g}^{-1}$) were produced by incomplete combustion of C_2H_2 and O_2 with the resulting particles between 10-30 nm as shown in Fig. 5.5. TEM images indicated CNCs with good uniformity. Detailed processing parameters for CNCs synthesis was reported by Liu and Li [76].

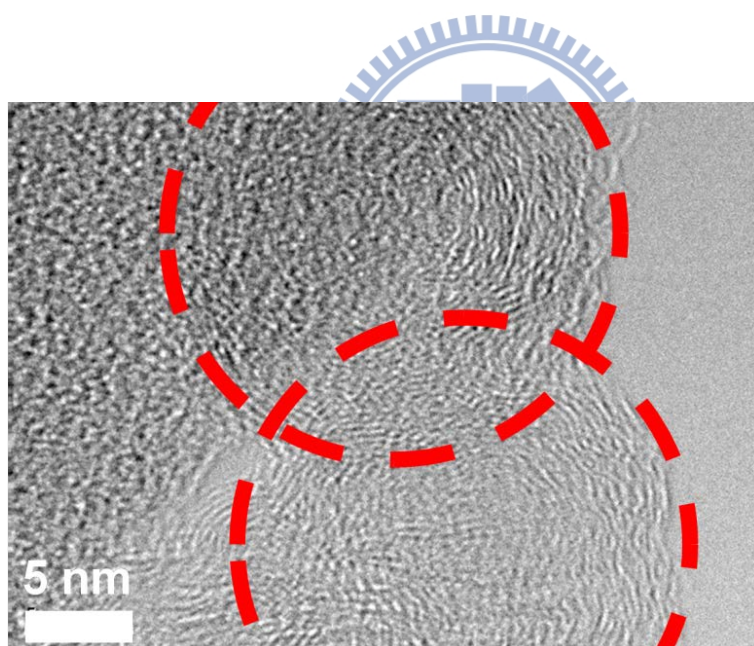


Figure 5.5 Images for CNCs from TEM.

Fig. 5.6 presents the I-V polarizations in discharge mode conducted on GDEs that were catalyzed by $\text{La}_{0.6}\text{Ca}_{0.4}\text{CoO}_3$, IrO_2/CNCs , $\text{La}_{0.6}\text{Ca}_{0.4}\text{CoO}_3/\text{CNCs}$, and $\text{La}_{0.6}\text{Ca}_{0.4}\text{CoIr}_{0.25}\text{O}_{3.5-\delta}/\text{CNCs}$. In addition, noncatalyzed GDEs were evaluated as the reference. In I-V profiles, the voltage readings started from 1.6 V and decreased

gradually with increasing current. Among these discharge curves the $\text{La}_{0.6}\text{Ca}_{0.4}\text{CoIr}_{0.25}\text{O}_{3.5-\delta}/\text{CNCs}$ revealed the highest catalytic ability, delivering 0.980 V at 100 mAcm^{-2} . This is a significant 89 mV enhancement over that of $\text{La}_{0.6}\text{Ca}_{0.4}\text{CoO}_3/\text{CNCs}$. Interestingly, the $\text{La}_{0.6}\text{Ca}_{0.4}\text{CoIr}_{0.25}\text{O}_{3.5-\delta}/\text{CNCs}$ behaves better than IrO_2/CNCs at high current density. In contrast, unsupported $\text{La}_{0.6}\text{Ca}_{0.4}\text{CoO}_3$ showed rapid deteriorations in I-V discharge, approaching noncatalyzed GDEs at current density above 175 mAcm^{-2} . The notable improvement of $\text{La}_{0.6}\text{Ca}_{0.4}\text{CoO}_3$ on CNCs in catalytic ability was expected as previous reports have documented synergistic effect in combining perovskites with carbonaceous supports [48,58]. It is because carbon produces peroxide ions in reduction reaction while the presence of perovskites promotes the decomposition of peroxide ions.

The I-V polarizations in charging mode for IrO_2/CNCs , $\text{La}_{0.6}\text{Ca}_{0.4}\text{CoO}_3/\text{CNCs}$, $\text{La}_{0.6}\text{Ca}_{0.4}\text{CoIr}_{0.25}\text{O}_{3.5-\delta}/\text{CNCs}$, and noncatalyzed GDE were shown in Fig. 5.7. In charging reaction, oxygen was produced and released from the GDE. Generally, the oxygen evolution reaction incurs a much larger polarization loss as compared to the oxygen reduction at identical current density. From the diagram, the voltage started from 1.6 V and moved to higher voltages with increasing current density. The GDE catalyzed by $\text{La}_{0.6}\text{Ca}_{0.4}\text{CoIr}_{0.25}\text{O}_{3.5-\delta}/\text{CNCs}$ demonstrated impressive catalytic performances, showing a charging voltage of 2.104 V at 50 mAcm^{-2} . For current density between 0 and 150 mAcm^{-2} , $\text{La}_{0.6}\text{Ca}_{0.4}\text{CoIr}_{0.25}\text{O}_{3.5-\delta}/\text{CNCs}$ exhibited performance improvements of 67 mV over those of $\text{La}_{0.6}\text{Ca}_{0.4}\text{CoO}_3/\text{CNCs}$. Although the IrO_2/CNCs was superior than that of $\text{La}_{0.6}\text{Ca}_{0.4}\text{CoO}_3/\text{CNCs}$, its performance was still inferior to that of $\text{La}_{0.6}\text{Ca}_{0.4}\text{CoIr}_{0.25}\text{O}_{3.5-\delta}/\text{CNCs}$ at low current densities. In contrast, the noncatalyzed GDE revealed negligible catalytic abilities with a sharp rise

in the charging voltage. Our results confirmed that the addition of Ir^{4+} in the lanthanum cobaltate is beneficial for bi-functional catalytic abilities. Notably, the surface area of $\text{La}_{0.6}\text{Ca}_{0.4}\text{CoIr}_{0.25}\text{O}_{3.5-\delta}/\text{CNCs}$ are smaller than that of $\text{La}_{0.6}\text{Ca}_{0.4}\text{CoO}_3$. Therefore, we are confident that the observed enhancements in I-V performances are due to the intrinsic superiority of $\text{La}_{0.6}\text{Ca}_{0.4}\text{CoIr}_{0.25}\text{O}_{3.5-\delta}/\text{CNCs}$.

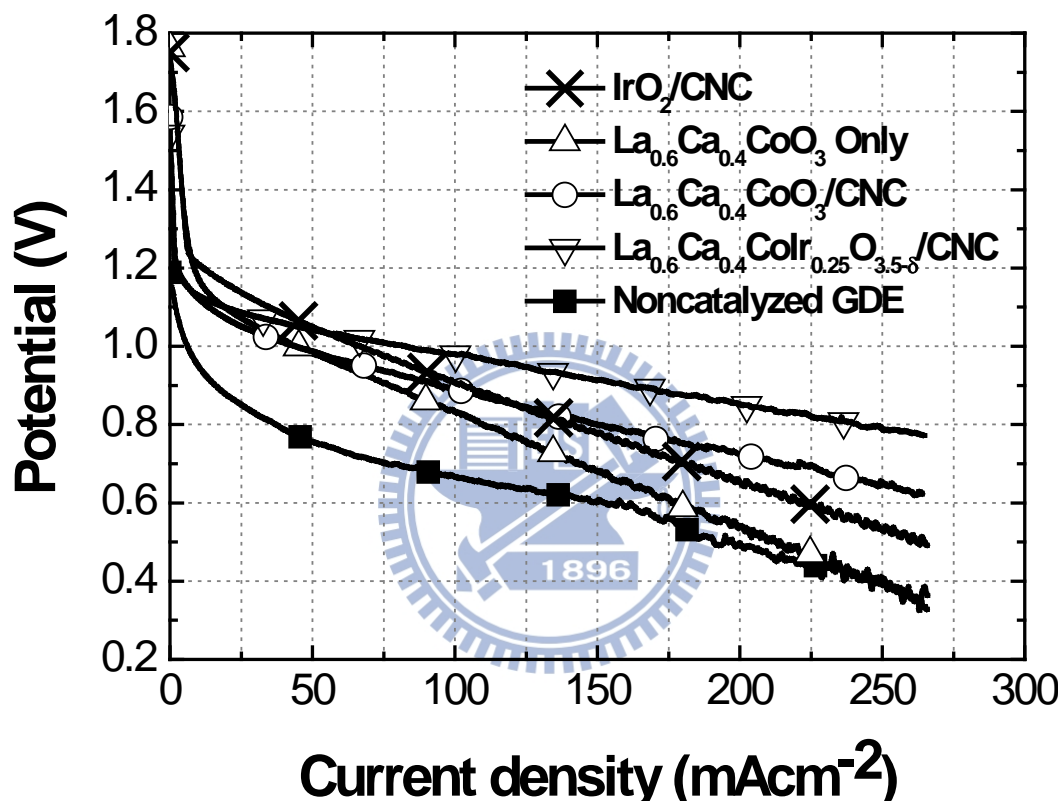


Figure 5.6 The discharging I-V polarization curves of the noncatalyzed GDE, and catalyzed GDEs with electrocatalysts of IrO_2/CNCs , $\text{La}_{0.6}\text{Ca}_{0.4}\text{CoO}_3$, $\text{La}_{0.6}\text{Ca}_{0.4}\text{CoO}_3/\text{CNCs}$, and $\text{La}_{0.6}\text{Ca}_{0.4}\text{CoIr}_{0.25}\text{O}_{3.5-\delta}/\text{CNCs}$.

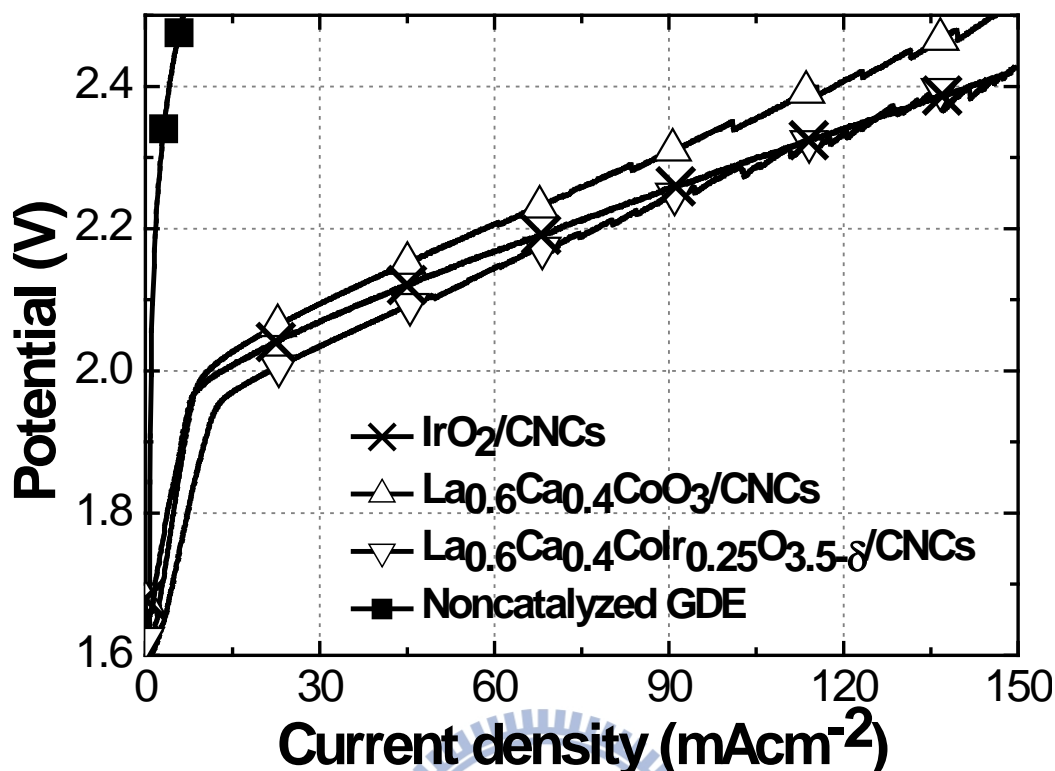


Figure 5.7 The charging I-V polarization curves of the noncatalyzed GDE and catalyzed GDEs with electrocatalysts of IrO₂/CNCs, La_{0.6}Ca_{0.4}CoO₃/CNCs, and La_{0.6}Ca_{0.4}CoIr_{0.25}O_{3.5-δ}/CNCs.

Further studies in catalytic performance of La_{0.6}Ca_{0.4}CoIr_{0.25}O_{3.5-δ}/CNCs were carried out in galvanostatic charging and discharging modes for duration of 10 min at current density of 25 and 100 mAcm⁻², respectively. Their results were shown in Fig. 5.8 along with those of La_{0.6}Ca_{0.4}CoO₃/CNCs. For both charging and discharging, the voltage readings were in line with those reported in polarization experiments. In addition, both galvanostatic profiles were rather flat confirming electrocatalysts of La_{0.6}Ca_{0.4}CoO₃/CNCs and La_{0.6}Ca_{0.4}CoIr_{0.25}O_{3.5-δ}/CNCs were stable in alkaline electrolyte and their performances were sustainable. For both charging and discharging, the electrocatalytic performances of La_{0.6}Ca_{0.4}CoIr_{0.25}O_{3.5-δ}/CNCs surpassed those of La_{0.6}Ca_{0.4}CoO₃/CNC. This effectively demonstrates that

incorporation of Ir^{4+} in the $\text{La}_{0.6}\text{Ca}_{0.4}\text{CoO}_3$ structure leads to a remarkable improvement in bi-functional ability.

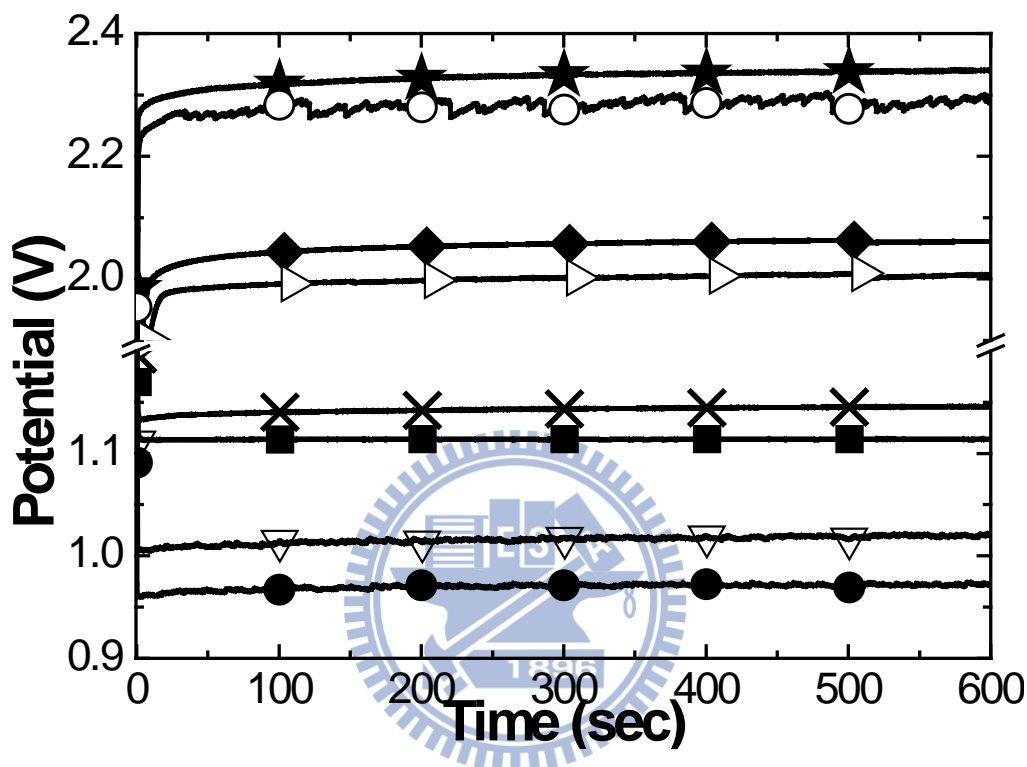


Figure 5.8 $\text{La}_{0.6}\text{Ca}_{0.4}\text{CoO}_3/\text{CNCs}$ galvanostatic discharging curves at (a) \blacksquare 25 and (b) \bullet 100 mAcm^{-2} and charging curves at (c) \blacklozenge 25 and (d) \blackstar 100 mAcm^{-2} . $\text{La}_{0.6}\text{Ca}_{0.4}\text{CoIr}_{0.25}\text{O}_{3.5-\delta}/\text{CNCs}$ galvanostatic discharging curves at (a) \times 25 and (b) ∇ 100 mAcm^{-2} and charging curves at (c) \triangleright 25 and (d) \circ 100 mAcm^{-2} .

Fig. 5.9 shows the oxygen reduction I–V curves for the noncatalyzed GDE and catalyzed GDEs with $\text{La}_{0.6}\text{Ca}_{0.4}\text{Co}_{0.8}\text{Ir}_{0.2}\text{O}_3$ only, $\text{La}_{0.6}\text{Ca}_{0.4}\text{CoO}_3/\text{CNCs}$, and ACP-derived $\text{La}_{0.6}\text{Ca}_{0.4}\text{Co}_{0.8}\text{Ir}_{0.2}\text{O}_3$. Also shown is the commercial catalyst (MnO_x) from eVionyx Inc. The profiles exhibited typical I–V polarizations in which the potential values decreased steadily from 1.60 V with increasing current densities.

Among these samples, ACP-derived $\text{La}_{0.6}\text{Ca}_{0.4}\text{Co}_{0.8}\text{Ir}_{0.2}\text{O}_3/\text{CNCs}$ demonstrated the best performance, delivering 1.047 and 0.932 V at 100 and 200 mAcm^{-2} , respectively. In contrast, $\text{La}_{0.6}\text{Ca}_{0.4}\text{CoO}_3/\text{CNCs}$ maintained a potential of 0.891 and 0.723 V at identical current densities. There was a 209 mV enhancement at 200 mAcm^{-2} for ACP-derived $\text{La}_{0.6}\text{Ca}_{0.4}\text{Co}_{0.8}\text{Ir}_{0.2}\text{O}_3/\text{CNCs}$. Moreover, ACP-derived $\text{La}_{0.6}\text{Ca}_{0.4}\text{Co}_{0.8}\text{Ir}_{0.2}\text{O}_3/\text{CNCs}$ performed better than MnO_x . In contrast, the GDE with unsupported ACP-derived $\text{La}_{0.6}\text{Ca}_{0.4}\text{Co}_{0.8}\text{Ir}_{0.2}\text{O}_3$ only demonstrated rapid voltage deterioration with increasing current densities. Again, this behavior is consistent with earlier observations in which a synergistic effect was observed for GDEs catalyzed by perovskites supported on carbons [48,58]. Lastly, the noncatalyzed GDE showed negligible catalytic behaviors, as expected.

The oxygen evolution I–V curves for the noncatalyzed GDE, as well as GDEs catalyzed by ACP-derived $\text{La}_{0.6}\text{Ca}_{0.4}\text{Co}_{0.8}\text{Ir}_{0.2}\text{O}_3/\text{CNCs}$, $\text{La}_{0.6}\text{Ca}_{0.4}\text{CoO}_3/\text{CNCs}$, and IrO_2/CNCs are provided in Fig. 5.10. Since the oxygen evolution is kinetically challenging, the polarization loss is expected to be more severe as compared to the oxygen reduction at identical current densities. As shown, the voltage started at 1.60 V and moved rapidly to higher values with increasing current densities. Apparently, the noncatalyzed GDE showed limited oxygen evolution performance. In contrast, the GDE catalyzed by ACP-derived $\text{La}_{0.6}\text{Ca}_{0.4}\text{Co}_{0.8}\text{Ir}_{0.2}\text{O}_3/\text{CNCs}$ demonstrated remarkable catalytic abilities, exhibiting the voltages of 2.046 and 2.178 V at 50 and 100 mAcm^{-2} , respectively. At identical current densities, the voltage readings from $\text{La}_{0.6}\text{Ca}_{0.4}\text{CoO}_3/\text{CNCs}$ were 2.171 and 2.347 V, respectively. The GDE catalyzed by IrO_2/CNCs showed slightly better behavior than $\text{La}_{0.6}\text{Ca}_{0.4}\text{CoO}_3/\text{CNCs}$ but was still outperformed by ACP-derived $\text{La}_{0.6}\text{Ca}_{0.4}\text{Co}_{0.8}\text{Ir}_{0.2}\text{O}_3/\text{CNCs}$. The results from the I–V

measurements for oxygen reduction and evolution were encouraging. With the introduction of Ir at the Co cation sites, we not only observed the improvements in the catalysis for the oxygen evolution, but also better oxygen reduction behaviors.

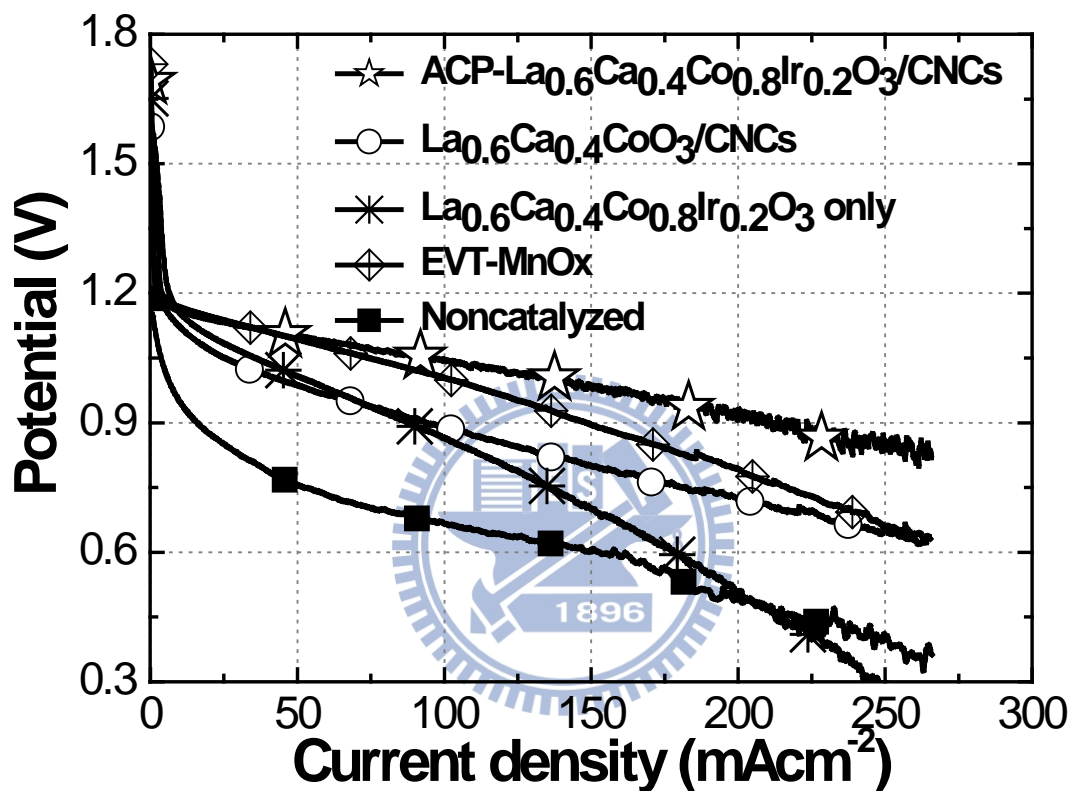


Figure 5.9 Oxygen reduction I-V polarization curves of MnO_x, noncatalyzed GDE, and catalyzed GDEs with La_{0.6}Ca_{0.4}Co_{0.8}Ir_{0.2}O₃ only, La_{0.6}Ca_{0.4}CoO₃/CNCs, and ACP-derived La_{0.6}Ca_{0.4}Co_{0.8}Ir_{0.2}O₃/CNCs.

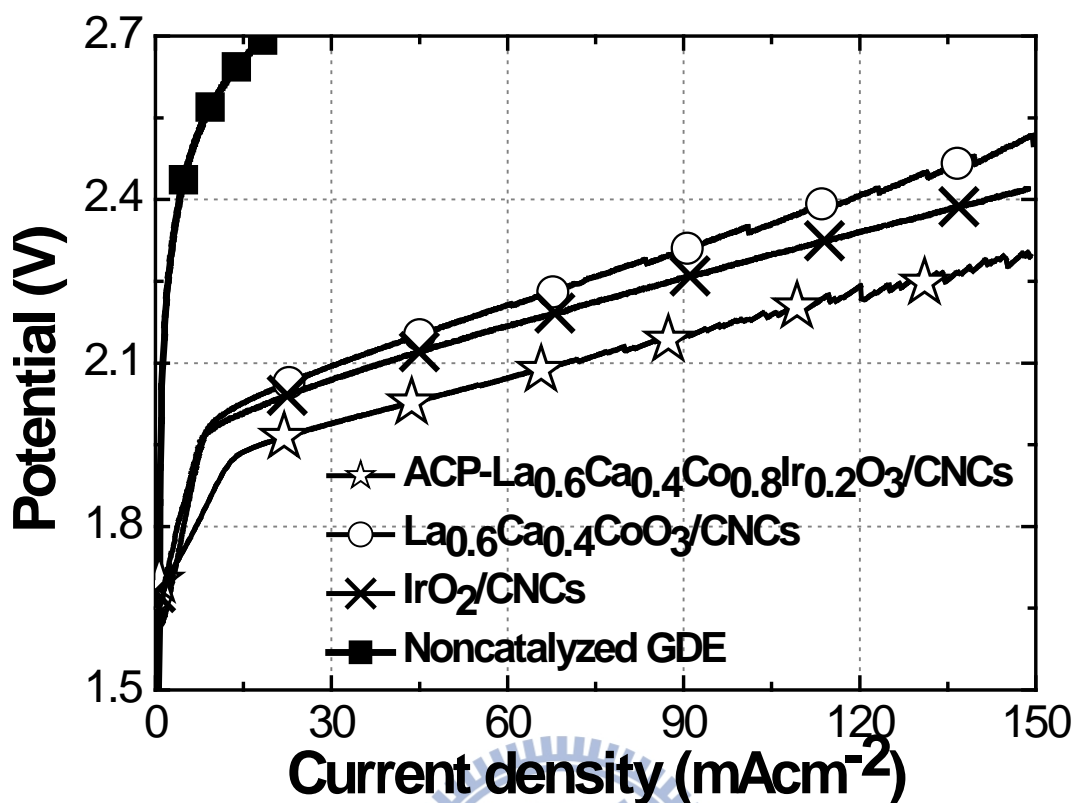


Figure 5.10 Oxygen evolution I-V polarization curves of noncatalyzed GDE and catalyzed GDEs with ACP-derived $\text{La}_{0.6}\text{Ca}_{0.4}\text{Co}_{0.8}\text{Ir}_{0.2}\text{O}_3/\text{CNCs}$, $\text{La}_{0.6}\text{Ca}_{0.4}\text{CoO}_3/\text{CNCs}$, and IrO_2/CNCs .

Fig. 5.11 exhibits the I-V polarizations in discharging mode conducted on the GDEs that were catalyzed by $\text{La}_{0.6}\text{Ca}_{0.4}\text{CoIr}_{0.25}\text{O}_{3.5-8}/\text{CNCs}$, and ACP-derived $\text{La}_{0.6}\text{Ca}_{0.4}\text{Co}_{0.8}\text{Ir}_{0.2}\text{O}_3/\text{CNCs}$. In addition, the noncatalyzed GDE was adopted as the reference. They are benchmarked against noncatalyzed GDE and showed much improved performance, delivering in between 0 and 250 mAcm^{-2} . For incorporation of Ir^{4+} in the $\text{La}_{0.6}\text{Ca}_{0.4}\text{CoO}_3$ perovskite prepared by these two methods, ACP method produces the powders with the best catalytic ability. Note that it is likely that the superior ability is a result of high surface area as BET results shown earlier.

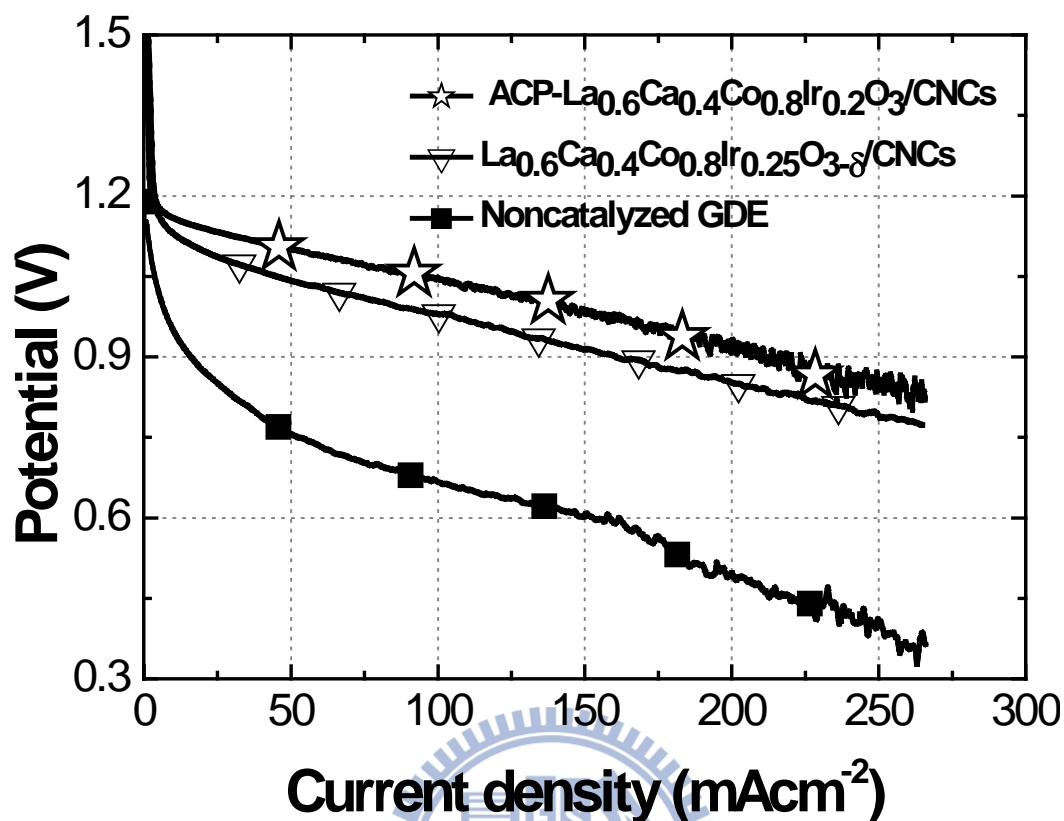


Figure 5.11 Oxygen reduction I-V polarization curves of noncatalyzed GDE and catalyzed GDEs with $\text{La}_{0.6}\text{Ca}_{0.4}\text{Co}_{0.8}\text{Ir}_{0.25}\text{O}_{3.5-\delta}/\text{CNCs}$ and ACP-derived $\text{La}_{0.6}\text{Ca}_{0.4}\text{Co}_{0.8}\text{Ir}_{0.2}\text{O}_3/\text{CNCs}$.

Fig. 5.12 provides the ORR I-V profiles for the ACP-derived $\text{La}_{0.6}\text{Ca}_{0.4}\text{Co}_{0.8}\text{Ru}_{0.2}\text{O}_3/\text{CNCs}$ and ACP-derived $\text{La}_{0.6}\text{Ca}_{0.4}\text{Co}_{0.8}\text{Ir}_{0.2}\text{O}_3/\text{CNCs}$. These curves exhibited typical I-V characteristics where the potential values were found to decrease gradually from 1.6 V with increasing current densities. As shown, both ACP-derived $\text{La}_{0.6}\text{Ca}_{0.4}\text{Co}_{0.8}\text{Ru}_{0.2}\text{O}_3/\text{CNCs}$ and ACP-derived $\text{La}_{0.6}\text{Ca}_{0.4}\text{Co}_{0.8}\text{Ir}_{0.2}\text{O}_3/\text{CNCs}$ revealed similar catalytic abilities between 0 and 210 mAcm^{-2} .

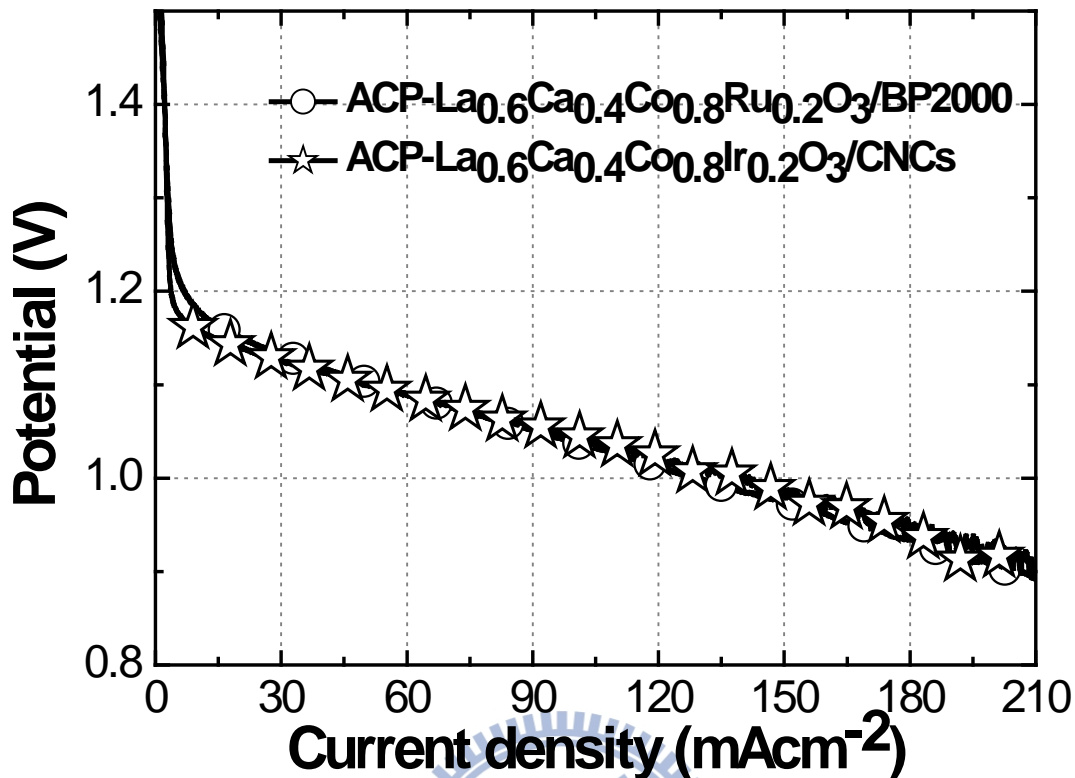


Figure 5.12 Oxygen reduction I-V polarization curves of ACP-derived $\text{La}_{0.6}\text{Ca}_{0.4}\text{Co}_{0.8}\text{Ru}_{0.2}\text{O}_3/\text{CNCs}$ and ACP-derived $\text{La}_{0.6}\text{Ca}_{0.4}\text{Co}_{0.8}\text{Ir}_{0.2}\text{O}_3/\text{CNCs}$.

Additional supporting evidence is be provided by the measurement of zeta potentials. As pointed out by Bockris and Otagawa, the point of zero charge (pzc) is an indicator of intrinsic catalytic properties because the surface characteristics of oxide powders determine their pzc values [38]. Hence, the zeta potential measurements were conducted on ACP-derived $\text{La}_{0.6}\text{Ca}_{0.4}\text{Co}_{0.8}\text{Ir}_{0.2}\text{O}_3$ and $\text{La}_{0.6}\text{Ca}_{0.4}\text{CoO}_3$ and the results are shown in Fig. 5.13. As shown, the pzc values for ACP-derived $\text{La}_{0.6}\text{Ca}_{0.4}\text{Co}_{0.8}\text{Ir}_{0.2}\text{O}_3$ and $\text{La}_{0.6}\text{Ca}_{0.4}\text{CoO}_3$ were determined to be 11.23 and 8.652, respectively. Our results were consistent with what Bockris and Otagawa had predicted: that the perovskites with pzc at high pH values between 7 and 14 were likely to possess better catalytic abilities for the oxygen evolution reaction [38].

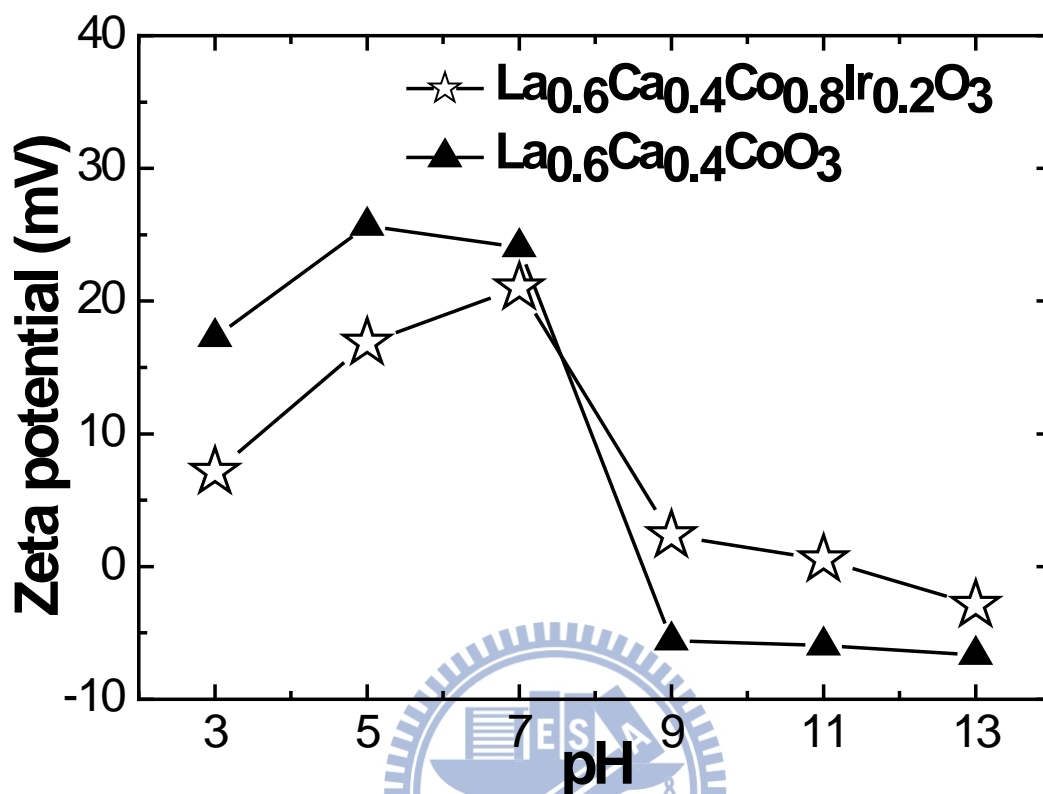


Figure 5.13 Zeta potential responses for ACP-derived $\text{La}_{0.6}\text{Ca}_{0.4}\text{Co}_{0.8}\text{Ir}_{0.2}\text{O}_3$ and $\text{La}_{0.6}\text{Ca}_{0.4}\text{CoO}_3$.

Galvanostatic measurements for the oxygen reduction reaction were carried out at current densities of 50 and 100 mAcm^{-2} for the GDEs catalyzed with ACP-derived $\text{La}_{0.6}\text{Ca}_{0.4}\text{Co}_{0.8}\text{Ir}_{0.2}\text{O}_3/\text{CNCs}$ and $\text{La}_{0.6}\text{Ca}_{0.4}\text{CoO}_3/\text{CNCs}$. Fig. 5.14 presents their respective profiles for 10 min. For both samples, the voltage plateaus were observed at and their values agreed well with those reported in earlier I–V polarization curves (shown in Fig. 5.9), indicating that the catalytic performances of ACP-derived $\text{La}_{0.6}\text{Ca}_{0.4}\text{Co}_{0.8}\text{Ir}_{0.2}\text{O}_3/\text{CNCs}$ and $\text{La}_{0.6}\text{Ca}_{0.4}\text{CoO}_3/\text{CNCs}$ were stable and sustainable. In addition, the voltage readings from ACP-derived $\text{La}_{0.6}\text{Ca}_{0.4}\text{Co}_{0.8}\text{Ir}_{0.2}\text{O}_3/\text{CNCs}$ were consistently higher than those of $\text{La}_{0.6}\text{Ca}_{0.4}\text{CoO}_3/\text{CNCs}$ for both current densities.

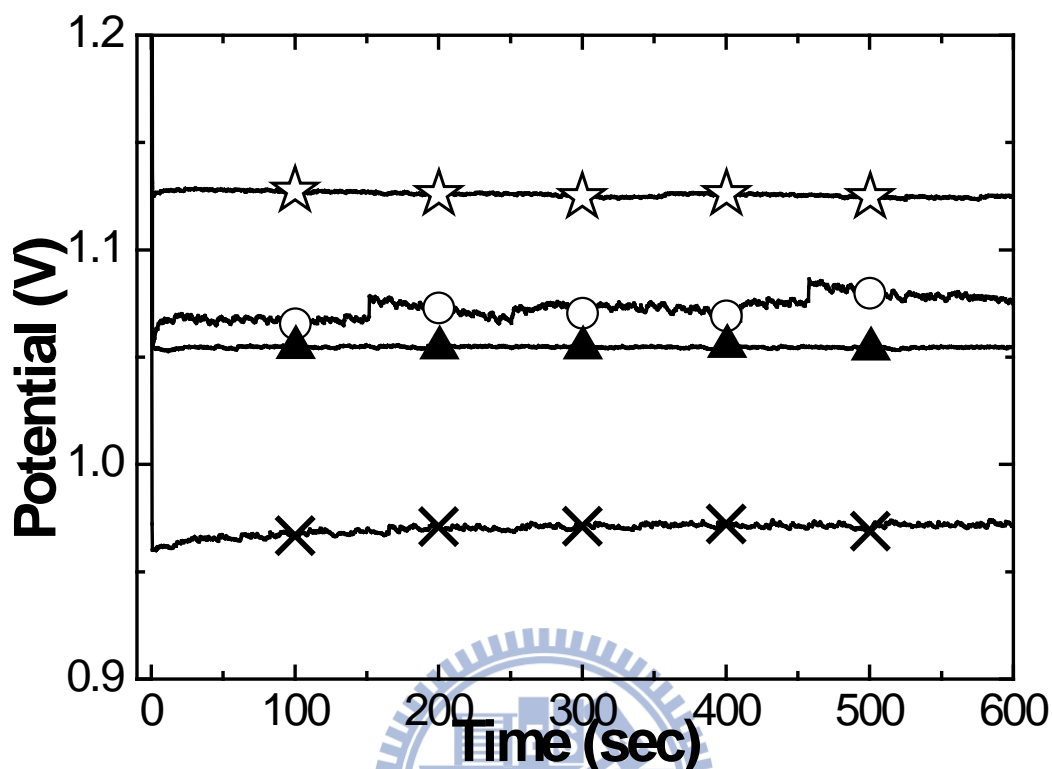


Figure 5.14 Oxygen reduction galvanostatic curves for the ACP-derived $\text{La}_{0.6}\text{Ca}_{0.4}\text{Co}_{0.8}\text{Ir}_{0.2}\text{O}_3/\text{CNCs}$ at current densities of 50 mAcm^{-2} (\star) and 100 mAcm^{-2} (\circ), as well as $\text{La}_{0.6}\text{Ca}_{0.4}\text{CoO}_3/\text{CNCs}$ at current densities of 50 mAcm^{-2} (\blacktriangle) and 100 mAcm^{-2} (\times).

Fig. 5.15 presents the oxygen evolution galvanostatic profiles for the GDEs catalyzed with ACP-derived $\text{La}_{0.6}\text{Ca}_{0.4}\text{Co}_{0.8}\text{Ir}_{0.2}\text{O}_3/\text{CNCs}$ and $\text{La}_{0.6}\text{Ca}_{0.4}\text{CoO}_3/\text{CNCs}$ at current densities of 50 and 100 mAcm^{-2} for 10 min. Again, the voltage readings agreed well with earlier I-V polarization curves (shown in Fig. 5.10), and their responses were relatively steady.

Notably, ACP-derived $\text{La}_{0.6}\text{Ca}_{0.4}\text{Co}_{0.8}\text{Ir}_{0.2}\text{O}_3/\text{CNCs}$ behaved much better than $\text{La}_{0.6}\text{Ca}_{0.4}\text{CoO}_3/\text{CNCs}$ at both current densities. Unfortunately, at a current density of

100 mAcm⁻², severe voltage fluctuations took place for both samples. Since the oxygen evolution reaction formation and detachment of oxygen bubbles at the electrode surface often resulted in the reactivation of catalytic surfaces [149,150]. As a result, a periodic reduction of overpotentials was observed.

To evaluate the bi-functional abilities of ACP-derived La_{0.6}Ca_{0.4}Co_{0.8}Ir_{0.2}O₃/CNCs, the catalyzed GDE was subjected to repeated sequences of oxygen reduction (0.5 h), resting (1 h), oxygen evolution (0.5 h), and resting (1 h) for intermittent life time that. Each cycle lasted 3 h and the average voltage in the oxygen reduction and evolution steps was measured. The results are shown in Fig. 5.16. For the oxygen evolution reactions, the voltages drifted lower initially but moved up steadily at a rate of 1.59 mVcycle⁻¹. At the 70th cycle, the voltage was 2.08 V. Similarly, the voltages in the oxygen reduction reactions exhibited a gradual reduction upon cycling. The slopes of the voltage declines were 0.61 mVcycle⁻¹ in the first stage (0–40 cycles) and 4.24 mVcycle⁻¹ in the second stage (40–70 cycles). At the 70th cycle, the voltage was still 0.97 V. Since CO₂-filtered air was used, the effect of carbonation-induced electrode damage could be ruled out. We speculated that the undesirable electrolyte flooding contributed partially to the performance degradations because in our case only a thin layer of catalysts was deposited on the surface of the GDEs. In addition, it is recognized that oxidation of the carbon supports during the oxygen evolution reaction might have led to the gradual loss of catalytic abilities [69,70].

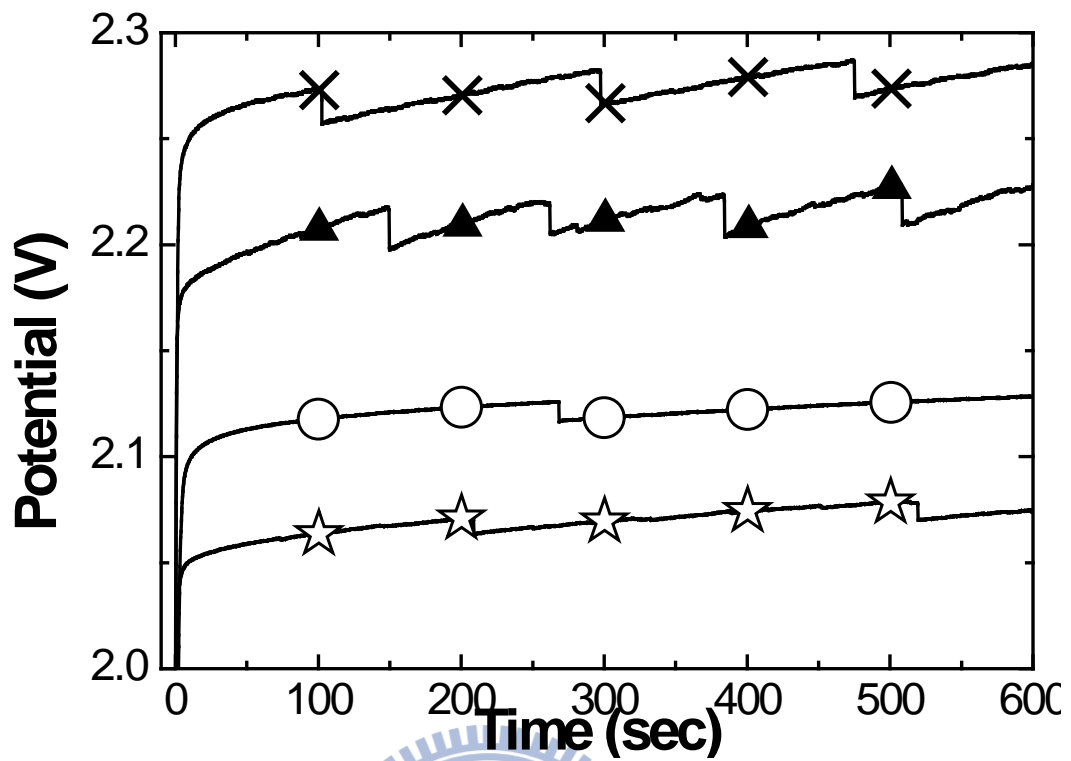


Figure 5.15 Oxygen evolution galvanostatic curves for ACP-derived $\text{La}_{0.6}\text{Ca}_{0.4}\text{Co}_{0.8}\text{Ir}_{0.2}\text{O}_3/\text{CNCs}$ at current densities of 50 mAcm^{-2} (\star) and 100 mAcm^{-2} (\circ), as well as $\text{La}_{0.6}\text{Ca}_{0.4}\text{CoO}_3/\text{CNCs}$ at current densities of 50 mAcm^{-2} (\blacktriangle) and 100 mAcm^{-2} (\times).

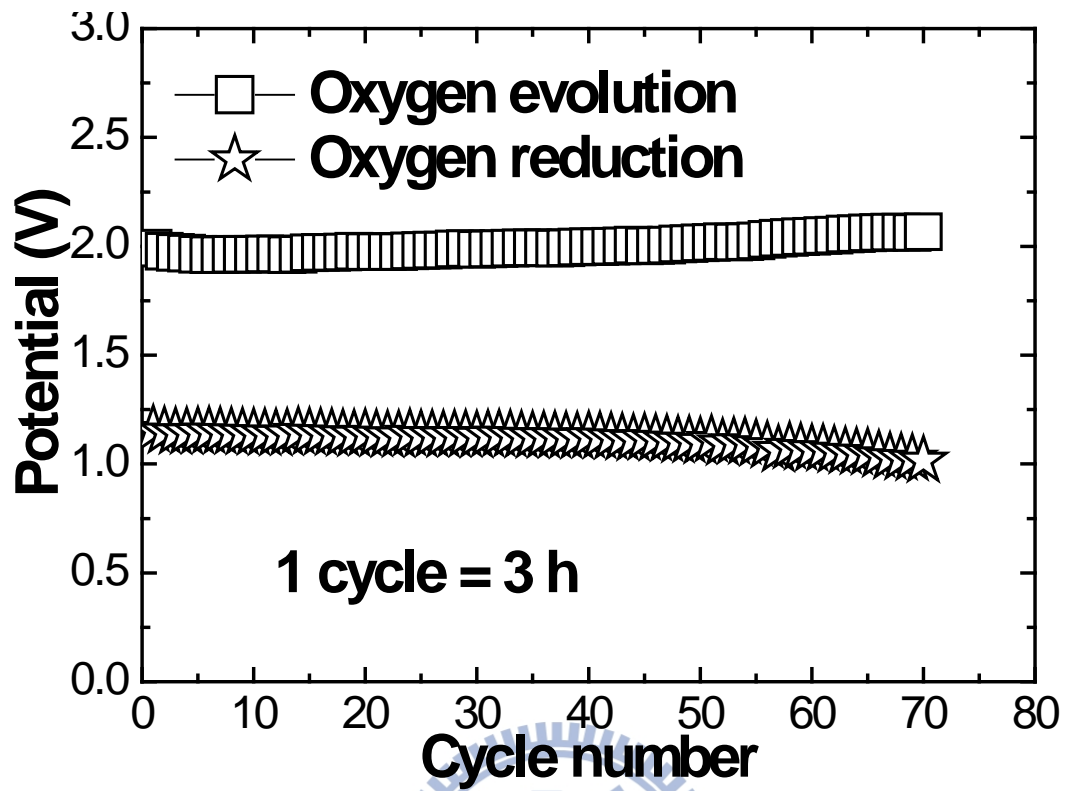


Figure 5.16 The cycle life performance for the ACP-derived $\text{La}_{0.6}\text{Ca}_{0.4}\text{Co}_{0.8}\text{Ir}_{0.2}\text{O}_3/\text{CNCs}$ -catalyzed GDE.

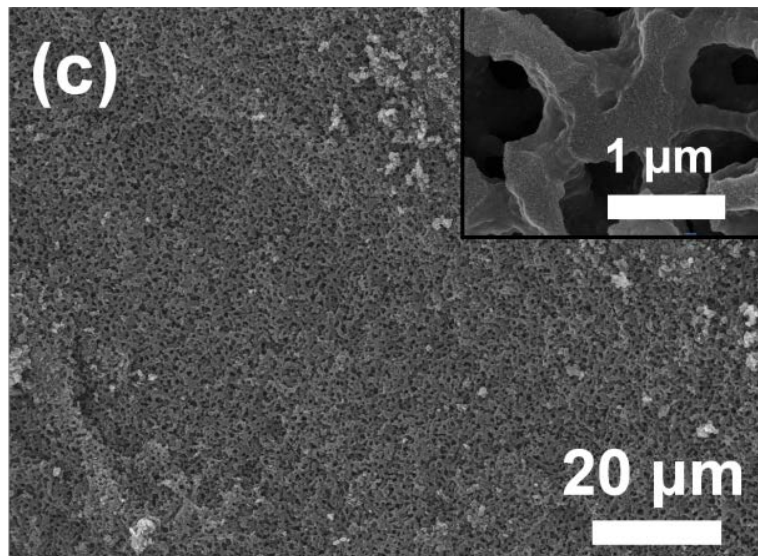
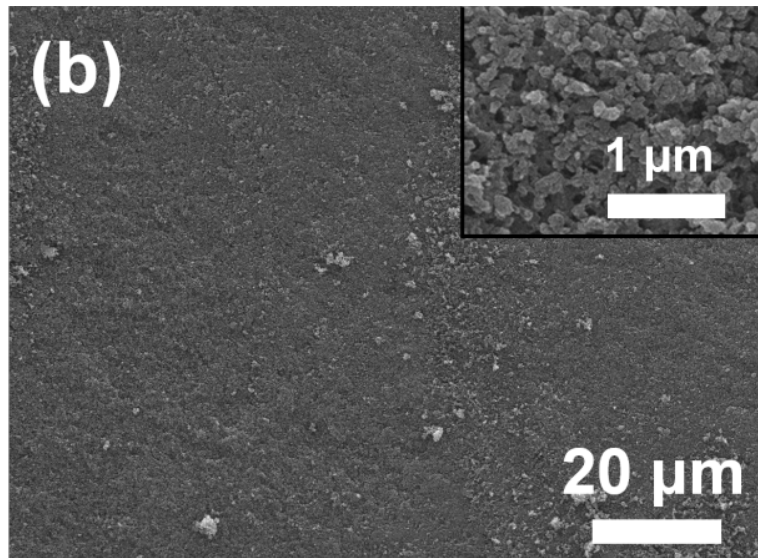
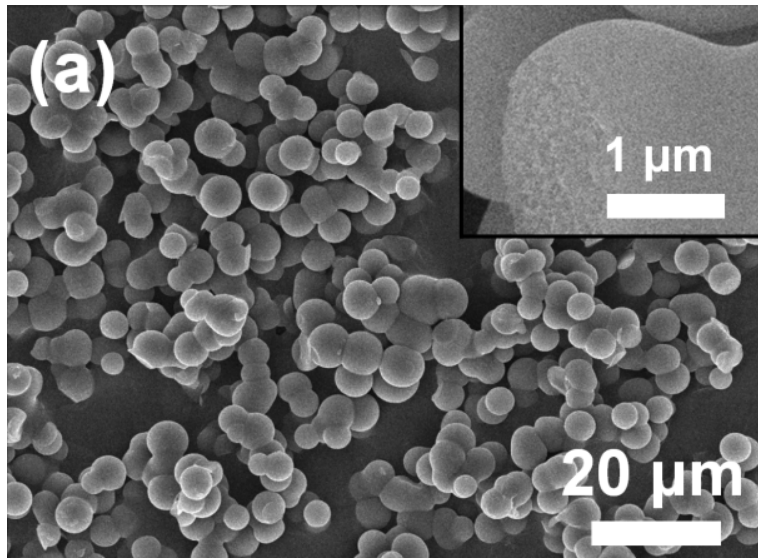
Chapter 6 Synthesis of Large Surface Area Carbon Ambient Gels for Electrochemical Double Layer Capacitors

6.1 Structural characterizations

Previously, in the preparation of R-F derived carbon aerogels, the R/C ratios were in between 50 and 1500, and a catalyst such as sodium carbonate (NaCO_3) was used [123]. It is because a high R/C ratio enables the formation of large colloidal particles with limited contacts among them, and a base catalyst promotes a wider pore size distributions [122,123]. However, the concentration of catalyst with such formula extremely low and it is rather difficult to initiate the condensation reaction. Therefore, we inferred that a lower R/C ratio of 5 or 10 might be beneficial because the concentrated precursors allow an intimate structure with relatively narrower pore size distribution. In addition, we selected an acidic catalyst because Al-Muhtaseb *et al.* and Elkhataat *et al.* reported that in an acidic solution, the condensation reaction took less time to complete and finer interconnected mesopores were produced afterwards [122,123].

Representative SEM images for GA, GB, GC, and GD samples are presented in Fig. 6.1(a)-(d). Sample GA (shown in Fig. 6.1(a) and its inset) revealed uniform spherical carbons with diameter in 7-10 μm . These spherical carbons are in contact with each other in a string-of-pearls pattern. Since the sample was synthesized with relatively lower precursor concentrations, the condensation reaction took place slowly

and resulted in larger primary particles. Similar results were observed by Scherdei *et al.* who observed the formation of spherical particles at lower precursor concentrations [151]. In SEM image of sample GB shown in Fig. 6.1(b), once the precursor concentrations were increased (while the R/C ratio was kept at 5:1), many small irregularly-shaped carbon particles (50-500 nm in size) connecting to each other was observed. During sol-gel reaction, a higher precursor concentration often leads to faster condensation and stronger cross-linking among primary particles. As a result, sample GB exhibited a foam-like microstructure comprised of mostly smaller primary carbon particles compared to those of sample GA. Fig. 6.1(c) shows the morphology of sample GC, in which a reduced catalyst amount was used while the precursor concentration was identical to that of sample GB. Similar to that of Fig. 6.1(b), a foam-like microstructure with primary carbon particles in 50-100 nm size was observed. Moreover, a higher magnification picture, sample GC revealed larger internal pores with moderate sintering among primary carbon particles in sample GC. We speculated that due to a reduced catalyst loading, there were fewer nucleation sites for the sol-gel reaction so that the resulting cross-linking was suppressed. Morphology for sample GD is shown in Fig. 6.1(d). Since the difference between samples GC and GD was the treatment for CO₂ activation, their morphologies are hence quite similar as the CO₂ etching effect induces the micropores on the carbon surface and those micropores were not readily observed by SEM.



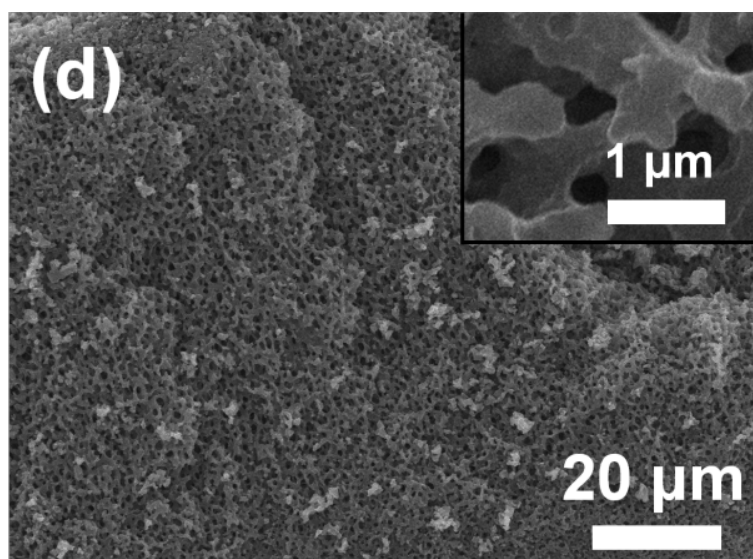


Figure 6.1 SEM images for sample (a) GA, (b) GB, (b) GC, and (d) GD.

The pores of carbon ambient gels can be classified as micropores (<2 nm), mesopores (2-50 nm), and macropores (>50 nm). Their relative amounts could be estimated by nitrogen adsorption and desorption isotherms as shown in Fig. 6.2. Interestingly, samples GA, GB, GC, and GD exhibited a type I behavior, indicating the predominant presence of micropores. Relevant pore properties including BET surface area (S_{BET}), micropore surface area (S_{Micro}), external surface area (S_{Ext}), average pore diameter, micropore volume (V_{Micro}), and total pore volume (V_{Pore}) are provided in Table 6.1. Despite their notable difference in SEM morphology, samples GA and GB exhibited similar V_{micro} , implying that the R/C ratio and CO_2 activation were responsible for micropore formation. Remarkably, at identical R/C ratio of 10, sample GC possessed four times larger V_{micro} over that of sample GD. Moreover, the S_{Ext} for sample GC increased considerably as well. It is noted that the S_{Ext} represents the sum of macropores and mesopores. According to Fig. 6.1, the morphologies for sample GC and sample GD were quite similar, and hence their macropore volumes were likely to be close. Therefore, the large S_{Ext} for sample GC was attributed to the

formation of abundant mesopores and micropores during CO₂ activation. This was confirmed by the burn-off ratio listed in Table 6.1. With CO₂ activation, the samples suffered from weight loss of 95-96%. In contrast, without CO₂ activation, sample GD retained 11.7 % weight after pyrolysis. Our experimental results provide clear evidences for CO₂ activation that effectively etches the carbon surface, resulting in the presence of excess micropores and mesopores. It is worthy to note that the surface area for sample GC was estimated at 3419 m²g⁻¹, a value that is significantly larger than typical high surface area carbons like activated carbons or Black Pearl 2000 (BP2000). In previous studies of RF-derived samples, the largest surface area reported was 3125 m²g⁻¹ from a carbon aerogel [152]. In our case, we were able to surpass that value by combining improved formula, solvent exchange, and CO₂ activation simultaneously.

Table 6.1 Relevant parameters for the pore properties determined by nitrogen adsorption and desorption isotherms from GA, GB, GC, and GD, respectively.

| | GA | GB | GC | GD |
|---|--------|--------|--------|-------|
| V _{Pore} (cm ³ g ⁻¹) | 0.99 | 0.86 | 1.36 | 0.23 |
| V _{Micro} (cm ³ g ⁻¹) | 0.42 | 0.40 | 0.76 | 0.18 |
| S _{BET} ^a (m ² g ⁻¹) | 2293.9 | 2016.6 | 3418.6 | 449.1 |
| S _{Micro} (m ² g ⁻¹) | 1009 | 928.8 | 1987.4 | 338.4 |
| S _{Ext} ^b (m ² g ⁻¹) | 1284.9 | 1087.7 | 1431.2 | 110.7 |
| D _p (Å) | 13.8 | 12.2 | 18.5 | 11.1 |
| S _{Ext} ratio ^c (%) | 56 | 53.9 | 40.9 | 24.7 |

^a S_{BET} = S_{Micro} + S_{Ext}.

^b S_{Ext} is the surface area including mesopores and macropores.

^c S_{Ext} ratio = S_{Ext}/S_{BET}.

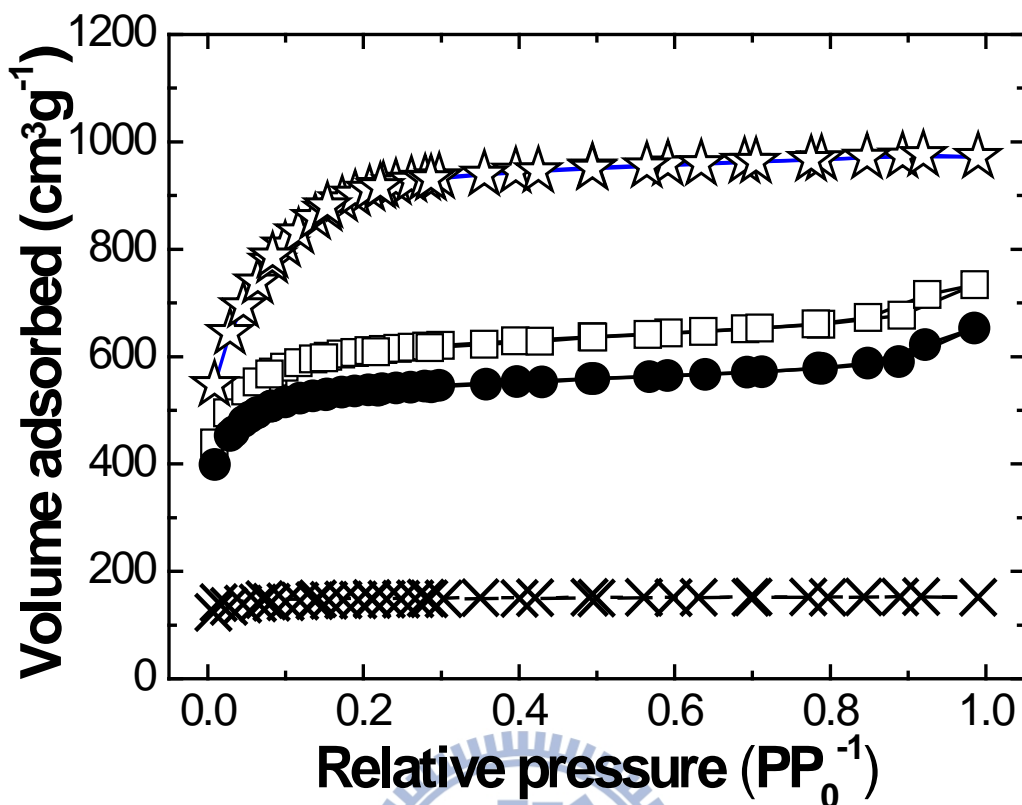


Figure 6.2 N₂ adsorption/desorption isotherms of sample GA (□), GB (●), GC (☆), and GD (×).

To evaluate the bond status for our samples, Raman analysis was conducted and the results are displayed in Fig. 6.3. The Raman spectra revealed distinct peaks near 1340 cm⁻¹ and 1580 cm⁻¹, respectively. According to previous study [153], the first peak at 1340 cm⁻¹ (D-band) is attributed to the sp³ hybridized bonding which is associated with disordered or amorphous carbon phase, while the graphitic component in sp² arrangement accounts for the second peak at 1580 cm⁻¹ (G-band). Hence, the degree of graphitization, or crystallinity for the carbon ambient gels, could be determined by the ratio of integrated from intensities D and G bands (I_D/I_G). For an ideal graphitic structure, the I_D/I_G ratio is expected to be zero as a singular I_G peak is present. In our case, the I_D/I_G ratios were 1.93, 1.86, 2.05, and 1.78 for samples GA, GB, GC, and GD, respectively. These values suggested that the structures for the

carbon ambient gels were poorly ordered with substantial numbers of defects. Moreover, the I_D/I_G ratios for those samples undergoing CO_2 activation were consistently larger than that of sample GD. This pattern confirmed that the CO_2 activation was able to destroy sp^2 bonding, exposing a larger surface upon pore formation.

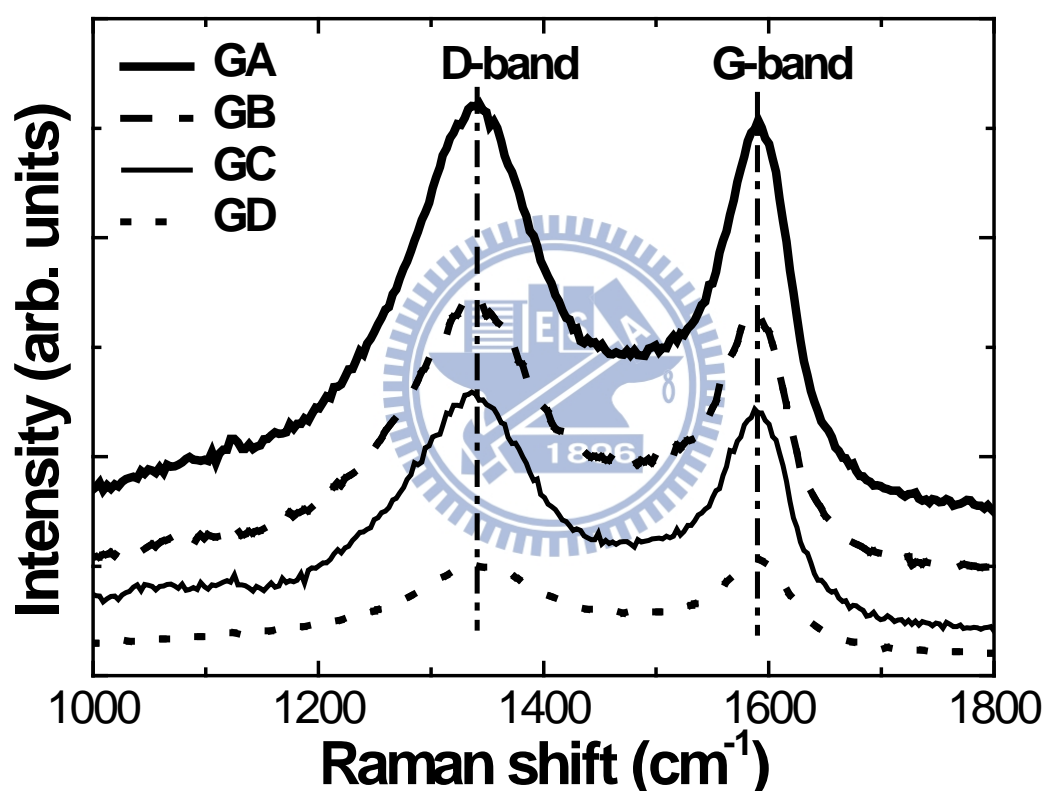


Figure 6.3 Raman spectra for sample GA, GB, GC, and GD.

6.2 Electrochemical characterizations

Since binder was not used in the TCE for electrochemical analysis, the determination of intrinsic capacitive behaviors for the carbon ambient gels was

feasible especially only a small amount of sample was necessary to fill the electrode cavity. Fig. 6.4 shows the representative CV profiles for sample GC at potential windows of 0-0.6, 0-0.8, and 0-1 V, respectively, along with the response from an empty TCE. As shown, the TCE itself revealed negligible currents in both forward and backward scans. In contrast, the carbon ambient gels exhibited quasi-rectangular responses typical of EDLCs [154]. At voltage approaching 1 V, there appeared moderate electrolysis which engendered an apparent current rise. Notably, the presence of functional groups on the carbon ambient gels was rather subdued as additional redox peaks were not observed in 0.2-0.6 V. It is known that the specific capacitance could be estimated from the CV profiles by the equation listed below,

$$C_s = \frac{Q}{w\Delta E} = \frac{\int i_c dt}{w\Delta E} \quad (5-1)$$

where C_s , Q , w , ΔE , and i_c are the specific capacitance (Fg^{-1}), coulombs of discharge, sample weight, CV potential window, and cathodic current density, respectively. Table 6.2 lists the specific capacitance for the carbon ambient gels at various potential windows along with commercially available carbon blacks such as Vulcan XC72R (XC72R), BP2000, and Active Carbon (AC1100). The C_s for those commercial carbon blacks were determined by a TCE in identical test conditions and their values were reported in our previous work [109].

Table 6.2 Values of specific capacitance (Fg^{-1}) calculated from CV profiles in various potential windows at 20 mVs^{-1} scan rate.

| | GA | GB | GC | GD | XC72 ^a | BP2000 ^a | AC1100 ^a |
|---------|------|-------|-------|------|-------------------|---------------------|---------------------|
| 0-0.6 V | 55.8 | 98 | 168.4 | 31 | 16.7 | 78 | 75 |
| 0-0.8 V | 69.3 | 115.2 | 183.4 | 33 | 18.7 | 94 | 80.8 |
| 0-1 V | 84.5 | 150.4 | 209.9 | 38.3 | 25.7 | 130.3 | 88 |

^a these values were reported in reference 109.

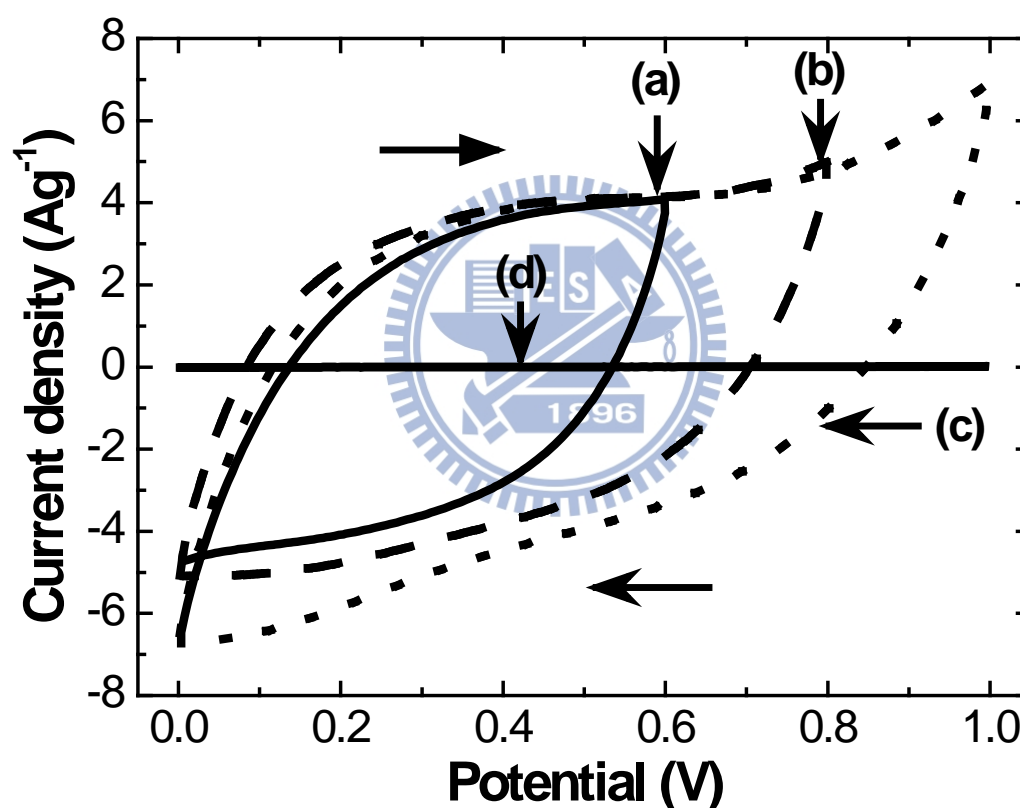


Figure 6.4 CV profiles at 20 mVs^{-1} from sample GC in potential windows of (a) 0-0.6 V, (b) 0-0.8 V, (c) 0-1 V, and (d) empty TCE of 0-1 V, respectively.

Among commercial carbon blacks, the BP2000 is known to possess a large surface area due to its fine particle size and consequently, its C_S is considerably larger than that of XC72R (130.3 vs. 25.7 Fg^{-1}). Remarkably, the carbon ambient gels of GB

and GC exhibited even larger C_S values of 150.4 and 209.9 Fg^{-1} , respectively. These values, to our knowledge, are comparable to the C_S s derived from other large-surface-area nanostructured carbons reported in previously [155-159]. For example, Weng *et al.* fabricated active carbons with a surface area of $2860 \text{ m}^2\text{g}^{-1}$ and obtained a C_S of 130 Fg^{-1} [155]. Similar results were reported by Rufford *et al.* whose active carbons of 1788 and $2019 \text{ m}^2\text{g}^{-1}$ were synthesized and their C_S were 300 and 368 Fg^{-1} , respectively [156,157]. According to Table 3.1, sample GD was prepared with the identical formulation to sample GC but the CO_2 activation step was replaced by Ar heat treatment. Without the CO_2 etching effect, sample GD possessed a substantially low V_{micro} and as a result, its C_S was merely 38.3 Fg^{-1} .

It is known that the CV profiles for a double layer capacitor are affected by the scan rate imposed during CV measurements. The relation for a capacitive current from a double layer capacitor is as follows,

$$i_c = \nu C_d [1 - \exp(-t/R_s C_d)] \quad (5-2)$$

where ν is the scan rate, R_s is the electrolyte resistance, t is the time, and C_d is the capacitance (Fg^{-1}). Hence, the current rises quickly and reaches a plateau in a short time for a true capacitor. In addition, an increasing scan rate allows a larger current plateau. Fig. 6.5 displays the representative CV profiles of sample GC at various scan rates in a potential window of 0-1 V. The CV profiles exhibited rectangular shapes at scan rates of 5 and 10 mVs^{-1} , as expected for a typical double layer capacitor [160]. Apparently, once the scan rate exceeded to 20 mVs^{-1} , the CV curves gradually distorted. This distortion was attributed to the compromised diffusion within the porous structure that rendered a progressively slower capacitance upon faster scan

rate [129]. The C_S is also a function of CV scan rate since at a sufficiently fast scan rate, some micropores become inaccessible due to diffusion limitation, and thus cease to contribute to the capacitive current. Hence, the largest C_S is always recorded at the lowest scan rate where ions adsorption and desorption are allowed in available free surface and internal pores. Table 6.3 provides the C_S at different scan rates for the carbon ambient gels and commercial carbon blacks. For the carbon ambient gels except sample GA, they exhibited capacitance retention characteristics similar to those of XC72, BP2000, and AC1100. We can thus reasonably assumed that the carbon ambient gels contained pores that were properly sized so access by ions was moderate at fast scan rate.

Table 6.3 Values of specific capacitance (Fg^{-1}) calculated from CV profiles at various scan rates in potential window of 0-1 V.

| mVs^{-1} | GA | GB | GC | GD | XC72 ^a | BP2000 ^a | AC1100 ^a |
|------------|-------|-------|-------|------|-------------------|---------------------|---------------------|
| 5 (a) | 193.7 | 214.9 | 312.3 | 56.9 | 32.03 | 169.76 | 128.48 |
| 10 | 132.4 | 183.1 | 266.2 | 47.2 | 29.52 | 152.97 | 111.19 |
| 20 | 84.5 | 150.4 | 209.9 | 38.3 | 25.68 | 130.32 | 88 |
| 50 (b) | 38.6 | 122.6 | 132.6 | 27.3 | 23.28 | 95.51 | 51.28 |
| (b/a) (%) | 19.9 | 57.1 | 42.5 | 48.8 | 72.68 | 56.26 | 39.91 |

^a these values were reported in reference 109.

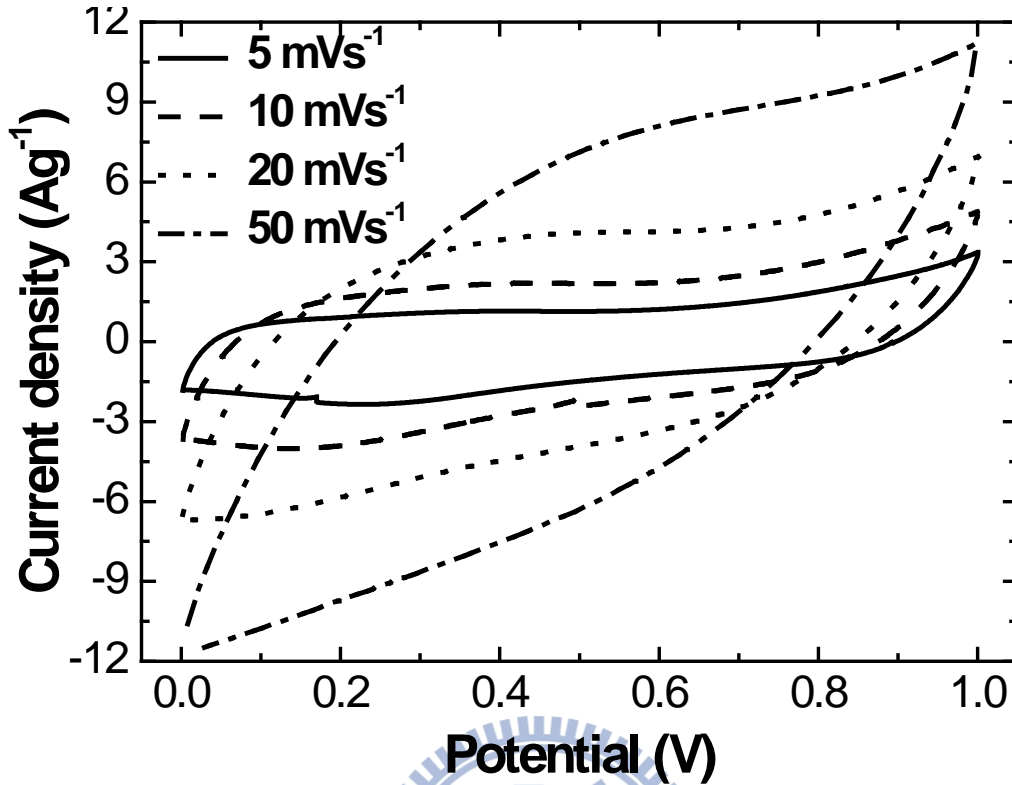


Figure 6.5 CV profiles for sample GC in potential window of 0-1 V at scan rates of 5, 10, 20, and 50 mVs⁻¹, respectively.

Fig. 6.6 provides the CRC responses at $\pm 1 \text{ Ag}^{-1}$ for the carbon ambient gels. It is known that the C_S can be estimated by following equation [109],

$$C_S = \frac{i_c}{w \times \left| \frac{dE}{dt} \right|} \approx \frac{Q}{w \times \Delta E} \quad (5-3)$$

where $\frac{dE}{dt}$ is the slope for discharging curve. In addition, during current reversal, there is a sudden voltage drop (iR loss) whose magnitude is proportional to the electrical resistance of carbon ambient gel, TCE, and electrolyte. Values for the C_S and iR loss are listed in Table 6.4. Sample GD exhibited the lowest voltage drop, suggesting its smallest electrical resistance. This might be attributed to its intimate interconnected structure and surface integrity. On the other hand, sample GA

exhibited the largest voltage drop which was likely caused by the finite contact areas among primary carbon particles that circumvented electron transports (see Fig. 6.1(a)). In addition, all carbon ambient gels except GD possessed C_S larger than 200 Fg^{-1} , indicating that accessible surface area, as well as suitable micropores and mesopores structure were produced after CO_2 activation.

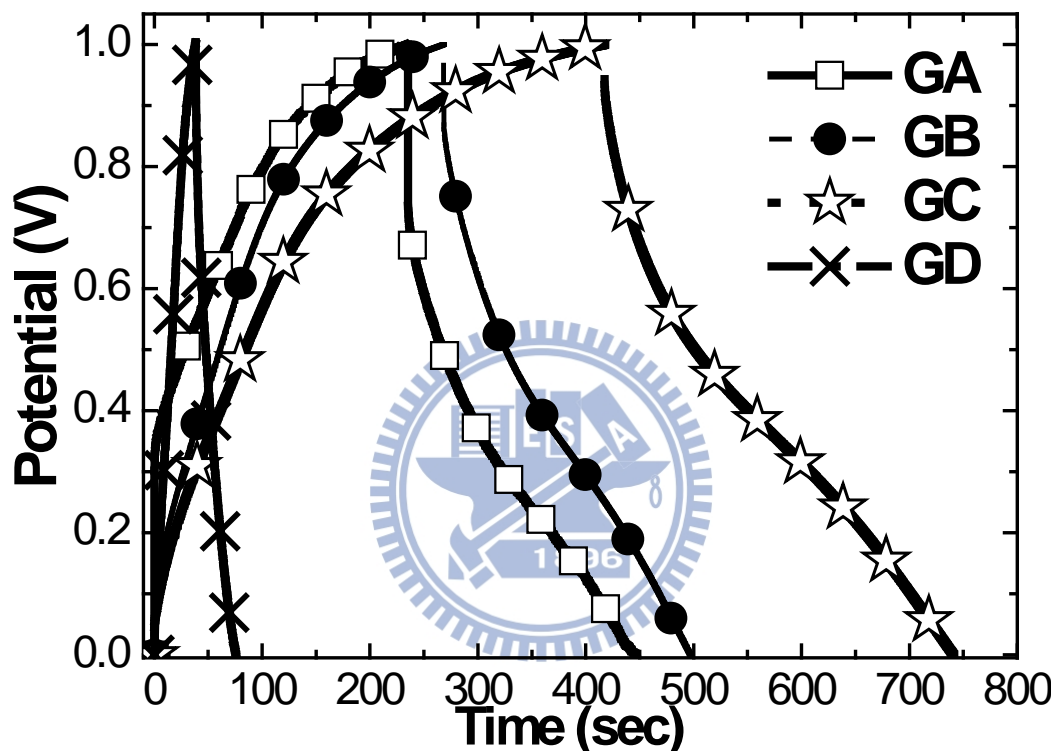


Figure 6.6 CRC curves at $\pm 1 \text{ Ag}^{-1}$ in potential window of 0-1 V for sample GA, GB, GC, and GD, respectively.

Table 6.4 Relevant parameters determined from the CRC measurements at $\pm 1 \text{ Ag}^{-1}$ in potential window of 0-1 V.

| | GA | GB | GC | GD |
|------------------------------------|-------|-------|-------|-------|
| Q © | 236.3 | 269.2 | 418.6 | 39.60 |
| E ⁺ (V) | 1.00 | 1.00 | 1.00 | 1.00 |
| E ⁻ (V) | 0.736 | 0.869 | 0.935 | 0.944 |
| <i>iR</i> drop (mV) | 264 | 131 | 65 | 56 |
| C _S (Fg ⁻¹) | 213.2 | 229.4 | 324.8 | 34.7 |

It is noted that the CRC scan always leads to a higher C_S as opposed to that obtained by CV scans. Since the CRC method is conducted at a fixed potential window with a constant current density, it hence allows a sufficient time for ion adsorption and desorption. In contrast, the C_S determined by CV scans is achieved by varying current so the kinetics for ion diffusion in the porous structure is limited. In principle, the capacitance obtained at slow scan rate during CV scans should approach to of CRC method. In our measurements, indeed, the C_S of CRC at 1 Ag⁻¹ was indeed close to the C_S of from the CV at a scan rate of 5 mVs⁻¹.

To evaluate the life time performance for the carbon ambient gels, we carried out the cyclic CRC experiments between 0 and 1 V at $\pm 1 \text{ Ag}^{-1}$. The resulting capacitance variation over 3000 cycles are shown in Fig. 6.7, along with that of BP2000 for comparison purpose. The life time testing, it was found that the capacitances decreases smaller with increasing cycles, a fact that was possibly associated with detachment of individual carbon particles during prolonged cycling. We speculated that without binder, electrolyte inundation in the TCE cavity inevitably affects the packing density and local environments of carbon particles. As a result, the amount of

carbon particles responsible for the capacitive responses decreases with time. This undesired effect was the worst in sample GA (with a capacity loss of 63%) since its SEM image indicated there is limited contact in between carbon particles and thus results in poor electrical conductivity and packing density. In contrast, sample GB exhibited the best capacitance retention with a moderate capacity loss of 13%. Sample GC showed a capacitance loss of 27% despite its *IR* loss was the smallest as listed in Table 6.4. Nevertheless, the value of GC was still significantly better than 41% of BP2000. Hence, we concluded that except sample GA, the carbon ambient gels retained reasonable EDLCs behaviors comparable or even better than that of BP2000.

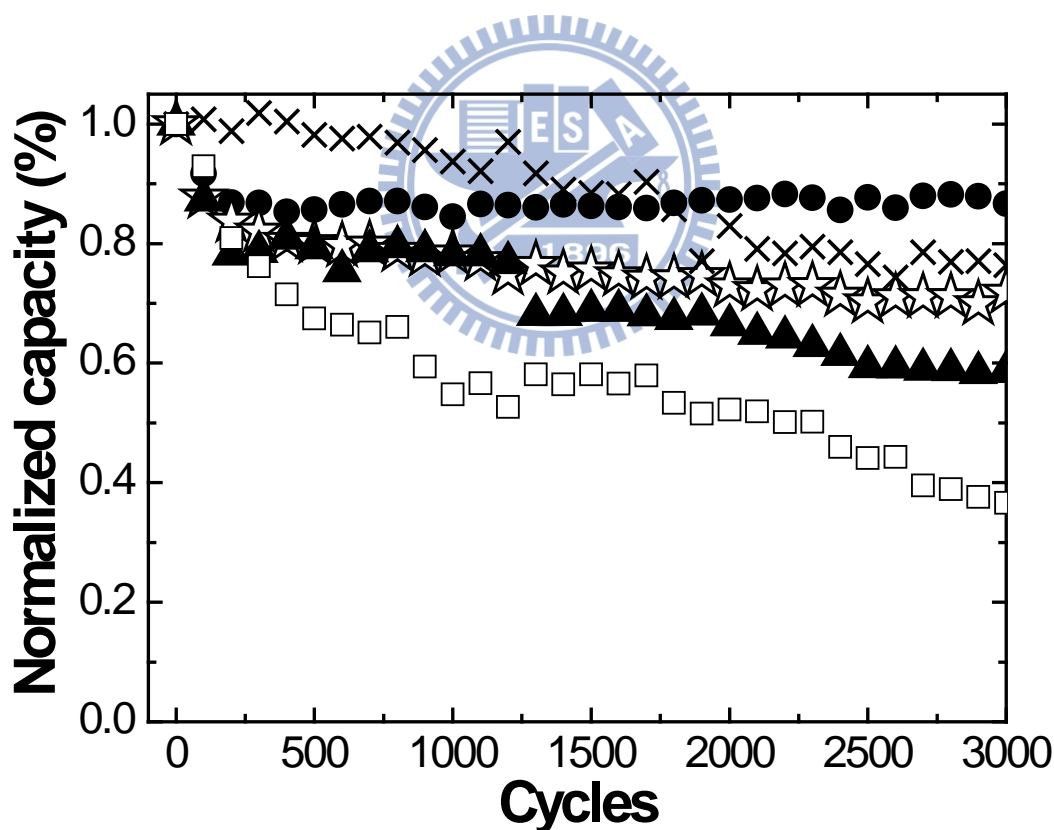
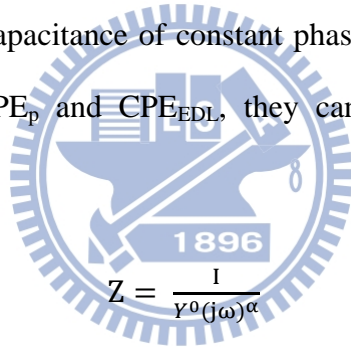


Figure 6.7 Variation of specific capacitance for sample GA(□), GB(●), GC(☆), GD(×), and BP2000 (▲) obtained from CRC measurements in potential window of 0-1 V at $\pm 1 \text{Ag}^{-1}$ for 3000 cycles.

Impedance analysis is a powerful technique to examine the interfacial phenomenon occurring in the ambient gels during capacitive responses. Fig. 6.8(a) shows the Nyquist plots for samples GA, GB, and GC over the frequency regime of 0.1-20 kHz. Apparently, the impedance spectra consist of a semi-circle at high frequency and a Warburg diffusion at low frequency. The enlarged spectra at high frequency regime is shown in Fig. 6.8(b) and the equivalent circuit model for fitting the impedance spectra is provided in Fig. 6.8(c). As shown, the equivalent circuit includes elements of R_s (ohmic resistance from electrolyte, carbon particles, and TCE), R_{CT} (resistance from faradaic charge transfer reaction), CPE_p (capacitance of constant phase element for faradaic charge transfer reaction), W (Warburg impedance), and CPE_{EDL} (capacitance of constant phase element for electrochemical double layer). For both CPE_p and CPE_{EDL} , they can be derived from following equation [161]:



$$Z = \frac{1}{Y^0(j\omega)^\alpha} \quad (5-4)$$

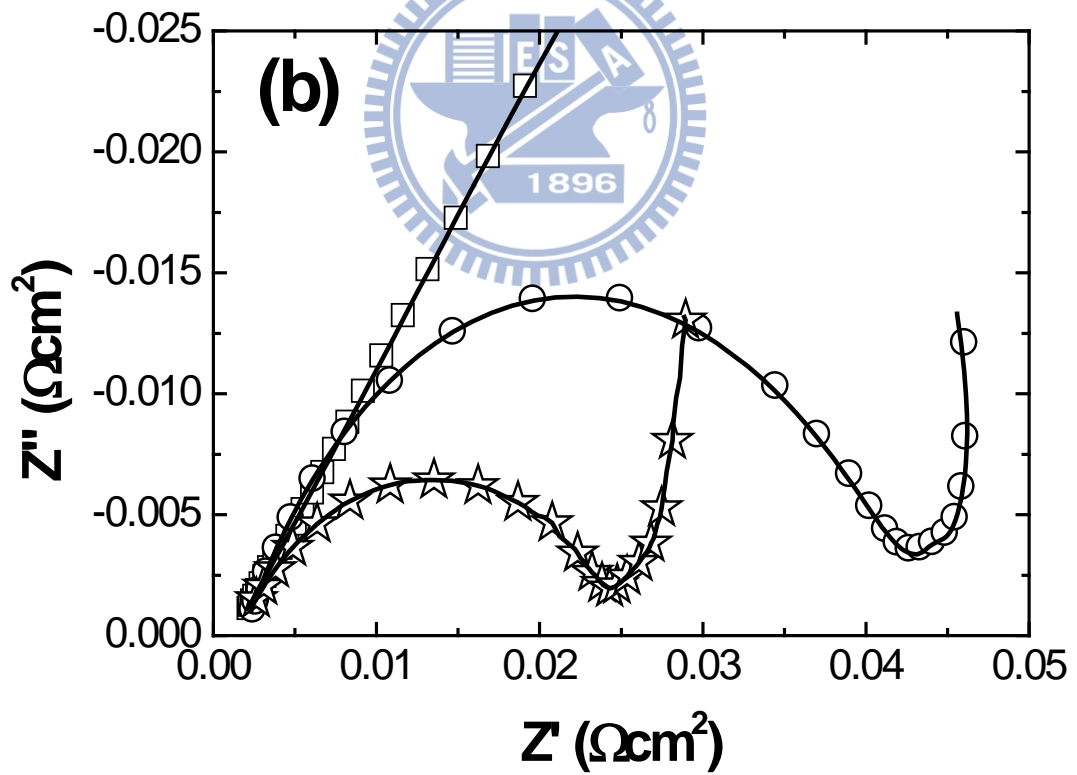
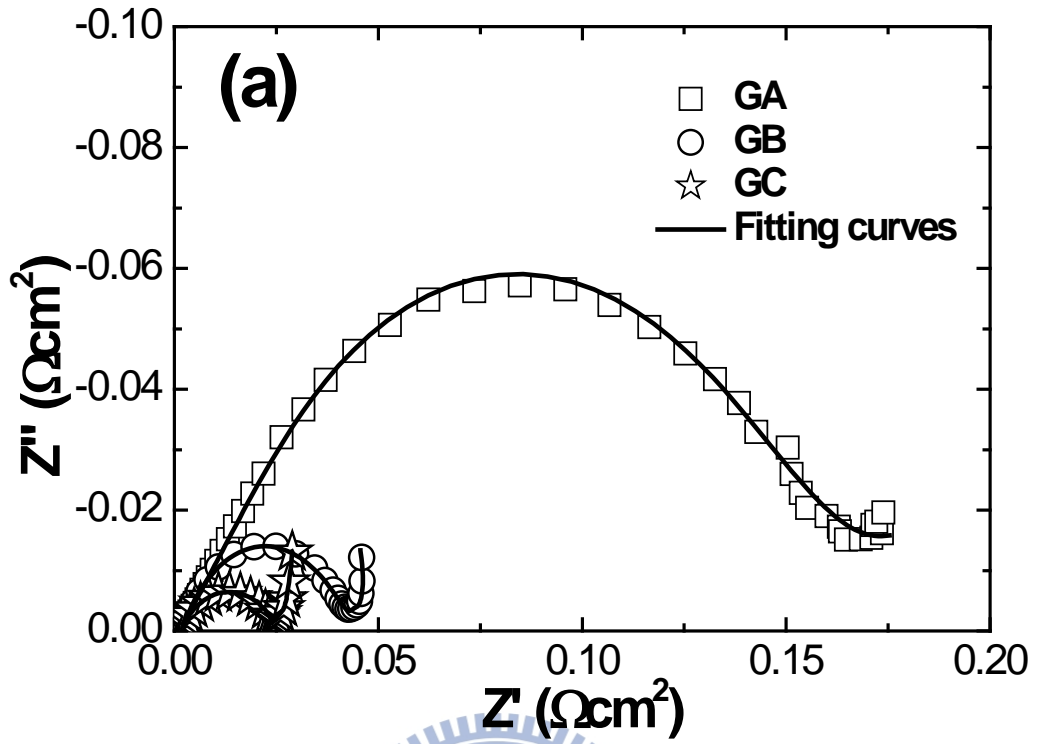
where Z , Y^0 , j , ω , and α are impedance, capacitance of associated element, imaginary unit, angular frequency ($\omega = 2\pi f$) of the AC signal, and a dimensionless parameter for fitting purpose ($\alpha = 0$ for a pure resistor and $\alpha = 1$ for an ideal parallel plate capacitor). In practice, the α is between 0 and 1, and its exact value reflects the porous nature of the active material [162].

Table 6.5 presents the fitting results with relevant parameters clearly identified. As listed, the R_s values were rather subdued confirming the conductive nature for the carbon ambient gels. The CPE_p-Y^0 , $W-Y^0$, and $CPE_{EDL}-Y^0$ indicate the capacitive components for CPE_p , Warburg impedance, and CPE_{EDL} , respectively. Among these

samples, the q values for CPE_p were consistently below 1, which was expected for a porous electrode. In addition, the q values of Warburg impedance for sample GB and GC were less than 1, a fact attributed to the limited diffusion in porous carbons. For sample GA, its q value of Warburg impedance was undetermined because the Warburg diffusion occurring at the low frequency regime was not clearly defined. It is possible that a lower frequency AC signal is necessary to clarify the diffusion effect. As for the CPE_{EDL} , interestingly, sample GC revealed a q value of 1, suggesting its response was close to an ideal capacitor.

Table 6.5 Parameters from fitting impedance spectra obtained at the open circuit voltage

| | | GA | GB | GC |
|------------------------------|-------------------------|---------|-----------|---------|
| R_s (Ωg^{-1}) | | 0.00115 | 0.00181 | 0.00151 |
| CPE_p | Y^0 (Fg^{-1}) | 1.113 | 0.228 | 0.281 |
| | q | 0.553 | 0.707 | 0.642 |
| R_{CT} (Ωg^{-1}) | | 0.0954 | 0.0339 | 0.0215 |
| W | R (Ωg^{-1}) | - | 0.0019204 | 0.00462 |
| | Y^0 (Fg^{-1}) | - | 0.69332 | 0.839 |
| | q | - | 0.741 | 0.417 |
| CPE_{EDL} | Y^0 (Fg^{-1}) | 77.230 | 117.300 | 130.300 |
| | q | 0.428 | 0.552 | 1.000 |



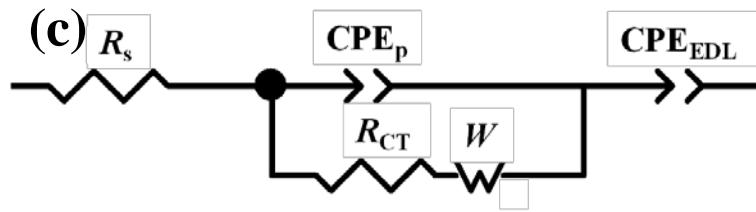


Figure 6.8 (a) Nyquist plots for sample GA, GB, and GC at the open circuit voltage in frequency range of 0.1-20 kHz, as well as (b) the enlarged spectra at high frequency regime. (c) is the equivalent circuit model used to fit the impedance spectra.



Chapter 7 Conclusions and Future Work

7.1 Conclusions

Stoichiometric $\text{La}_{0.6}\text{Ca}_{0.4}\text{Co}_{1-x}\text{Ru}_x\text{O}_3$ powders were prepared *via* ACP and SRR routes. The XRD analysis identified the perovskite structure of $\text{La}_{0.6}\text{Ca}_{0.4}\text{CoO}_3$, indicating the successful incorporation of Ru^{3+} at the Co^{3+} sites. The SEM image exhibited a foam-like microstructure with a specific surface area of $11.6 \text{ m}^2\text{g}^{-1}$ in ACP-derived $\text{La}_{0.6}\text{Ca}_{0.4}\text{Co}_{0.8}\text{Ru}_{0.2}\text{O}_3$. On the other hand, the surface areas of SSR-derived $\text{La}_{0.6}\text{Ca}_{0.4}\text{Co}_{1-x}\text{Ru}_x\text{O}_3$ ($x=0\sim 1$) were between 7 and $10 \text{ m}^2\text{g}^{-1}$. In the H_2O_2 decomposition test, ACP-derived $\text{La}_{0.6}\text{Ca}_{0.4}\text{Co}_{0.8}\text{Ru}_{0.2}\text{O}_3$ exhibited a higher decomposition rate as opposed to that of $\text{La}_{0.6}\text{Ca}_{0.4}\text{CoO}_3$. Consistent behaviors were observed during the ORR I-V polarization measurements. Impedance spectra indicated a smaller R_{CT} for ACP-derived $\text{La}_{0.6}\text{Ca}_{0.4}\text{Co}_{0.8}\text{Ru}_{0.2}\text{O}_3/\text{BP2000}$. Both the galvanostatic profiles and the life time performance indicated an impressive ORR ability for ACP-derived $\text{La}_{0.6}\text{Ca}_{0.4}\text{Co}_{0.8}\text{Ru}_{0.2}\text{O}_3/\text{BP2000}$. Furthermore, it is demonstrated that the Ru-doped $\text{La}_{0.6}\text{Ca}_{0.4}\text{CoO}_3$ show a superior behavior than the undoped ones for oxygen evolution and reduction catalytic abilities. Among the compositions studied, the SSR-derived $\text{La}_{0.6}\text{Ca}_{0.4}\text{Co}_{0.4}\text{Ru}_{0.6}\text{O}_3$ exhibited the best bi-functional catalytic abilities.


Mechanical alloying process was adopted to prepare $\text{La}_{0.6}\text{Ca}_{0.4}\text{CoIr}_{0.25}\text{O}_{3.5-\delta}$ from mixtures of $\text{La}_{0.6}\text{Ca}_{0.4}\text{CoO}_3$ and IrO_2 . Powders of $\text{La}_{0.6}\text{Ca}_{0.4}\text{Co}_{0.8}\text{Ir}_{0.2}\text{O}_3$ were synthesized by amorphous citrate precursor method. XRD results on the resulting

powders confirmed successful formation of perovskite phase. The SEM images demonstrated $\text{La}_{0.6}\text{Ca}_{0.4}\text{CoIr}_{0.25}\text{O}_{3.5-\delta}$ particles in irregular shape between 300-500 nm in size while the SEM images of ACP-derived $\text{La}_{0.6}\text{Ca}_{0.4}\text{Co}_{0.8}\text{Ir}_{0.2}\text{O}_3$ revealed a foam-like microstructure with numerous sub-micron pores. In electrochemical characterizations, the $\text{La}_{0.6}\text{Ca}_{0.4}\text{CoIr}_{0.25}\text{O}_{3.5-\delta}$ and ACP-derived $\text{La}_{0.6}\text{Ca}_{0.4}\text{Co}_{0.8}\text{Ir}_{0.2}\text{O}_3/\text{CNCs}$ exhibited improved performances over those of $\text{La}_{0.6}\text{Ca}_{0.4}\text{CoO}_3/\text{CNCs}$ and IrO_2/CNCs for both charging and discharging polarizations. For Ir doping of $\text{La}_{0.6}\text{Ca}_{0.4}\text{CoO}_3$ perovskite prepared by these two GDEs, ACP-derived $\text{La}_{0.6}\text{Ca}_{0.4}\text{Co}_{0.8}\text{Ir}_{0.2}\text{O}_3/\text{CNCs}$ produces the powders with highest catalytic ability. In addition, the resulting discharge I-V curves of ACP-derived $\text{La}_{0.6}\text{Ca}_{0.4}\text{Co}_{0.8}\text{Ir}_{0.2}\text{O}_3/\text{BP2000}$ and $\text{La}_{0.6}\text{Ca}_{0.4}\text{Co}_{0.8}\text{Ir}_{0.2}\text{O}_3/\text{CNCs}$ show the similar electrochemical activity. Similar behaviors were observed by galvanostatic measurements for oxygen reduction and evolution reactions. In life time determinations, where repeated cycling of oxygen reduction/resting/oxygen evolution/resting was imposed, ACP-derived $\text{La}_{0.6}\text{Ca}_{0.4}\text{Co}_{0.8}\text{Ir}_{0.2}\text{O}_3/\text{CNCs}$ demonstrated stable and sustainable performances with moderate degradation. Our results provided conclusive evidence that the doping of Ir in the perovskite structure of $\text{La}_{0.6}\text{Ca}_{0.4}\text{CoO}_3$ significantly enhances its bi-functional abilities in the alkaline electrolyte.

In term of electrochemical substrate, we synthesized carbon ambient gels *via* a condensation reaction of resorcinol ® and formaldehyde (F), followed by solvent exchange, pyrolysis, and CO_2 activation. The carbon ambient gels experienced negligible structural contraction during solvent removal and as a result, possessing excessive surface area with a large number of micropores and mesopores. By

selecting suitable combination of precursors and acidic catalyst, we were able to produce a porous carbon structure whose surface area reached as high as $3418 \text{ m}^2\text{g}^{-1}$. Image from SEM confirmed its foam-like morphology with moderate sintering among primary carbon particles. CV scans and CRC methods indicated C_5 and life time behaviors are comparable or even better than those of BP2000 in identical test conditions. In contrast, without CO_2 activation, the carbon ambient gel displayed a similar morphology but its surface area was reduced considerably to $449 \text{ m}^2\text{g}^{-1}$. Due to lack of sufficient micropores and mesopores, the resulting C_5 and the life time behavior were inferior to samples with CO_2 activation.

7.2 Future works



Future work of the bi-functional catalysts will focus on developing and improving performance for alkaline electrolyte system such as increasing surface area, minimization of the particle sizes, and doping noble metals. The surface area and particle sizes of catalyst are critical due to the determination of catalytic active sites. Generally speaking, metal oxide perovskite (two-electron route) has relatively lower conductivity and catalytic ability than those of noble metals (four-electron route) for ORR. We can dope little noble metals such as Pt, Pd, Rh, and Ag in perovskite for enhancing the catalytic ability. Therefore, the modification would be a practical way to increase the catalytic activity of perovskite for oxygen reduction and evolution.

Regarding of the carbon ambient gels research, we have recently studied the use of CO_2 treatment for surface activation. In the future work, it will be necessary to introduce metal oxides, such as RuO_2 , V_2O_5 , MnO_2 , etc., into the carbon ambient gels

to enhance the C_S of this metal oxide/carbon ambient gel nanocomposites. It is expected that the combination of metal oxides and carbon ambient gels can take the advantages of both the high pseudocapacitance of metal oxides and the stable double-layer capacitance of carbon ambient gels, which might result in much enhanced supercapacitance performance. In our study, we found that the carbon ambient gels high porosity in the structure, implying that the carbon ambient gels have huge voids in the structure. It is interesting that adding metallic ion into carbon ambient gels during sol-gel condensation process could result in well dispersed metal oxide/carbon ambient gel nanocomposites.



References

- [1] Service RF. The Hydrogen Backlash. *Science*. 2004;305:958-61.
- [2] Hamakawa Y. *Thin Film Solar Cells*. New York: Springer-Verlag; 2003.
- [3] O'Hayre R, Cha SW, Colella W, Prinz FB. *Fuel Cell Fundamentals*, New York: John Wiley & Sons; 2006.
- [4] Kennedy D. The Hydrogen Solution. *Science*. 2004;305:917.
- [5] Brown N. Solar Junction Breaks Concentrated Solar World Record with 43.5% Efficiency, <http://cleantechnica.com/2011/04/19/solar-junction-breaks-concentrated-solar-world-record-with-43-5-efficiency/>.
- [6] Conway BE. *Electrochemical Supercapacitors-Scientific Fundamentals and Technological Applications*. New York: Kluwer Academic-Plenum Publishers; 1999.
- [7] Simon P, Gogotsi Y. Materials for Electrochemical Capacitors. *Nature Materials* 2008;7:845-54.
- [8] Steele BCH, Heinzel A. Materials for Fuel-cell Technologies. *Nature*. 2001;414:345-52.
- [9] Arai H, Muller S, Haas O. AC Impedance Analysis of Bifunctional Air Electrodes for Metal-Air Batteries. *Journal of The Electrochemical Society*. 2000;147:3584-91.
- [10] McLean GF, Niet T, Prince-Richard S, Djilali N. An Assessment of Alkaline Fuel Cell Technology. *International Journal of Hydrogen Energy*. 2002;27:507-26.

- [11] <http://en.wikipedia.org/wiki/Perovskite>.
- [12] Jörissen L. Bifunctional Oxygen/Air Electrodes. *Journal of Power Sources*. 2006;155(1):23-32.
- [13] Zhang HM, Teraoka Y, Yamazoe N. Preparation of Perovskite-Type Oxides with Large Surface Area by Citrate Process. *Chemistry Letters* 1987;16:665-8.
- [14] Chang YM, Wu PW, Wu CY, Hsieh YF, Chen J-Y. Mechanical Alloying Preparation of $\text{La}_{0.6}\text{Ca}_{0.4}\text{CoIr}_{0.25}\text{O}_{3.5-\delta}$ as a Bifunctional Electrocatalyst in Alkaline Electrolyte. *Electrochemical and Solid-State Letters*. 2008;11(4):B47-B50.
- [15] Chang YM, Wu PW, Wu CY, Hsieh YC. Synthesis of $\text{La}_{0.6}\text{Ca}_{0.4}\text{Co}_{0.8}\text{Ir}_{0.2}\text{O}_3$ Perovskite for Bi-Functional Catalysis in an Alkaline Electrolyte. *Journal of Power Sources*. 2009;189(2):1003-7.
- [16] Prakash J, Joachin H. Electrocatalytic Activity of Ruthenium for Oxygen Reduction in Alkaline Solution. *Electrochimica Acta*. 2000;45(14):2289-96.
- [17] Adžić RR, Anastasijević NA, Dimitrijević ZM. Oxygen Reduction on Ruthenium Electrode Modified by Foreign Metal Adsorbates. *Journal of The Electrochemical Society*. 1984;131(11):2730-1.
- [18] Neburchilov V, Wang H, Martin JJ, Qu W. A Review on Air Cathodes for Zinc-Air Fuel Cells. *Journal of Power Sources*. 2010;195(5):1271-91.
- [19] Kinumoto T, Takai K, Iriyama Y, Abe T, Inaba M, Ogumi Z. Stability of Pt-Catalyzed Highly Oriented Pyrolytic Graphite Against Hydrogen Peroxide in Acid Solution. *Journal of The Electrochemical Society*. 2006;153(1):A58-63.

- [20] Stamenkovic VR, Fowler B, Mun BS, Wang G, Ross PN, Lucas CA, et al. Improved Oxygen Reduction Activity on Pt₃Ni(111) via Increased Surface Site Availability. *Science*. 2007 January 26, 2007;315(5811):493-7.
- [21] Meng H, Shen PK. Novel Pt-free Catalyst for Oxygen Electroreduction. *Electrochemistry Communications*. 2006;8(4):588-94.
- [22] Bashyam R, Zelenay P. A Class of Non-Precious Metal Composite Catalysts for Fuel Cells. *Nature*. 2006;443(7107):63-6.
- [23] Wu CY, Wu PW, Lin P, Li YY, Lin YM. Silver-Carbon Nanocapsule Electrocatalyst for Oxygen Reduction Reaction. *Journal of The Electrochemical Society*. 2007;154(10):B1059-62.
- [24] Kinoshita K. *Electrochemical Oxygen Technology*. John Wiley & Sons. New York (1992).
- [25] Li X, Hsing IM. The Effect of the Pt Deposition Method and the Support on Pt Dispersion on Carbon Nanotubes. *Electrochimica Acta*. 2006;51:5250-8.
- [26] Lafuente E, Muñoz E, Benito AM, Maser WK, Martínez MT, Alcaide F, et al. Single-Walled Carbon Nanotube-Supported Platinum Nanoparticles as Fuel Cell Electrocatalysts. *Journal of Materials Research*, 2006;21:2841-6.
- [27] Ding J, Chan K-Y, Ren J, Xiao F-s. Platinum and Platinum–Ruthenium Nanoparticles Supported on Ordered Mesoporous Carbon and Their Electrocatalytic Performance for Fuel Cell Reactions. *Electrochimica Acta*. 2005;50:3131-41.
- [28] Gamburgzev S, Petrov K, Appleby AJ. Silver–Carbon Electrocatalyst for Air

- Cathodes in Alkaline Fuel Cells. *Journal of Applied Electrochemistry*. 2002;32:805-9.
- [29] Chou KS, Ren CY. Synthesis of Nanosized Silver Particles by Chemical Reduction Method. *Materials Chemistry and Physics*. 2000;64:241-6.
- [30] Tang Z, Liu S, Dong S, Wang E. Electrochemical Synthesis of Ag Nanoparticles on Functional Carbon Surfaces. *Journal of Electroanalytical Chemistry*. 2001;502:146-51.
- [31] Ardizzone S, Falciola M, Trasatti S. Effect of the Nature of the Precursor on the Electrocatalytic Properties of Thermally Prepared Ruthenium Oxide. *Journal of The Electrochemical Society*. 1989;136:1545-50.
- [32] Bagotzky VS, Shumilova NA, Khrushcheva EI. Electrochemical Oxygen Reduction on Oxide Catalysts. *Electrochimica Acta*. 1976;21:919-24.
- [33] Wei ZD, Huang WZ, Zhang ST, Tan J. Induced Effect of Mn_3O_4 on Formation of MnO_2 Crystals Favourable to Catalysis of Oxygen Reduction. *Journal of Applied Electrochemistry*. 2000;30:1133-6.
- [34] Tiwari SK, Chartier P, Singh RN. Preparation of Perovskite-Type Oxides of Cobalt by the Malic Acid Aided Process and Their Electrocatalytic Surface Properties in Relation to Oxygen Evolution. *Journal of The Electrochemical Society*. 1995;142:148-53.
- [35] Müller S, Striebel K, Haas O. $La_{0.6}Ca_{0.4}CoO_3$: a Stable and Powerful Catalyst for Bifunctional Air Electrodes. *Electrochimica Acta*. 1994;39:1661-8.
- [36] Wu NL, Liu WR, Su SJ. Effect of Oxygenation on Electrocatalysis of

$\text{La}_{0.6}\text{Ca}_{0.4}\text{CoO}_{3-x}$ in Bifunctional Air Electrode. *Electrochimica Acta*. 2003;48:1567-71.

[37] Lee CK, Striebel KA, McLarnon FR, Cairns EJ. Thermal Treatment of $\text{La}_{0.6}\text{Ca}_{0.4}\text{CoO}_3$ Perovskites for Bifunctional Air Electrodes. *Journal of The Electrochemical Society*. 1997;144:3801-6.

[38] Bockris JOM, Otagawa T. The Electrocatalysis of Oxygen Evolution on Perovskites. *Journal of The Electrochemical Society*. 1984;131:290-302.

[39] Ponce J, Rehspringer JL, Poillerat G, Gautier JL. Electrochemical Study of Nickel–Aluminium–Manganese Spinel $\text{Ni}_x\text{Al}_{1-x}\text{Mn}_2\text{O}_4$. Electrocatalytical Properties for the Oxygen Evolution Reaction and Oxygen Reduction Reaction in Alkaline Media. *Electrochimica Acta*. 2001;46:3373-80.

[40] Sugawara M, Ohno M, Matsuki K. Oxygen Reduction Catalysis of Mn-Co Spinel Oxides on a Graphite Electrode in Alkaline Solution. *Journal of Materials Chemistry*. 1997;7:833-6.

[41] El Baydi M, Tiwari SK, Singh RN, Rehspringer JL, Chartier P, Koenig JF, et al. High Specific Surface Area Nickel Mixed Oxide Powders LaNiO_3 (Perovskite) and NiCo_2O_4 (Spinel) via Sol-Gel Type Routes for Oxygen Electrocatalysis in Alkaline Media. *Journal of Solid State Chemistry*. 1995;116:157-69.

[42] Zhao F, Harnisch F, Schröder U, Scholz F, Bogdanoff P, Herrmann I. Application of Pyrolysed Iron (II) Phthalocyanine and CoTMPP Based Oxygen Reduction Catalysts as Cathode Materials in Microbial Fuel Cells. *Electrochemistry Communications*. 2005;7:1405-10.

- [43] Wang B. Recent Development of Non-Platinum Catalysts for Oxygen Reduction Reaction. *Journal of Power Sources*. 2005;152:1-15.
- [44] Lee YN, Lago RM, Fierro JLG, González J. Hydrogen Peroxide Decomposition Over $\text{Ln}_{1-x}\text{A}_x\text{MnO}_3$ (Ln = La or Nd and A = K or Sr) Perovskites. *Applied Catalysis A: General*. 2001;215(1-2):245-56.
- [45] Jiang SP, Lin ZG, Tseung ACC. Homogeneous and Heterogeneous Catalytic Reactions in Cobalt Oxide/Graphite Air Electrodes. *Journal of The Electrochemical Society*. 1990;137(3):759-64.
- [46] Falcón H, Carbonio RE, Fierro JLG. Correlation of Oxidation States in $\text{LaFe}_x\text{Ni}_{1-x}\text{O}_{3+\delta}$ Oxides with Catalytic Activity for H_2O_2 Decomposition. *Journal of Catalysis*. 2001;203(2):264-72.
- [47] da Silva PS, Schmitz EPS, Spinelli A, Garcia JR. Electrodeposition of Zn and Zn–Mn Alloy Coatings from an Electrolytic Bath Prepared by Recovery of Exhausted Zinc–Carbon Batteries. *Journal of Power Sources*. 2012;210:116-21.
- [48] Kinoshita K. *Electrochemical Oxygen Technology*. John Wiley & Sons. New York (1992).
- [49] Simner SP, Anderson MD, Coleman JE, Stevenson JW. Performance of a Novel $\text{La}(\text{Sr})\text{Fe}(\text{Co})\text{O}_3\text{–Ag}$ SOFC Cathode. *Journal of Power Sources*. 2006;161:115-22.
- [50] El-Deab MS, Awad MI, Mohammad AM, Ohsaka T. Enhanced Water Electrolysis: Electrocatalytic Generation of Oxygen Gas at Manganese Oxide Nanorods Modified Electrodes. *Electrochemistry Communications*. 2007;9:2082-7.

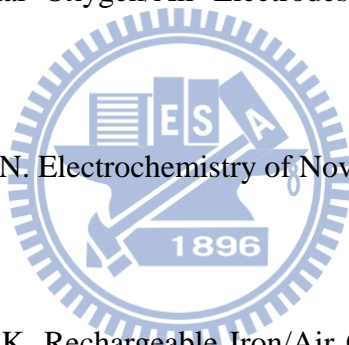
[51] Weidenkaff A, Ebbinghaus SG, Lippert T. $\text{Ln}_{1-x}\text{A}_x\text{CoO}_3$ (Ln = Er, La; A = Ca, Sr)/Carbon Nanotube Composite Materials Applied for Rechargeable Zn/Air Batteries. *Chemistry of Materials*. 2002;14:1797-805.

[52] Chartouni D, Kuriyama N, Kiyobayashi T, Chen J. Air–Metal Hydride Secondary Battery with Long Cycle Life. *Journal of Alloys and Compounds*. 2002;330–332:765-70.

[53] Swette L, Giner J. Oxygen Electrodes for Rechargeable Alkaline Fuel Cells. *Journal of Power Sources*. 1988;22:399-408.

[54] Jörissen L. Bifunctional Oxygen/Air Electrodes. *Journal of Power Sources*. 2006;155:23-32.

[55] Lipkowski J and Ross PN. *Electrochemistry of Novel Materials*. New York: VCH Publishers Inc; 1994.



[56] Kannan AM, Shukla AK. Rechargeable Iron/Air Cells Employing Bifunctional Oxygen Electrodes of Oxide Pyrochlores. *Journal of Power Sources*. 1991;35:113-21.

[57] Bursell M, Pirjamali M, Kiros Y. $\text{La}_{0.6}\text{Ca}_{0.4}\text{CoO}_3$, $\text{La}_{0.1}\text{Ca}_{0.9}\text{MnO}_3$ and LaNiO_3 as Bifunctional Oxygen Electrodes. *Electrochimica Acta*. 2002;47:1651-60.

[58] Hermann V, Dutriat D, Müller S, Comninellis C. Mechanistic Studies of Oxygen Reduction at $\text{La}_{0.6}\text{Ca}_{0.4}\text{CoO}_3$ -Activated Carbon Electrodes in a Channel Flow Cell. *Electrochimica Acta*. 2000;46:365-72.

[59] Mota N, Álvarez-Galván MC, Al-Zahrani SM, Navarro RM, Fierro JLG. Diesel Fuel Reforming Over Catalysts Derived from $\text{LaCo}_{1-x}\text{Ru}_x\text{O}_3$ Perovskites with High

Ru Loading. *International Journal of Hydrogen Energy*. 2012;37:7056-66.

[60] Hjalmarsson P, Sjøgaard M, Mogensen M. Defect Structure, Electronic Conductivity and Expansion of Properties of $(\text{La}_{1-x}\text{Sr}_x)\text{sCo}_{1-y}\text{Ni}_y\text{O}_{3-\delta}$. *Journal of Solid State Chemistry*. 2010;183:1853-62.

[61] Tiwari SK, Singh SP, Singh RN. Effects of Ni, Fe, Cu, and Cr Substitutions for Co in $\text{La}_{0.8}\text{S}_{0.2}\text{CoO}_3$ on Electrocatalytic Properties for Oxygen Evolution. *Journal of The Electrochemical Society*. 1996;143(5):1505-10.

[62] Haas O, Holzer F, Müller S, McBreen JM, Yang XQ, Sun X, et al. X-ray Absorption and Diffraction Studies of $\text{La}_{0.6}\text{Ca}_{0.4}\text{CoO}_3$ Perovskite, a Catalyst for Bifunctional Oxygen Electrodes. *Electrochimica Acta*. 2002;47:3211-7.

[63] Wang X, Sebastian PJ, Smit MA, Yang H, Gamboa SA. Studies on the Oxygen Reduction Catalyst for Zinc–Air Battery Electrode. *Journal of Power Sources*. 2003;124:278-84.

[64] De Pauli CP, Trasatti S. Composite Materials for Electrocatalysis of O_2 Evolution: $\text{IrO}_2+\text{SnO}_2$ in Acid Solution. *Journal of Electroanalytical Chemistry*. 2002;538–539:145-51.

[65] Guerrini E, Chen H, Trasatti S. Oxygen Evolution on Aged IrO_x/Ti Electrodes in Alkaline Solutions. *Journal of Solid State Electrochemistry*. 2007;11:939-45.

[66] Maja M, Orecchia C, Strano M, Tosco P, Vanni M. Effect of Structure of The Electrical Performance of Gas Diffusion Electrodes for Metal Air Batteries. *Electrochimica Acta*. 2000;46:423-32.

- [67] Litster S, McLean G. PEM fuel Cell Electrodes. *Journal of Power Sources*. 2004;130:61-76.
- [68] Tomantschger K, Findlay R, Hanson M, Kordesch K, Srinivasan S. Degradation Modes of Alkaline Fuel Cells and Their Components. *Journal of Power Sources*. 1992;39:21-41.
- [69] Staud N, Ross PN. The Corrosion of Carbon Black Anodes in Alkaline Electrolyte. *Journal of The Electrochemical Society*. 1986;133:1079-84.
- [70] Ross PN, Sattler M. The Corrosion of Carbon Black Anodes in Alkaline Electrolyte. *Journal of The Electrochemical Society*. 1988;135:1464-70.
- [71] Schmidt TJ, Gasteiger HA, Behm RJ. Rotating Disk Electrode Measurements on the CO Tolerance of a High-Surface Area Pt/Vulcan Carbon Fuel Cell Catalyst. *Journal of The Electrochemical Society*. 1999;146:1296-304.
- [72] Nadeau G, Song XY, Massé M, Guerfi A, Brisard G, Kinoshita K, et al. Effect of Heat-Treatment and Additives on the Particles and Carbon Fibers as Anodes for Lithium-Ion Batteries. *Journal of Power Sources*. 2002;108:86-96.
- [73] Yang R, Qiu X, Zhang H, Li J, Zhu W, Wang Z, et al. Monodispersed Hard Carbon Spherules as a Catalyst Support for the Electrooxidation of Methanol. *Carbon*. 2005;43:11-6.
- [74] Dicks AL. The Role of Carbon in Fuel Cells. *Journal of Power Sources*. 2006;156:128-41.
- [75] Iijima S. Helical Microtubules of Graphitic Carbon. *Nature*. 1991;354:56-58.

- [76] Liu TC, Li YY. Synthesis of Carbon Nanocapsules and Carbon Nanotubes by an Acetylene Flame Method. *Carbon*. 2006;44:2045-50.
- [77] Kongkanand A, Kuwabata S, Girishkumar G, Kamat P. Single-Wall Carbon Nanotubes Supported Platinum Nanoparticles with Improved Electrocatalytic Activity for Oxygen Reduction Reaction. *Langmuir*. 2006;22:2392-6.
- [78] Che G, Lakshmi BB, Fisher ER, Martin CR. Carbon Nanotubule Membranes for Electrochemical Energy Storage and Production. *Nature*. 1998;393:346-9.
- [79] Huang H, Zhang W, Li M, Gan Y, Chen J, Kuang Y. Carbon Nanotubes as a Secondary Support of a Catalyst Layer in a Gas Diffusion Electrode for Metal Air Batteries. *Journal of Colloid and Interface Science*. 2005;284:593-9.
- [80] Winter M, Brodd RJ. What Are Batteries, Fuel Cells, and Supercapacitors? *Chemical Reviews*. 2004;104:4245-70.
- [81] Tai Z, Yan X, Lang J, Xue Q. Enhancement of Capacitance Performance of Flexible Carbon Nanofiber Paper by Adding Graphene Nanosheets. *Journal of Power Sources*. 2012;199:373-8.
- [82] Pandolfo AG, Hollenkamp AF. Carbon Properties and Their Role in Supercapacitors. *Journal of Power Sources*. 2006;157:11-27.
- [83] An KH, Jeon KK, Heo JK, Lim SC, Bae DJ, Lee YH. High-Capacitance Supercapacitor Using a Nanocomposite Electrode of Single-Walled Carbon Nanotube and Polypyrrole. *Journal of The Electrochemical Society*. 2002;149:A1058-A62.
- [84] Conway BE. *Electrochemical Supercapacitors*, New York: Kluwer-Plenum Press;

1999.

[85] Kossyrev P. Carbon Black Supercapacitors Employing Thin Electrodes. *Journal of Power Sources*. 2012;201:347-52.

[86] Liu MC, Kong LB, Zhang P, Luo YC, Kang L. Porous Wood Carbon Monolith for High-Performance Supercapacitors. *Electrochimica Acta*. 2012;60:443-8.

[87] Lazzari M, Mastragostino M, Pandolfo AG, Ruiz V, Soavi F. Role of Carbon Porosity and Ion Size in the Development of Ionic Liquid Based Supercapacitors. *Journal of The Electrochemical Society*. 2011;158:A22-5.

[88] Jin SI, Deng HG, Zhan L, Qiao WM, Ling LC. Synthesis of 3D Hierarchical Porous Carbon as Electrode Material for Electric Double Layer Capacitors. *New Carbon Materials*. 2012;27:87-92.

[89] Pico F, Ibañez J, Lillo-Rodenas MA, Linares-Solano A, Rojas RM, Amarilla JM, et al. Understanding RuO₂·xH₂O/Carbon Nanofibre Composites as Supercapacitor Electrodes. *Journal of Power Sources*. 2008;176:417-25.

[90] Al Sakka M, Gualous H, Van Mierlo J, Culcu H. Thermal Modeling and Heat Management of Supercapacitor Modules for Vehicle Applications. *Journal of Power Sources*. 2009;194:581-7.

[91] Cericola D, Ruch PW, Kötz R, Novák P, Wokaun A. Simulation of a Supercapacitor/Li-ion Battery Hybrid for Pulsed Applications. *Journal of Power Sources*. 2010;195:2731-6.

[92] Hu CC, Chang KH, Lin MC, Wu YT. Design and Tailoring of the Nanotubular

Arrayed Architecture of Hydrus RuO₂ for Next Generation Supercapacitors. Nano Letters. 2006;6:2690-5.

[93] Sopčić S, Mandić Z, Inzelt G, Roković MK, Meštrović E. Ion dynamics in the pseudocapacitive reaction of hydrous ruthenium oxide. Effect of the Temperature Pre-treatment. Journal of Power Sources. 2011;196:4849-58.

[94] Song RY, Park JH, Sivakkumar SR, Kim SH, Ko JM, Park D-Y, et al. Supercapacitive Properties of Polyaniline/Nafion/hydrous RuO₂ Composite Electrodes. Journal of Power Sources. 2007;166:297-301.

[95] Rosario AV, Bulhões LOS, Pereira EC. Investigation of Pseudocapacitive Properties of RuO₂ Film Electrodes Prepared by Polymeric Precursor Method. Journal of Power Sources. 2006;158:795-800.

[96] Panić VV, Dekanski AB, Stevanović RM. Sol-gel Processed Thin-layer Ruthenium Oxide/Carbon Black Supercapacitors: A Revelation of the Energy Storage Issues. Journal of Power Sources. 2010;195:3969-76.

[97] Mayrand-Provencher L, Lin S, Lazzerini D, Rochefort D. Pyridinium-based Protic Ionic Liquids as Electrolytes for RuO₂ Electrochemical Capacitors. Journal of Power Sources. 2010;195:5114-21.

[98] Bonso JS, Rahy A, Perera SD, Nour N, Seitz O, Chabal YJ, et al. Exfoliated Graphite Nanoplatelets-V₂O₅ Nanotube Composite Electrodes for Supercapacitors. Journal of Power Sources. 2012;203:227-32.

[99] Jayalakshmi M, Rao MM, Venugopal N, Kim K-B. Hydrothermal Synthesis of SnO₂-V₂O₅ Mixed Oxide and Electrochemical Screening of Carbon Nano-tubes

(CNT), V_2O_5 , V_2O_5 -CNT, and SnO_2 - V_2O_5 -CNT electrodes for supercapacitor applications. *Journal of Power Sources*. 2007;166:578-83.

[100] Zhang YQ, Xia XH, Tu JP, Mai YJ, Shi SJ, Wang XL, et al. Self-assembled Synthesis of Hierarchically Porous NiO Film and Its Application for Electrochemical Capacitors. *Journal of Power Sources*. 2012;199:413-7.

[101] Lee MT, Tsai WT, Deng MJ, Cheng H-F, Sun IW, Chang JK. Pseudocapacitance of MnO_2 Originates from Reversible Insertion/desertion of Thiocyanate Anions Studied Using in Situ X-ray Absorption Spectroscopy in Ionic Liquid Electrolyte. *Journal of Power Sources*. 2010;195:919-22.

[102] Tang W, Hou YY, Wang XJ, Bai Y, Zhu YS, Sun H, et al. A Hybrid of MnO_2 Nanowires and MWCNTs as Cathode of Excellent Rate Capability for Supercapacitors. *Journal of Power Sources*. 2012;197:330-3.

[103] Qu QT, Shi Y, Tian S, Chen YH, Wu YP, Holze R. A New Cheap Asymmetric Aqueous Supercapacitor: Activated Carbon/ $NaMnO_2$. *Journal of Power Sources*. 2009;194:1222-5.

[104] Hung CJ, Hung JH, Lin P, Tseng TY. Electrophoretic Fabrication and Characterizations of Manganese Oxide/Carbon Nanotube Nanocomposite Pseudocapacitors. *Journal of The Electrochemical Society*. 2011;158:A942-7.

[105] Chang KH, Hu CC, Huang CM, Liu YL, Chang CI. Microwave-Assisted Hydrothermal Synthesis of Crystalline WO_3 - $WO_3 \cdot 0.5H_2O$ Mixtures for Pseudocapacitors of the Asymmetric Type. *Journal of Power Sources*. 2011;196:2387-92.

- [106] Sawangphruk M, Limtrakul J. Effects of Pore Diameters on The Pseudocapacitive Property of Three-Dimensionally Ordered Macroporous Manganese Oxide Electrodes. *Materials Letters*. 2012;68:230-3.
- [107] Kötz R, Carlen M. Principles and Applications of Electrochemical Capacitors. *Electrochimica Acta*. 2000;45:2483-98.
- [108] Appetecchi GB, Scaccia S, Tizzani C, Alessandrini F, Passerini S. Synthesis of Hydrophobic Ionic Liquids for Electrochemical Applications. *Journal of The Electrochemical Society*. 2006;153:A1685-91.
- [109] Wu CY, Wu PW, Lin P. Evaluation on Carbon Nanocapsules for Supercapacitors Using a Titanium Cavity Electrode. *Journal of Power Sources*. 2010;195:5122-9.
- [110] Zubizarreta L, Arenillas A, Pirard JP, Pis JJ, Job N. Tailoring the Textural Properties of Activated Carbon Xerogels by Chemical Activation with KOH. *Microporous and Mesoporous Materials*. 2008;115:480-90.
- [111] Galiński M, Lewandowski A, Stepniak I. Ionic liquids as electrolytes. *Electrochimica Acta*. 2006;51:5567-80.
- [112] Li Q, Liu F, Zhang L, Nelson BJ, Zhang S, Ma C, et al. In situ Construction of Potato Starch Based Carbon Nanofiber/Activated Carbon Hybrid Structure for High-Performance Electrical Double Layer Capacitor. *Journal of Power Sources*. 2012;207:199-204.
- [113] Ahmed J, Kim HJ, Kim S. Polyaniline Nanofiber/Carbon Black Composite as Oxygen Reduction Catalyst for Air Cathode Microbial Fuel Cells. *Journal of The Electrochemical Society*. 2012;159:B497-501.

[114] Haghghi B, Tabrizi MA. Direct Electron Transfer from Glucose Oxidase Immobilized on a Nano-Porous Glassy Carbon Electrode. *Electrochimica Acta*. 2011;56:10101-6.

[115] Casella IG, Di Fonzo DA. Anodic Electrodeposition of Cobalt Oxides from an Alkaline Bath Containing Co-Gluconate Complexes on Glassy Carbon. An Electroanalytical Investigation. *Electrochimica Acta*. 2011;56:7536-40

[116] Chng ELK, Pumera M. Nanographitic Impurities are Responsible for Electrocatalytic Activity of Carbon Nanotubes Towards Oxidation of Carbamazepine. *Electrochemistry Communications*. 2011;13:781-4.

[117] Chang YM, Hsieh YC, Wu PW. Improved Electrochemical Performances by Carbon Nanocapsules as an Electrocatalyst Support for Direct Methanol Fuel Cells. *Diamond and Related Materials*. 2009;18:501-4.

[118] Zou L, Lv R, Kang F, Gan L, Shen W. Preparation and Application of Bamboo-Like Carbon Nanotubes in Lithium Ion Batteries. *Journal of Power Sources*. 2008;184:566-9.

[119] Rooke J, Passos CdM, Chatenet M, Sescousse R, Budtova T, Berthon-Fabry S, et al. Synthesis and Properties of Platinum Nanocatalyst Supported on Cellulose-Based Carbon Aerogel for Applications in PEMFCs. *Journal of The Electrochemical Society*. 2011;158:B779-B89.

[120] Pekala RW. Low density, Resorcinol-Formaldehyde Aerogels. US patent No. 4873218 (1989).

[121] Liu B, Creager S. Carbon Xerogels as Pt Catalyst Supports for Polymer

Electrolyte Membrane Fuel-Cell Applications. *Journal of Power Sources*. 2010;195:1812-20.

[122] Al-Muhtaseb SA, Ritter JA. Preparation and Properties of Resorcinol-Formaldehyde Organic and Carbon Gels. *Advanced Materials*. 2003;15:101-14.

[123] Elkhatat AM, Al-Muhtaseb SA. Advances in Tailoring Resorcinol-Formaldehyde Organic and Carbon Gels. *Advanced Materials*. 2011;23:2887-903.

[124] Tian HY, Buckley CE, Paskevicius M, Sheppard DA, Wang SB, Webb CJ, et al. Nanoscale Cobalt Doped Carbon Aerogel: Microstructure and Isothermic Heat of Hydrogen adsorption. *International Journal of Hydrogen Energy*. 2011;36:10855-60.

[125] Inagaki M, Konno H, Tanaike O. Carbon Materials for Electrochemical Capacitors. *Journal of Power Sources*. 2010;195:7880-903.

[126] Lazzari M, Soavi F, Mastragostino M. High Voltage, Asymmetric EDLCs Based on Xerogel Carbon and Hydrophobic IL Electrolytes. *Journal of Power Sources*. 2008;178:490-6.

[127] Jespersen HT, Allermann K, Schneider I, Schaumburg K. Anti-Fouling Composition Comprising an Aerogel. US patent No. 20100269731 (2010).

[128] Fang B, Binder L. A modified Activated Carbon Aerogel for High-Energy Storage in Electric Double Layer Capacitors. *Journal of Power Sources*. 2006;163:616-22.

[129] Stoner BR, Glass JT. Carbon Nanostructures: A Morphological Classification for Charge Density Optimization. *Diamond and Related Materials*. 2012;23:130-4.

[130] Shimizu Y, Matsuda H, Miura N, Yamazoe N. Bi-functional Oxygen Electrode Using Large Surface Area Perovskite-type Oxide Catalyst for Rechargeable Metal-Air Batteries. *Chemistry Letters*. 1992;21(6):1033-6.

[131] Tiwari SK, Chartier P, Singh RN. Preparation of Perovskite-Type Oxides of Cobalt by the Malic Acid Aided Process and Their Electrocatalytic Surface Properties in Relation to Oxygen Evolution. *Journal of The Electrochemical Society*. 1995;142(1):148-53

[132] Teraoka Y, Kakebayashi H, Moriguchi I, Kagawa S. Hydroxy Acid-Aided Synthesis of Perovskite-Type Oxides of Cobalt and Manganese. *Chemistry Letters*. 1991;20(4):673-6.

[133] Merino NA, Barbero BP, Grange P, Cadús LE. $\text{La}_{1-x}\text{Ca}_x\text{CoO}_3$ Perovskite-Type Oxides: Preparation, Characterisation, Stability, and Catalytic Potentiality for the Total Oxidation of Propane. *Journal of Catalysis*. 2005;231(1):232-44.

[134] Müller S, Striebel K, Haas O. $\text{La}_{0.6}\text{Ca}_{0.4}\text{CoO}_3$: a Stable and Powerful Catalyst for Bifunctional Air Electrodes. *Electrochimica Acta*. 1994;39(11-12):1661-8.

[135] Chang YM, Hsieh YC, Wu PW, Lai CH, Chang TY. Enhancement of Bifunctional Catalysis by Ir Doping of $\text{La}_{0.6}\text{Ca}_{0.4}\text{CoO}_3$ Perovskites. *Materials Letters*. 2008;62(26):4220-2.

- [136] Chang YM, Hsieh YC, Wu PW. Improved Electrochemical Performances by Carbon Nanocapsules as an Electrocatalyst Support for Direct Methanol Fuel Cells. *Diamond and Related Materials*. 2009;18(2-3):501-4.
- [137] Krstajic NV, Jovic VD, Gajic-Krstajic L, Jovic BM, Antozzi AL, Martelli GN. Electrodeposition of Ni-Mo Alloy Coatings and Their Characterization as Cathodes for Hydrogen Evolution in Sodium Hydroxide Solution. *International Journal of Hydrogen Energy*. 2008;33(14):3676-87.
- [138] Arai H, Muller S, Haas O. AC Impedance Analysis of Bifunctional Air Electrodes for Metal-Air Batteries. *Journal of The Electrochemical Society*. 2000;147(10):3584-91.
- [139] Benjamin JS. Dispersion strengthened super-alloys by mechanical alloying. *Metall Trans*. 1970;1:2943-51.
- [140] Gaudet J, Tavares AC, Trasatti S, Guay D. Physicochemical Characterization of Mixed RuO₂-SnO₂ Solid Solutions. *Chem Mater*. 2005;17:1570-9.
- [141] Lalande G, Denis MC, Guay D, Dodelet JP, Schulz R. Structural and Surface Characterizations of Nanocrystalline Pt-Ru Alloys Prepared by High-Energy Ball-Milling. *Journal of Alloys and Compounds*. 1999;292:301-10.
- [142] Koch CC, Whittenberger JD. Mechanical Milling/Alloying of Intermetallics. *Intermetallics*. 1996;4:339-55.
- [143] Moreno KJ, Rodrigo RS, Fuentes AF. Direct Synthesis of A₂(Ti_(1-y)Zr_y)₂O₇ (A=Gd³⁺, Y³⁺) Solid Solutions by Ball Milling Constituent Oxides. *Journal of Alloys and Compounds*. 2005;390:230-5.

- [144] Wang JX, Su WH, Xu DP, He TM. Electrical Properties of Solid Solutions $\text{Ba}_{1.1}\text{Ce}_{1-x}\text{Eu}_x\text{O}_{3-\delta}$. *Journal of Alloys and Compounds*. 2006;421:45-8.
- [145] Tojo T, Zhang Q, Saito F. Mechanochemical Synthesis of Rutile-Type CrMO_4 (M=V, Sb) and Their Solid Solutions. *Journal of Solid State Chemistry*. 2006;179:433-7.
- [146] Figueroa S, Desimoni J, Rivas PC, Caracoche MC, De Sanctis O. Local Structures in the ZrO_2 -15 mol% Fe_2O_3 System Obtained by Ball Milling. *Journal of the American Ceramic Society*. 2006;89:3759-64.
- [147] Chen C, Zhang B, Liu D, Ge Z. Thermoelectric Properties of $\text{Cu}_y\text{Bi}_x\text{Sb}_{2-x-y}\text{Te}_3$ Alloys Fabricated by Mechanical Alloying and Spark Plasma Sintering. *Intermetallics*. 2012;25:131-5.
- [148] Mansuri I, Varshney D. Structure and Electrical Resistivity of $\text{La}_{1-x}\text{Ba}_x\text{MnO}_3$ ($0.25 \leq x \leq 0.35$) perovskites. *Journal of Alloys and Compounds*. 2012;513:256-65.
- [149] Kiuchi D, Matsushima H, Fukunaka Y, Kuribayashi K. Ohmic Resistance Measurement of Bubble Froth Layer in Water Electrolysis under Microgravity. *Journal of The Electrochemical Society*. 2006;153:E138-43.
- [150] Iida T, Matsushima H, Fukunaka Y. Water Electrolysis under a Magnetic Field. *Journal of The Electrochemical Society*. 2007;154:E112-5.
- [151] Brandt R, Fricke J. Acetic-Acid-Catalyzed and Subcritically Dried Carbon Aerogels with a Nanometer-Sized Structure and a Wide Density Range. *Journal of Non-Crystalline Solids*. 2004;350:131-5.

[152] Baumann TF, Worsley MA, Han TYJ, Satcher Jr JH. High Surface Area Carbon Aerogel Monoliths with Hierarchical Porosity. *Journal of Non-Crystalline Solids*. 2008;354:3513-5.

[153] Tuinstra F, Koenig JL. Raman Spectrum of Graphite. *The Journal of Chemical Physics*. 1970;53:1126-30.

[154] Conway BE, Pell WG. Power limitations of Supercapacitor Operation Associated with Resistance and Capacitance Distribution in Porous Electrode Devices. *Journal of Power Sources*. 2002;105:169-81.

[155] Weng TC, Teng H. Characterization of High Porosity Carbon Electrodes Derived from Mesophase Pitch for Electric Double-Layer Capacitors. *Journal of The Electrochemical Society*. 2001;148:A369-73.

[156] Rufford TE, Hulicova-Jurcakova D, Khosla K, Zhu Z, Lu GQ. Microstructure and Electrochemical Double-Layer Capacitance of Carbon Electrodes Prepared by Zinc Chloride Activation of Sugar Cane Bagasse. *Journal of Power Sources*. 2010;195:912-8.

[157] Rufford TE, Hulicova-Jurcakova D, Zhu Z, Lu GQ. Nanoporous Carbon Electrode from Waste Coffee Beans for High Performance Supercapacitors. *Electrochemistry Communications*. 2008;10:1594-7.

[158] Zhu Y, Hu H, Li W, Zhang X. Resorcinol-Formaldehyde Based Porous Carbon as an Electrode Material for Supercapacitors. *Carbon*. 2007;45:160-5.

[159] Ye JS, Liu X, Cui HF, Zhang WD, Sheu FS, Lim TM. Electrochemical Oxidation of Multi-Walled Carbon Nanotubes and its Application to Electrochemical

Double Layer Capacitors. *Electrochemistry Communications*. 2005;7:249-55.

[160] Wang J, Chen M, Wang C, Wang J, Zheng J. Preparation of Mesoporous Carbons from Amphiphilic Carbonaceous Material for High-Performance Electric Double-Layer Capacitors. *Journal of Power Sources*. 2011;196:550-8.

[161] Liu X, Juan L, Zhan L, Tang L, Wang Y, Qiao W, et al. Effect of Conductive Filler on the Impedance Behaviors of Activated Carbon Based Electric Double Layer Capacitors. *Journal of Electroanalytical Chemistry*. 2010;642:75-81.

[162] Song HK, Hwang HY, Lee KH, Dao LH. The Effect of Pore Size Distribution on the Frequency Dispersion of Porous Electrodes. *Electrochimica Acta*. 2000;45:2241-57.



Vita

| PERSONAL INFORMATION DETAILS | |
|------------------------------|--|
| Name | Jeff Chang (張雲閔) |
| Date of Birth | 11/10/1980 |
| Gender | Male |
| E-mail | unmin999@yahoo.com.tw |
| Address | 2F., No.30, Aly. 66, Ln. 180, Yongji Rd., Xinyi Dist., Taipei City 110, Taiwan |



EDUCATION

Ph.D. in Department of Material Science and Engineering, National Chiao Tung University, 2006/9~ 2012/7

Visiting Scholar in Department of Material Science and Engineering, University of California Los Angeles, 2010/10~ 2011/7

M.Sc in Department of Chemistry, Chung Yuan Christain University, 2004/9~2006/7

B.Sc. in Department of Chemistry, Chung Yuan Christain University, 2001/9~2004/7

AWARDS

1. 2011 Taipei International Invention Show& Technomart
2. National Science Council “Swift Horse Program” Overseas Traveling Grant, 2010~2011
3. China Technical Consultants incorporated Foundation “the Academic Visit for Taiwan Young Students Between Mainland China and Taiwan” Overseas Traveling Grant, 2010
4. National Chiao Tung University Overseas Traveling Grant, 2009
5. National Chiao Tung University “Aiming for the Top University and Elite Research Center Development Plan” Overseas Traveling Grant, 2008
6. National Chiao Tung University Overseas Traveling Grant, 2008
7. Outstanding Creative R&D Award 2007
8. Professor James Huang Research Paper Award 2006
9. United Microelectronics Corporation Scholarship 2006
10. National Science Council Student Overseas Traveling Grant from Taiwan, 2006
11. Materials Research Society Annual Meeting in Taiwan - Honorable Mention Award 2005

Publication List

A. Papers presented in SCI journal :

1. **YM Chang**, CY Wu, PW Wu, "Synthesis of Large Surface Area Carbon Ambient Gels for Electrochemical Double Layer Capacitors" *revised in Journal of Power Sources*.
2. YC Hsieh, LC Chang, PW Wu, **YM Chang**, Jyh-Fu Lee, "Displacement Reaction of Pt on Carbon-supported Ru Nanoparticles in Hexachloroplatinic Acids", *Applied Catalysis B: Environmental*, 2011, [103, 116–127](#).
3. **YM Chang**, YF Chang, PW Wu, CY Wu, P Lin, "Synthesis and Characterization of $\text{La}_{0.6}\text{Ca}_{0.4}\text{Co}_{0.8}\text{Ru}_{0.2}\text{O}_3$ for Oxygen Reduction Reaction in an Alkaline Electrolyte" *Journal of Electrochemical Society*, 2010, [157, B900–5](#).
4. RM Liang, **YM Chang**, PW Wu, P Lin, "Effect of Annealing on the Electrodeposited Cu_2O Films for Photoelectrochemical Hydrogen General" *Thin Solid Films*, 2010, [518, 7191–5](#).
5. JN. Tiwari, RN Tiwari, **YM Chang**, KL Lin, "A Promising Approach to the Synthesis of 3D Nanoporous Graphitic Carbon as a Unique Electrocatalyst Support for Methanol Oxidation", *ChemSusChem*, 2010, [3, 460–6](#).
6. YF Hsieh, YC Hsieh, PW Wu, CH Liao, **YM Chang** "Pulse Electrodepositions of PtRu on Large-Area Carbon Nanotubes for Enhancement of Methanol Electro-Oxidation", *Journal of Electrochemical Society*, 2010, [157, B39–44](#). [selected for *Virtual Journal of Nanoscale Science and Technology*, November 16, 2009].
7. YP Huang, **YM Chang**, TY Tsai, W Lee, "H-PDLC/Clay Nanocomposites", *Molecular Crystals and Liquid crystals*, 2009, [512, 167\[2013\]–78\[24\]](#).
8. PC Chen, **YM Chang**, PW Wu, YF Chiu "Fabrication of Ni Nanowires for Water Electrolysis in Neutral Electrolyte", *International Journal of Hydrogen energy*, 2009, [34, 6596–602](#).
9. YC Hsieh, PW Wu, YJ Lu, **YM Chang**, "Displacement Reaction in Pulse Current Deposition of PtRu for Methanol Electro-Oxidation", *Journal of Electrochemical Society*, 2009, [156, B753–42](#).
10. **YM Chang**, PW Wu, CY Wu, YC Hsieh, "Synthesis of $\text{La}_{0.6}\text{Ca}_{0.4}\text{Co}_{0.8}\text{Ir}_{0.2}\text{O}_3$ Perovskite for Bi-functional Catalysis in an Alkaline Electrolyte" *Journal of Power Sources*, 2009, [189, 1003–7](#).
11. **YM Chang**, TY Tsai, YP Huang, WS Cheng, Wei Lee, "Polymer-encapsulated Liquid Crystals Comprising Montmorillonite Clay", *Journal of Optics A: Pure and Applied Optics*, 2009, [11, 024018–24](#).
12. **YM Chang**, YC Hsieh, PW Wu, "Improved Electrochemical Performances by Carbon Nanocapsules as an Electrocatalyst Support for Direct Methanol Fuel Cells", *Diamond and Related Materials*, 2009, [18, 501–4](#).

13. **YM Chang**, YC Hsieh, PW Wu, CH. Lai, TY Chang, “Solid State Reaction Synthesis of $\text{La}_{0.6}\text{Ca}_{0.4}\text{Co}_{0.8}\text{Ir}_{0.2}\text{O}_3$ for Bifunctional Catalysis”, *Materials Letters*, 2008, [62, 4220–22](#).
14. **YM Chang**, PW Wu, CY Wu, YF. Hsieh, JY Chen, “Mechanical Alloying Preparation of $\text{La}_{0.6}\text{Ca}_{0.4}\text{CoIr}_{0.25}\text{O}_{3.5-\delta}$ as Bifunctional Electrocatalysts in Alkaline Electrolyte”, *Electrochemical and Solid-State Letters*, 2008, [11, B47–50](#). [selected for *Virtual Journal of Nanoscale Science and Technology*, *February 11, 2008*].
15. YM Lin, **YM Chang**, PW Wu, P Lin, YY Li, CY Wu, CF Tsai, KY Yeh, “Carbon Nanocapsules as an Electrocatalyst support for the Oxygen Reduction Reaction in Alkaline Electrolyte”, *Journal of Applied Electrochemistry*, 2008, [38, 507–14](#).
16. **YM Chang**, TY Tsai, YP Huang, WS Chen, W Lee, “Electrical and Electro-Optical Properties of Nematic Liquid Crystal-Montmorillonite Clay Nanocomposites”, *Japanese Journal of Applied Physics*, 2007, [46, 7368–70](#).
17. YP Huang, TY Tsai, W Lee, WK Chin, **YM Chang**, HY Chen, “The Photorefractive Effect of Nematic–Clay Nanocomposites”, *Optics Express*, 2005, [13, 2058–63](#).
18. TY Tsai, YP Huang, HY Chen, W Lee, **YM Chang**, WK Chin, “Electro-Optical Properties of a Twisted Nematic–Montmorillonite-Clay Nanocomposite”, *Nanotechnology*, 2005, [16, 1053–7](#).

B. Patents:

1. PW Wu, **YM Chang**, “Synthesis for catalysis of bifunctional perovskite compound”, United States Patent [7,955,529](#).
2. TY Tsai, YP Huang, SW Lu, **YM Chang**, “Liquid crystal composites containing photosensitive polymers and layered inorganic compounds”, Japan, JP Patent [No. 4598733](#).
3. PW Wu, **YM Chang**, “Synthesis for catalysis of bifunctional perovskite compound”, Republic of China Patent, No.097147743.
4. TY Tsai, YP Huang, SW Lu, **YM Chang**, “Liquid Crystal composite”, United States Patent [20070045588](#).
5. **YM Chang**, “Clothes Rack”, Republic of China Patent, No. 095216949.
6. TY Tsai, YP Huang, SW Lu, **YM Chang**, “Liquid Crystal composite Material”, Republic of China Patent, No.094129465.

C. Conference Talks :

1. RM Liang, **YM Chang**, PW Wu, P Lin, “Effect of Annealing on The Electrodeposited Cu_2O Films for Photoelectrochemical Hydrogen General”, TACT 2009 International Thin Films Conference, Dec. 14~16, Taipei, Taiwan
2. **YM Chang**, CY Wu, LY Wang, PW Wu, “Synthesis and Characterization of High Surface Area

- Xerogel for Supercapacitor”, 4th Asian Conference on Electrochemical Power Sources, Nov. 8~12, 2009, Taipei, Taiwan.
3. YF Chang, **YM Chang**, PW Wu, P Lin, “Synthesis Silver Nanocubes Electrocatalyst for Oxygen Reduction Reaction in an Alkaline Electrolyte”, 216th Electrochemistry Society Meeting, Oct. 4~9, 2009, Vienna, Austria.
 4. YF Chang, PW Wu, **YM Chang**, “Synthesis and Characterization of Stoichiometric $\text{La}_{0.6}\text{Ca}_{0.4}\text{Co}_x\text{Ru}_{1-x}\text{O}_3$ as Bifunctional Electrocatalysts for Oxygen Evolution and Reduction in Alkaline Electrolyte”, 214th Electrochemistry Society Meeting, Oct. 13~18, 2008, Honolulu, Hawaii, USA.
 5. **YM Chang**, PW Wu, YM Lin, P Lin, YF Chang, RM Liang, “Controlled Synthesis of Silver Particles Supported on Carbon Nanocapsules for Oxygen Reduction Reaction in Alkaline Electrolyte”, 213th Electrochemistry Society Meeting, May. 18~23, 2008, Phoenix, AZ, USA.
 6. TY Tsai, **YM Chang**, WS Chen, W Lee, “Electro–Optical Properties of the Nematic Liquid Crystal–Montmorillonite Clay Nanocomposites”, Optics and Photonics Taiwan 2005, Dec. 9~10, 2005, Tainan, Taiwan.

